Investigating the Lid Effect in the Generation of Ocean Island Basalts

Shihao Jiang[1], Rhys Hawkins[2], Mark James Hoggard[1], D. Rhodri Davies[1], and Ian H Campbell[1]

[1]Australian National University
[2]University de Lyon 1

April 15, 2024

Abstract

Ocean Island Basalts (OIBs) are generated by mantle plumes, with their geochemistry controlled by a combination of source composition, temperature, and thickness of overlying lithosphere. For example, OIBs erupting onto thicker, older oceanic lithosphere are expected to exhibit signatures indicative of higher average melting pressures. Here, we quantitatively investigate this relationship using a global dataset of Neogene and younger OIB compositions. Local lithospheric thicknesses are estimated using theoretical plate-cooling models and Bayes factors are applied to identify trends. Our findings provide compelling evidence for a correlation between OIB geochemistry and lithospheric thickness, with some variables SiO_2, Al_2O_3, FeO, Lu, Yb and λ_2) showing linear trends that can be attributed to increasing average melting pressure, whereas others (λ_0 and λ_1, CaO) require a bi-linear fit with a change in gradient at ~55 km. Observed variations in highly incompatible elements are consistent with melt fractions that decrease with increasing lithospheric thickness, as expected. Nevertheless, at thicknesses beyond ~55 km, the implied melt fraction does not decrease as rapidly as suggested by theoretical expectations. This observation is robust across different lithospheric thickness estimates, including those derived from seismic constraints. We interpret this result as weak plumes failing to effectively thin overlying lithosphere and/or producing insufficient melt to erupt at the surface, in combination with a 'memory effect' of incomplete homogenisation of melts during their ascent. This view is supported by independent estimates of plume buoyancy flux, indicating that OIB magmatism on older lithosphere may be biased towards hotter plumes.

Investigating the Lid Effect in the Generation of Ocean Island Basalts

Shihao Jiang[1], Rhys Hawkins[1], Mark J. Hoggard[1], D. Rhodri Davies[1]& Ian H. Campbell[1]

[1]Research School of Earth Sciences, Australian National University, Canberra, ACT 2601, Australia

Key Points:

- We quantify the relationship between lithospheric thickness and OIB geochemistry: the so-called *lid effect*.
- Observed trends are controlled by pressure-related variations in melt fraction, mineral assemblage, and spinel-garnet phase transition.
- Magmatism beneath older lithosphere may be biased towards hotter plumes that more effectively thin and penetrate overlying lithosphere.

Corresponding author: Shihao Jiang, shihao.jiang1@anu.edu.au

Abstract

Ocean Island Basalts (OIBs) are generated by mantle plumes, with their geochemistry controlled by a combination of source composition, temperature, and thickness of overlying lithosphere. For example, OIBs erupting onto thicker, older oceanic lithosphere are expected to exhibit signatures indicative of higher average melting pressures. Here, we quantitatively investigate this relationship using a global dataset of Neogene and younger OIB compositions. Local lithospheric thicknesses are estimated using theoretical plate-cooling models and Bayes factors are applied to identify trends. Our findings provide compelling evidence for a correlation between OIB geochemistry and lithospheric thickness, with some variables (SiO_2, Al_2O_3, FeO, Lu, Yb and λ_2) showing linear trends that can be attributed to increasing average melting pressure, whereas others (λ_0 and λ_1, CaO) require a bi-linear fit with a change in gradient at ~ 55 km. Observed variations in highly incompatible elements are consistent with melt fractions that decrease with increasing lithospheric thickness, as expected. Nevertheless, at thicknesses beyond ~ 55 km, the implied melt fraction does not decrease as rapidly as suggested by theoretical expectations. This observation is robust across different lithospheric thickness estimates, including those derived from seismic constraints. We interpret this result as weak plumes failing to effectively thin overlying lithosphere and/or producing insufficient melt to erupt at the surface, in combination with a 'memory effect' of incomplete homogenisation of melts during their ascent. This view is supported by independent estimates of plume buoyancy flux, indicating that OIB magmatism on older lithosphere may be biased towards hotter plumes.

Plain Language Summary

Most of Earth's volcanoes occur at tectonic plate boundaries, but some emerge within plate interiors in so-called intra-plate settings. These volcanoes are believed to mark the surface expression of mantle plumes: hot, buoyant columns that rise from the core-mantle-boundary towards the surface. As they rise, lower pressures near the surface facilitate melting. However, the lithosphere – Earth's rigid outermost shell – limits plume ascent, and therefore controls the final (lowest) melting pressure of mantle plumes (the 'lid effect'). Here, we collate and analyse a global geochemical dataset of oceanic island basalts – the products of plume melting – to test this hypothesis. Using a range of diagnostics and a novel probabilistic analytical approach, we find that some geochemical parameters either linearly increase or decrease with lithospheric thickness, whereas other trends exhibit abrupt changes. We propose potential explanations for these patterns, focusing on factors such as the melt fraction (which is sensitive to temperature and pressure) and variations in mantle mineralogy at different depths. Notably, we suggest that there is a higher chance of observing volcanism above hotter plumes in regions of thicker lithosphere and identify a 'memory effect', whereby their geochemistry to some extent preserves information from the initial melting process.

1 Introduction

While the majority of Earth's volcanism is concentrated at tectonic plate boundaries, there are many volcanic activities that occur within plate interiors and/or extend across plate boundaries. Although some of this volcanism has been attributed to edge-driven convection, shear-driven upwelling and bursts in slab flux (e.g., King & Anderson, 1998; Conrad et al., 2011; D. R. Davies & Rawlinson, 2014; Rawlinson et al., 2017; Mather et al., 2020; Duvernay et al., 2021), the majority displays characteristics that imply an association with mantle plumes – hot, buoyant columns that rise from the core-mantle boundary towards the surface (e.g., Morgan, 1971; Griffiths & Campbell, 1990, 1991; Duncan & Richards, 1991; Campbell, 2007; D. R. Davies & Davies, 2009, Figure 1). As they rise into the shallow mantle, plumes undergo partial melting, with voluminous plume heads giving rise to Large Igneous Provinces and their tails producing lower fraction melts, termed *Ocean Island Basalts* (OIBs) in oceanic settings (e.g, White & McKenzie, 1989). The geological, geophysical and geochemical characteristics of OIBs have been widely studied (e.g., White & McKenzie, 1989; Weaver, 1991; Courtillot et al., 1999; Li et al., 2014; D. R. Davies, Goes, & Sambridge, 2015; Jones et al., 2016; Iaffaldano et al., 2018; P. W. Ball et al., 2019; Nebel et al., 2019; Jones et al., 2019; Bao et al., 2022). Nevertheless, despite mantle-plume theory being well established, our understanding remains incomplete concerning the interaction between plumes and overlying lithosphere – Earth's rigid outermost shell – and its reflection in the geochemistry of OIBs.

The lithospheric mantle is cool and refractory. Accordingly, it is unlikely to melt and generate magmas (e.g., Katz et al., 2003). In addition, the lithosphere is highly viscous and is therefore difficult to mechanically deform (e.g., Burov et al., 2007; Campbell, 2007; Burov & Gerya, 2014; Jones et al., 2017; Duvernay et al., 2021, 2022). As a consequence, it is expected to act as a lid that limits plume ascent and thereby dictate the lowest melting pressure for plume-derived melts (Figure 1). This behaviour is the so-called *'lid effect'*, first proposed by Watson and McKenzie (1991) and subsequently examined in several studies at both global (e.g. Ellam, 1992; Humphreys & Niu, 2009; Dasgupta et al., 2010; Niu et al., 2011; Niu, 2021) and regional scales (e.g. Gibson & Geist, 2010; D. R. Davies, Rawlinson, et al., 2015; Hole & Millett, 2016; Liu et al., 2016; Klöcking et al., 2018). Despite this extensive body of work, a complete and statistically rigorous assessment of the relationship between lithospheric thickness and the geochemistry of plume-derived magmas has not yet been established: previous studies have either described this relationship qualitatively or only made use of simple linear statistics (e.g. Ellam, 1992; Humphreys & Niu, 2009; Niu et al., 2011; D. R. Davies, Rawlinson, et al., 2015; Niu, 2021). Several important questions remain, including:

1. Do available geochemical data statistically support existence of a lid effect?
2. Are observed trends consistent with theoretical expectations for partial melting at different pressures?
3. What other processes might be affecting observed trends?

The last few years have seen progress in several areas that are pertinent to answering these questions. There has been a steady increase in the quantity and accessibility of high-quality data available on melt geochemistry, improvements in the accuracy and resolution of lithospheric thickness datasets, and the advent of comprehensive statistical techniques to examine any potential relationship between the two. There is, therefore, an opportunity to undertake a critical revaluation of evidence for the lid effect.

Our study exploits an extensive and carefully curated dataset of geochemical analyses for OIBs, extracted from the ever-growing open-source GeoRoc database (https://georoc.eu). The dataset is filtered to eliminate those samples whose geochemistry has been strongly altered after initial magma generation. Alongside the geochemical parameters examined by previous studies, we analyse geochemical diagnostics on Rare Earth Elements (REEs) that have been recently proposed by O'Neill (2016) and are expected to show a clear pressure signal owing to their sensitivity to melt fraction and the spinel-garnet phase transition. The latter, a pressure-sensitive aluminium-rich phase change, induces a substantial change to the peridotite mineral assemblage, with different REEs exhibiting varying compatibility between the two phases (e.g., Sun & Liang, 2013; Wood et al., 2013). Furthermore, we exploit new estimates of lithospheric thickness, based upon both theoretical models of oceanic spreading and observational constraints from seismic data (Richards, Hoggard, Crosby, et al., 2020; Hoggard, Czarnota, et al., 2020). Using a probabilistic Bayesian approach that is capable of detecting sharp changes in geochemical trends, we investigate the role of lithospheric thickness in controlling OIB geochemistry and explore the mechanisms that underpin the trends that we observe.

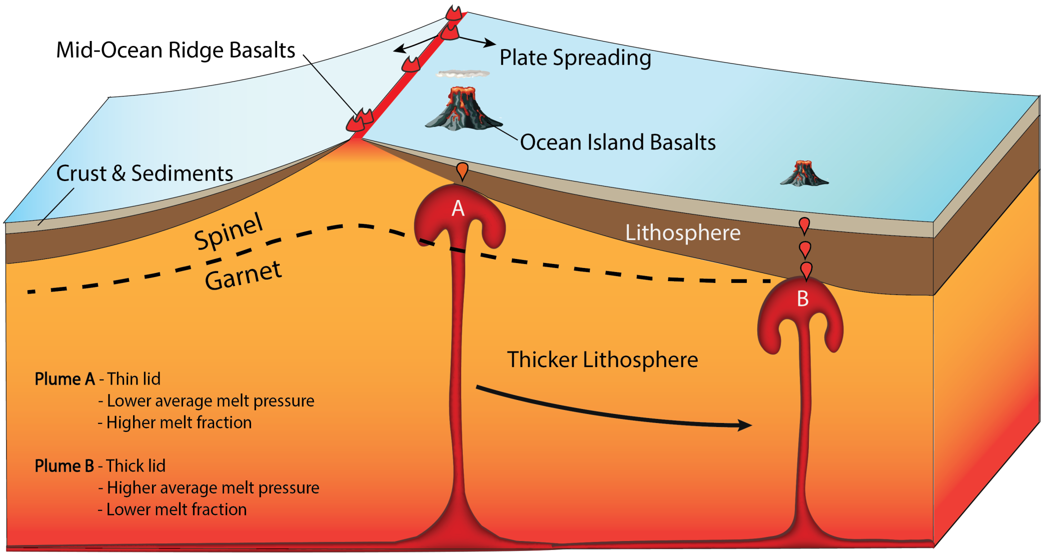

Figure 1. Schematic cartoon illustrating how oceanic lithosphere acts as a lid, hindering the ascent of mantle plumes. The dashed line represents the spinel-garnet transition. When a plume rises beneath thin lithosphere, large melt volumes will be produced with more melts generated within the spinel stability field, thus exhibiting a low-pressure signature. Conversely, when a plume rises beneath thick lithosphere, melt volumes are smaller and melting will principally occur within the garnet stability field, displaying a high-pressure signature.

The remainder of our paper is structured as follows. In Section 2.1, we introduce our OIB database, our approach to filtering this data, and the geochemical diagnostics examined. In Section 2.2, we describe the lithospheric thickness estimates at each individual island, derived using both plate-cooling models and local constraints from surface-wave tomography models. In Section 2.3 we present a probabilistic Bayesian approach developed and utilised to analyse relationships between geochemistry and lithospheric thickness. Our results are presented in Section 3, with their sensitivities, implications for our understanding of the lid-effect, the role of the lithosphere in modulating plume melting, and other processes affecting OIB chemistry, discussed in Section 4.

2 Methods

2.1 Geochemical Dataset

In compiling our geochemical database of the products of plume melting in oceanic settings, we have chosen to focus solely on OIB data and neglect data associated with Large Igneous Provinces (LIPs). This omission is because LIPs are the melt-products of plume heads and are also often associated with continental break-up. They regularly occur in the vicinity of the continent-ocean boundary and consequently often display a strong crustal signature (e.g., Chung & Jahn, 1995; Owen-Smith et al., 2017; J. H. F. L. Davies et al., 2021). It is also therefore difficult to estimate lithospheric thickness at the time of eruption (e.g., Hill, 1991; Courtillot et al., 1999).

2.1.1 Source of Analyses

Geochemical data for major and trace element concentrations are compiled from OIB data in the GeoRoc database. As the number of high-quality glass samples is limited, the data are derived principally from analyses of bulk rocks (with some additional glass analyses where available). The GeoRoc database contains geochemical information from over 20,000 OIB samples from the Atlantic, Indian and Pacific Oceans, with their locations mapped in Figure 2 and listed in Tables S1 and S2. Our database incorporates concentrations of major (SiO_2, Al_2O_3, MgO, FeO, TiO_2, Na_2O, K_2O, CaO, P_2O_5) and trace elements (REEs, U, Nb, Ba, Th), as well as derivative parameters describing REE patterns (λ_0, λ_1 and λ_2, from O'Neill, 2016). Major elements with high concentrations are likely influenced by the stabilities of minerals under varying pressure and their compatibilities in mantle peridotite. We expect that major elements with lower concentrations (usually < 5 wt. %) and trace elements are sensitive to phase changes and the melt fraction, which, in turn, are sensitive to pressure. The combined use of both major and trace element parameters can therefore offer a more complete picture of the impact of the lithospheric lid on mantle melting processes.

2.1.2 Database Filtering

Melts generated from peridotite melting are subject to various physiochemical processes during their ascent and whilst residing in magma chambers, such as fractional crystallisation and crustal assimilation (e.g., Sisson & Grove, 1993; Class & Goldstein, 1997; Straub et al., 2013; Ubide et al., 2022). Additionally, post-eruptive hydrothermal alteration can substantially alter the original chemical signature of basalts (e.g., Saito et al., 2015; Khogenkumar et al., 2016). Some previous studies of the lid effect have chosen to use all available OIB geochemical data without attempting to screen samples that are heavily impacted by these additional processes (e.g., Humphreys & Niu, 2009). In our analyses, however, we have filtered OIB samples to isolate those that exhibit a composition most similar to that of the primitive magma. We therefore restrict our dataset to samples that have not undergone excessive alteration or fractional crystallization after initial generation. We do so by applying the following filters to the data:

1. Only those samples with SiO_2 43–54 wt.% are accepted in order to exclude melts that fall outside of the basalt field (Figure 3a);
2. Only samples with MgO 7–16 wt.% are accepted. Values with MgO < 7 wt.% are likely to have been subjected to extensive fractional crystallisation (e.g., Sisson & Grove, 1993) and may contain clinopyroxene and/or plagioclase phenocrysts or have experienced clinopyroxene and plagioclase crystallisation, complicating interpretation of major element trends. Samples with MgO > 16 wt.% are rejected because they are likely to contain olivine phenocrysts (Figures 3a and 3b, e.g., Albarède et al., 1997);
3. Samples with a loss on ignition (LOI) > 3 wt.% are rejected to eliminate basalts subjected to excessive levels of post-eruptive hydrothermal alteration (e.g., Greenberger et al., 2012);
4. Samples with Nb/U < 30, La/Nb > 1.2, or La/Ba and Nb/U values outside of the ellipse of Fitton et al. (1991) are rejected because they are likely to have been contaminated by continental crust (e.g., Rudnick, 1995; Condie, 1999; Hofmann, 2003, Figures 3c and 3d).

Applying these filters to the global OIB dataset results in a subset of 1,737 samples, each consisting of concentrations of major elements, trace elements and REEs.

2.1.3 Correction for Fractional Crystallisation

When magma travels through the lithosphere or remains in a magma chamber, any fractional crystallisation that occurs alters the concentration of major and trace elements in the remaining melt (e.g., Jackson et al., 2012; Ubide et al., 2022). Provided that the mineral phases that have crystallised are not complex, we can 'revert' this process to es-

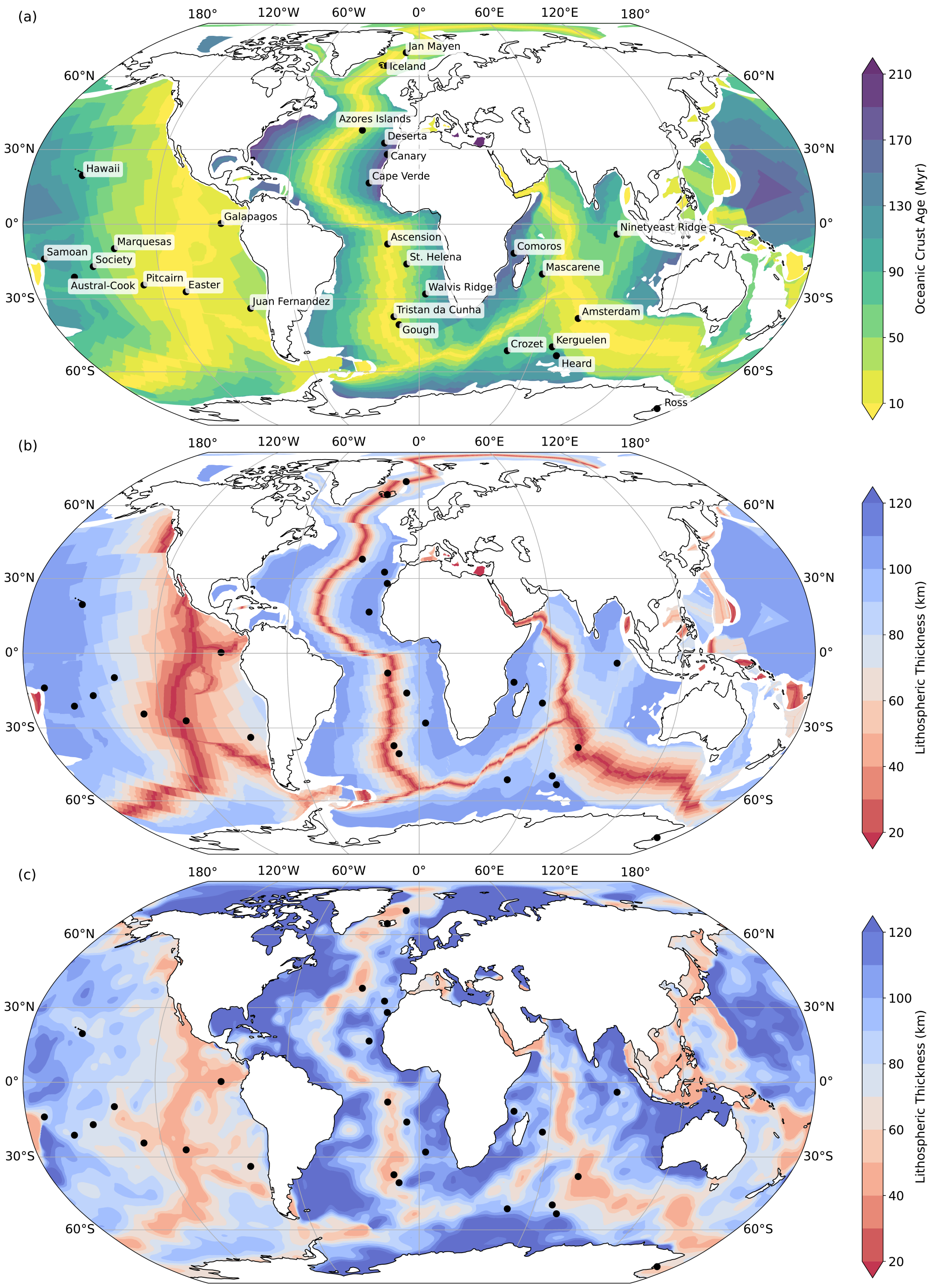

Figure 2. (a) Present-day oceanic lithospheric age from Seton et al. (2020) with locations of selected OIB samples (black dots). Only the name of the archipelago for each island group is displayed, but each individual island's lithospheric age and thickness are considered separately during the analysis. (b) Present-day oceanic lithospheric thickness based on a global plate-cooling model (Richards, Hoggard, Crosby, et al., 2020). (c) Present-day oceanic lithospheric thickness constrained by surface-wave tomography (Hoggard, Czarnota, et al., 2020).

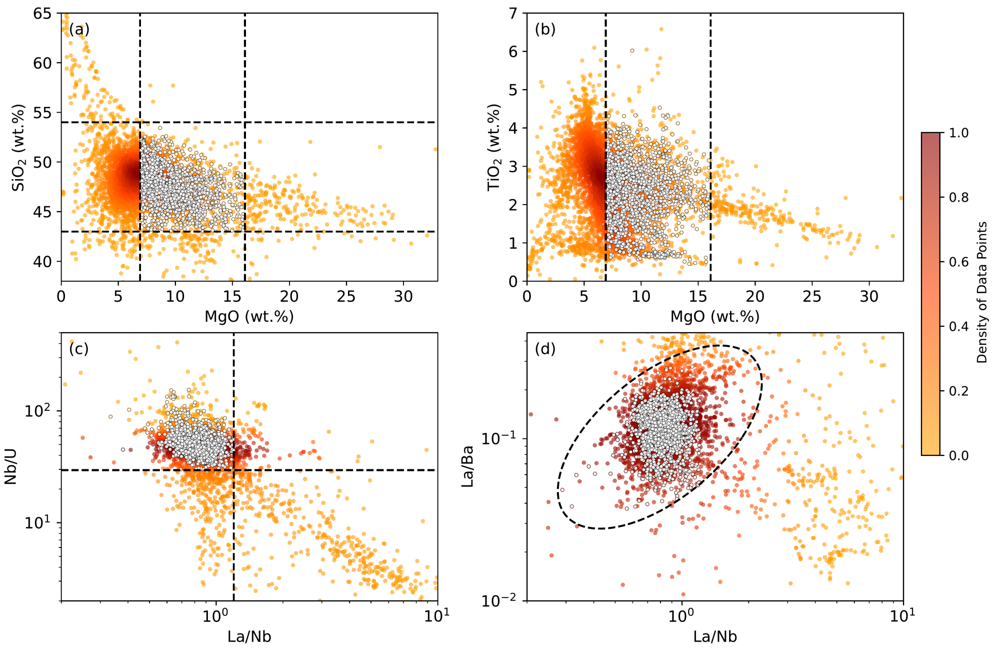

Figure 3. OIB database and sample filtering criteria. (a) SiO_2 versus MgO; coloured dots = original samples coloured by Gaussian kernel density estimation, normalised from 0 to 1; dashed lines = filtering criteria corresponding to SiO_2 43–54 wt.% and MgO 7–16 wt.%; white circles = subset of data that pass all filtering criteria. (b) Same for TiO_2 versus MgO. (c) Same for Nb/U versus La/Nb, where criteria of > 30 and < 1.2, respectively, are applied. (d) Same for La/Ba versus La/Nb, where only samples inside the ellipse of Fitton et al. (1991) are accepted.

timate concentrations of both major and trace elements in the primary magma. To do so, we use the Petrolog3 software (Danyushevsky & Plechov, 2011) to reintroduce olivine into evolved OIBs until MgO concentrations reach 16 wt.%, which is the assumed MgO content of magma that is in equilibrium with the mantle (e.g., Norman & Garcia, 1999). Despite some studies showing that minerals fractionate throughout magma ascent (e.g., Lundstrom et al., 2003; Liu et al., 2016), we make the simplifying assumption that this olivine did not crystallise until melts reached a magma chamber at ~ 0.3 GPa ($\sim$9 km depth). This choice of depth roughly coincides with the Moho, where the drop in density from mantle to crustal rocks results in melts becoming neutrally buoyant, allowing magma to remain in the chamber for a more extended period of time (Ryan, 1988, 1994). In the continuous, pure fractional crystallisation process, we assume that partition coefficients for trace elements in olivine remain constant. For each individual OIB sample, we use the major element calculations of Petrolog3 to determine how much olivine to 'add back in' to obtain the composition of the primitive magma. Accordingly, the concentration of each trace element in the primitive magma (c_p) is calculated via

$$c_\mathrm{p} = \frac{c_\mathrm{l}}{(1 - X)^{D-1}}, \quad (1)$$

where c_l is the measured concentration of each element in the sample, X is the fraction of olivine crystallised, and D is the associated partition coefficient (Shaw, 1970).

2.1.4 Shape of REE patterns

Due to their high charge and large ionic radii, REEs behave as incompatible elements in most mantle minerals. Moreover, the consistency of REE chemical valence makes their ionic radius systematically decrease with increasing atomic number (so-called lanthanide contraction; Ahrens, 1952). Since REEs occupy identical crystal lattice positions, their partition coefficients therefore exhibit a systematic dependence on atomic number, with lower atomic number REEs (Light Rare Earth Elements; LREEs) possessing larger radii and being more incompatible. Accordingly, during partial melting, REEs with a smaller atomic number more preferentially enter the melt than their heavier counterparts, an imbalance that is particularly pronounced at low degrees of melting. A caveat to this basic behaviour is that heavy rare earth elements (HREEs) readily substitute for Al^{3+} in garnet and, hence, can be compatible in garnet. As such, low-fraction melts generated within the garnet stability field will have lower HREE concentrations than equivalent melts generated in the spinel stability field. Many laboratory experiments have been conducted to constrain the partition coefficients of REEs, with results consistent with these aforementioned theoretical predictions (e.g., Fujimaki et al., 1984; McKenzie & O'Nions, 1991; Johnson, 1994, 1998). It is also worth noting that, due to the general incompatibility of REEs in all low-pressure mineral phases, their relative proportions are generally unaffected by fractional crystallisation at low pressure.

The systematic variation in REE behavior is best illustrated by plotting the log of their relative abundances as a function of atomic size: as demonstrated by O'Neill (2016), such patterns can be fit by polynomials with different shape coefficients. Given current analytical precision, third-order polynomials are usually sufficient to fit measured REE patterns. Their coefficients are denoted as λ_i (where $i = 0, 1, 2$) and can vary independently of one another. λ_i values also have a physical significance: (i) λ_0 measures the average log concentration of REEs (excluding Eu) normalized to their chondritic concentrations, with higher λ_0 indicating higher average REE concentrations; (ii) λ_1 measures the linear slope of the pattern (with increasing values for larger slopes), where positive λ_1 values indicate LREE enrichment relative to HREE and negative λ_1 values indicate HREE enrichment relative to LREE; (iii) λ_2 describes the quadratic curvature of the pattern (with increasing absolute values for larger curvatures), where positive and negative λ_2 indicate concave or convex REE patterns, respectively. In contrast to the simple ratios between two REEs, such as Ce/Y and La/Sm, that have been extensively used in previous studies (e.g., Ellam, 1992; Humphreys & Niu, 2009; Niu, 2021), λ_i considers all REEs except Eu and is more robust to the idiosyncrasies of individual element behavior.

2.2 Lithospheric Thickness and Eruptive Age

The thickness of oceanic lithosphere as a function of ocean floor age is commonly approximated through one of two theoretical cooling models: (i) the half-space model, in which lithospheric thickness is proportional to the square root of lithospheric age (Turcotte & Oxburgh, 1967); and (ii) the plate model, where lithospheric thickness increases with plate age, but asymptotes towards a constant value beyond a certain age due to heat resupply from below (McKenzie, 1967). Plate-model predictions have been shown to provide an improved match to heat flow and bathymetry observations in older ocean floor and also inferences of lithosphere-asthenosphere boundary (LAB) depth obtained from seismology (McKenzie, 1967; Parsons & Sclater, 1977; Richards et al., 2018; Richards, Hoggard, Crosby, et al., 2020). Accordingly, the plate model is our preferred reference and we test two different versions of it: one derived from globally averaged subsidence and heatflow data and the second providing optimal fits to subsets of these data from each individual oceanic basin (Atlantic, Indian and Pacific Oceans; Richards, Hoggard, Crosby, et al., 2020). We present results for the latter in the main text and also conduct assessments of the sensitivity of our results to this choice, with a summary presented in the Supplementary Information. In all cases, the potential temperature in the model is fixed to 1333°C and the base of the lithosphere is assumed to follow the 1175 ± 50°C isotherm (Richards, Hoggard, Crosby, et al., 2020).

A limitation of theoretical cooling models is that they assume oceanic lithospheric thickness varies solely as a function of ocean-floor age and, hence, cannot capture local deviations away from this average behaviour. Seismological observations, particularly from surface-wave tomography, provide a way of mapping these local variations in lithospheric thickness, including those potentially induced by the impingement of mantle plumes (Ballmer et al., 2011; Schaeffer & Lebedev, 2013; Richards, Hoggard, White, & Ghelichkhan, 2020; Duvernay et al., 2022). Accordingly, to complement our plate-model derived estimates of lithospheric thickness and explore the sensitivity of our results to regional lithospheric thickness variations, we also make use of a seismologically derived model of lithospheric thickness from Hoggard, Czarnota, et al. (2020).

We separate ocean islands into two categories: products from off-axis and on-axis plumes. For off-axis islands, we estimate lithospheric thickness using the aforementioned plate-cooling and seismologically derived models. Unfortunately, neither theoretical cooling models nor global-scale seismic estimates are good at constraining lithospheric thickness above on-axis plumes. The former do not capture the consequences of increased melt generation and hence thicker crust above plumes, while the latter suffer from the limited resolution of surface waves at depths shallower than ∼ 75 km (White & McKenzie, 1989; Priestley & McKenzie, 2006). For on-axis islands, we therefore obtain lithospheric thickness from local estimates of crustal thickness, assuming that melting extended to the top of the underlying mantle as is observed in ophiolites (e.g., Pallister & Hopson, 1981). Seismic estimates for Moho depths are as follows: Iceland ∼ 20–30 km (White et al., 1996); Ninetyeast Ridge, ∼ 15–25 km (Grevemeyer et al., 2001); Walvis Ridge ∼ 10–25 km (for lithosphere that is now aged between 60 Ma and 100 Ma; Goslin & Sibuet, 1975; Graça et al., 2019). At each of these sites, we calculate average lithospheric thickness according to $\frac{1}{2}(h_{\max}+h_{\min})$, where $h_{\max}$ and $h_{\min}$ are the maximum and minimum estimates of Moho depth, respectively.

Estimating lithospheric thickness at the time of eruption requires knowledge of lithospheric age at that time, which can be obtained by subtracting the OIB age from the present-day lithospheric age (Figure 2a). Present-day lithospheric age for each island is obtained from the global grid of Seton et al. (2020), with the age range of OIBs on each island constrained, where possible, by the onset and termination of the shield stage of volcanism or, in cases where geological constraints on the shield period are unavailable or unclear, the maximum and minimum age of OIB samples (Tables S1 and S2).

To estimate lithospheric thickness at the time of eruption for off-axis plumes, we assume that both the present-day lithospheric age (t_{crust}) and the OIB age (t_{OIB}) on each island follow a Gaussian distribution as

$$t_{\text{crust}} \sim \mathcal{N}(\mu_1,\, \sigma_1^2), \tag{2}$$

$$t_{\text{OIB}} \sim \mathcal{N}(\mu_2,\, \sigma_2^2), \tag{3}$$

where μ_1 is the oceanic crustal age, σ_1 is half of the age misfit, μ_2 is the mean of maximum and minimum OIB eruption ages, and σ_2 is a quarter of the length of the OIB major eruption period. t_{crust} and t_{OIB} can be considered as independent random variables, thus the age of oceanic lithosphere at the time of OIB volcanism (t_{erupt}) should also follow a Gaussian distribution given by

$$t_{\text{erupt}} \sim \mathcal{N}(\mu_1 - \mu_2,\, \sigma_1^2 + \sigma_2^2). \tag{4}$$

Lithospheric thickness is estimated from the theoretical cooling models by assuming that it lies between the 1125 °C and 1225 °C isotherms. We assume that lithospheric thickness (z) at a given time follows a Gaussian distribution according to

$$z \sim \mathcal{N}(\mu_3, \sigma_3^2), \tag{5}$$

in which μ_3 is the mean of the lithospheric thickness obtained from the 1125°C and 1225°C isotherms and σ_3 is a quarter of the difference in depth between them. For each island, we randomly choose a t_{erupt} based on Equation (4) and calculate the corresponding lithospheric thickness using Equation (5). Iteratively repeating this process until reaching a stable distribution of thickness estimates yields the plate-model-derived mean value of lithospheric thickness beneath each ocean island.

For the seismically constrained estimates of lithospheric thickness, we test two end-member scenarios: (i) lithospheric thickness at the time of eruption is equivalent to that of the present day; and (ii) following eruption and movement away from the location of the plume tail, the lithosphere has re-thickened to its present-day value by conductive cooling following a half-space model. The true scenario likely falls between these two assumptions. Both assumptions yield similar results, likely because the majority of OIBs in our dataset are young (< 10 Ma) and the lithosphere cannot substantially rethicken over such a short time frame. Correcting for this process makes no appreciable difference to our results (< 5 km thickness change; see Supplementary Tables S4 and S5) and the size of this correction is generally smaller than the depth range covered by the 1175± 50°C isotherms. When using seismically derived estimates of lithospheric thickness, we therefore adopt the first option above.

Estimated lithospheric thickness at the time of eruption, based on either the basin-specific plate models (Richards, Hoggard, Crosby, et al., 2020) or seismological constraints (Hoggard, Czarnota, et al., 2020), are tabulated in Supplementary Tables S4 and S5. Plate model thicknesses for the Atlantic basin are slightly greater than those derived from the global-average model, whereas in the Indian and Pacific basins, lithospheric thickness estimates from basin-based models are similar to, or thinner than, those of the global model (Supplementary Figure S1).

2.3 Bayesian Model Selection

To investigate the variation of each geochemical parameter with lithospheric thickness, we have plotted and parameterised OIB geochemical data against lithospheric thickness at the time of eruption. To understand whether a particular dataset suggests a trend, or a change in gradient, we make use of Bayes factors: the ratio of the evidence or marginal likelihood between two competing statistical models (Jeffreys, 1935; Kass & Raftery, 1995). The evidence represents the integral of the likelihood over the prior for a given model choice. In our case, it quantitatively evaluates how likely it is to generate the observed geochemical dataset, based on a specified model (i.e., a function that describes the trend of the geochemical parameters against lithospheric thickness). Therefore, given two or more competing models, the model with the larger evidence is preferred. Computing the evidence is difficult, particularly for large dimension models, but for this problem we use Dynamic Nested Sampling (Skilling, 2006; Speagle, 2020), which gives both posterior and evidence estimates in a single analysis.

The geochemical data include the raw and fractional crystallisation-corrected concentrations of major elements, trace elements and λ values calculated from REE concentrations. To determine whether a given geochemical parameter is sensitive to lithospheric thickness or influenced by any potential sudden changes in mantle composition, such as the phase change from spinel to garnet peridotite, three models were compared: (i) a constant value model (which would imply no sensitivity to lithospheric thickness); (ii) a linear model (which suggests a lid effect); and (iii) a bi-linear model that permits a change in gradient at some depth determined by the data (Figure 4). We choose not to examine exponential models since they are monotonous, so incapable of describing a

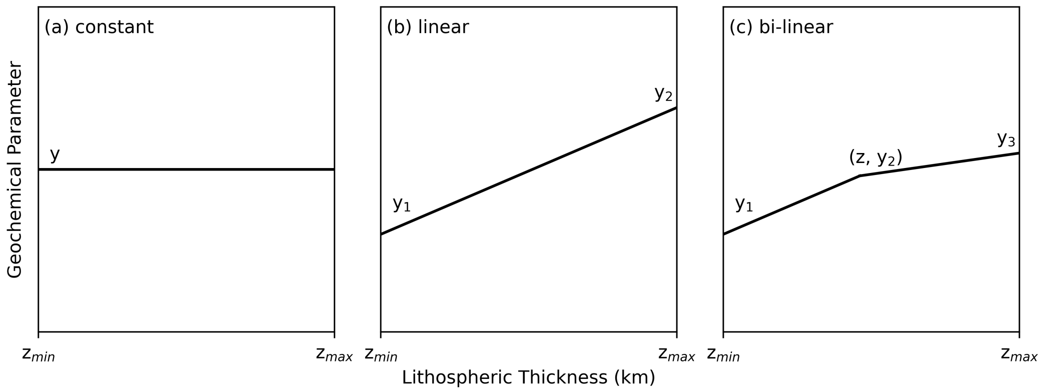

Figure 4. Schematic cartoon showing (a) a constant model with one unknown parameter; (b) a linear model with two unknown parameters; and (c) a bi-linear model with four unknown parameters. Associated model variables are labelled.

reverse in a trend or detecting the depth of a potential trend change. To estimate posterior probability densities of the model parameters for each candidate model, we choose an independent Gaussian likelihood which is written as

$$L(\boldsymbol{p}|\boldsymbol{d}) \propto \exp\left[-\frac{1}{2}\sum_{i=1}^{M}\sum_{j=1}^{N_i}\frac{(p_i - d_j)^2}{\sigma^2}\right], \tag{6}$$

where M is the number of islands, N_i the number of samples for each island i, p_i is the model prediction of the geochemical concentration for island i, d_j is the observed data value for each sample from that island, and σ is the overall standard error. This formulation assumes that the data follows the standard normal distribution at each lithospheric thickness.

We fix values for the minimum and maximum lithospheric thicknesses (z_{min} and z_{max} in Figure 4), resulting in one, two and four unknown parameters for the constant, linear and bi-linear models, respectively. The use of Bayes factors to test the relative support of competing models is subtly affected by the choice of priors. Regarding priors for the y values (i.e., the geochemical data), we adopt an empirical Bayes approach and set the prior to be Gaussian with mean and standard deviation equal to that of the overall data. The mean and standard deviation of z (i.e., the lithospheric thickness of a putative transition in the trend for the bi-linear model) are assumed to be 60 km and 5 km respectively, close to the average of all thickness data. To test the sensitivity of evidence calculations, we ran repeated tests that changed the standard deviation of the prior by $\pm 10\%$, which resulted in an average change of $\log_{10}$ evidence values of ± 0.14. Similarly, changing the standard deviation by $\pm 50\%$ (a comparatively large change in the prior) resulted in an average change in the $\log_{10}$ evidence of ± 0.18. We are therefore confident that the choice of priors for our Bayesian evidence calculations are reasonable and that sensitivity to the choice of priors is minor. Nonetheless, in the Bayesian evidence results herein, a reasonable error bound on the numerical $\log_{10}$ evidence values would be ± 0.2.

The evidences for constant, linear and bi-linear models are denoted as E_0, E_1, and E_2, respectively. Since evidence values are typically vanishingly small numbers, they are usually represented by their logarithms. A candidate model with a larger evidence value is to be preferred, for example, model "A" with a $\log_{10}$ evidence of -1000 is a hundred times more likely than a competing model "B" with a $\log_{10}$ evidence of -1002. Generally, a difference in the $\log_{10}$ evidence greater than 2 is taken to be statistically significant (Jeffreys, 1935; Kass & Raftery, 1995). We note that model evidence values can only be compared for the same geochemical parameter, as they are influenced by the range of values in the data and sample sizes. As a reminder, the constant model implies that a geochemical parameter is insensitive to changes in lithospheric thickness. The linear model can detect an overall trend but is incapable of describing a change or reversal in trend. The bi-linear model can be useful for identifying a change point in a trend and even detecting a reversal of the trend, but is more sensitive to outliers. For a given geochemical parameter, if $\log_{10}E_1 - \log_{10}E_0 > 2$, we are confident in saying that it varies with lithospheric thickness. Furthermore, if $\log_{10}E_2 - \log_{10}E_1 > 2$, we can say that a change point or kink can be found in the data trend. In these cases, we provide histograms of the depth of the likely kink in the model and calculate its mean and standard deviation.

2.4 Sensitivity to Sites with Large Numbers of Samples

Due to the form of our likelihood function in Equation (6), clusters of large numbers of measurements from a single site could potentially bias the results. Two notable examples of this are the large OIB sample sizes of Iceland and Hawaii. To test the robustness of our results to potential biasing from these two localities, we repeat the calculation of posterior probability densities and evidence values for each geochemical parameter using: (i) all data (i.e. our reference case); and (ii) the dataset with samples from both Iceland and Hawaii excluded. Removal of Hawaiian samples is of particular relevance because they represent the only OIBs located on thick lithosphere that are dominated by tholeiites (e.g., MacDonald & Katsura, 1964). All other OIBs at and beyond these lithospheric thicknesses consist predominantly or exclusively of alkali basalts (e.g., Schmincke, 1982; Fisk et al., 1988; Gautier et al., 1990).

3 Results

To provide a relatively simple overview that gets at the essence of our results, we have chosen to focus in the main text on a preferred reference case. This case includes the initial correction of geochemical concentrations for the effects of fractional crystallisation, uses data from all OIB localities within our database, and adopts lithospheric thicknesses from basin-specific plate-cooling models. While we discuss any important differences that arise from changes to this reference setup in the main text, the full suite of associated figures and results are presented in the Supplementary Information.

3.1 Geochemical Histograms

Raw histograms of major element concentrations for all OIB data, before application of sample filters, display slightly skewed Gaussian-like distributions with peaks at approximately 7 wt.% for MgO, 48 wt.% for SiO_2, 3 wt.% for TiO_2, and 14 wt.% for Al_2O_3 (blue bars in Figure 5a–d).The MgO peak at 7 wt.% broadly coincides with the minimum in magma density at 7–8 wt.% MgO calculated using Petrolog3 at 0.1 GPa, which is consistent with expectations that the lightest magmas are the most likely to erupt at the surface (see Supplementary Figure S2; Danyushevsky & Plechov, 2011). The continuous distribution of major element concentrations is consistent with expectations for mixing of distinct, end-member reservoirs to varying extents, which is also supported by isotopic evidence (e.g., Hart et al., 1992). Filtering the raw data according to the criteria outlined in Section 2.1.2 has limited impact on distributions for SiO_2, Al_2O_3 and TiO_2, but the filtered MgO histogram retains only the right-hand side of the distribution due to the sharp cut-off of samples with MgO < 7 wt.% (green bars in Figure 5a–d). Histograms of the REE shape parameters for filtered OIB samples exhibit more scatter and less clean unimodal behaviour (Figure 5e–g). Nevertheless, λ_0 has a clear peak at ~ 3.3. λ_1 is left skewed, with a peak around 10 and more than 80% of samples have

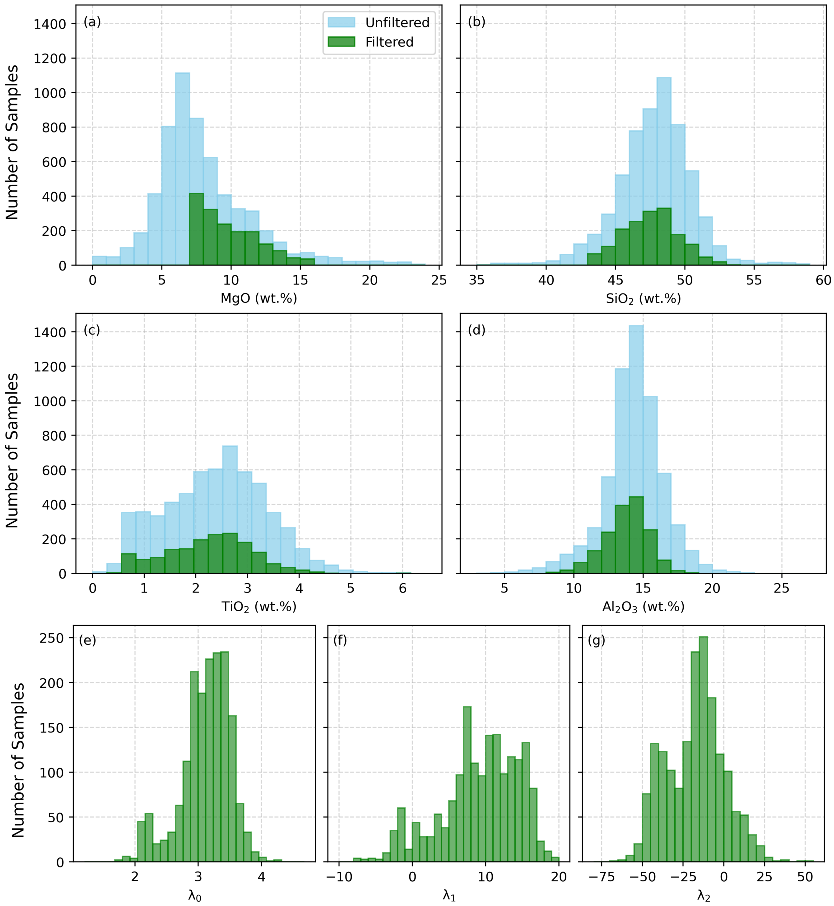

Figure 5. Concentration histograms of (a) MgO; (b) SiO_2; (c) TiO_2; and (d) Al_2O_3 in our OIB dataset. Original, unfiltered data are colored blue, while data in green represent the subset of data remaining following application of screening filters outlined in Section 2.1.2. For simplicity, histograms of (e) λ_0, (f) λ_1, and (g) λ_2 values are shown only for filtered OIB samples.

$\lambda_1 > 5$. λ_2 is somewhat bimodal, with a central peak at approximately -15 and a subsidiary peak at -40.

3.2 Evidence Results

3.2.1 Example of Statistical Results

To illustrate our procedure for quantifying the relationship between lithospheric thickness and various geochemical parameters, we present two examples for Al_2O_3 and λ_1 in Figure 6. Both use our reference setup, in which the global OIB dataset is filtered and corrected for fractional crystallisation, with lithospheric thickness evaluated via the basin-specific plate model. Black crosses represent individual OIB samples and $\log_{10}$ of the evidence is provided for each of the three types of model.

For both Al_2O_3 and λ_1, we find that the evidence increases by ~ 160 when moving from constant to linear models (compare Figure 6a with 6b, and 6e with 6f), supporting the existence of a lid effect for both Al_2O_3 and λ_1. However, we see contrasting results when the bi-linear model is introduced. For Al_2O_3, evidence values for lin-

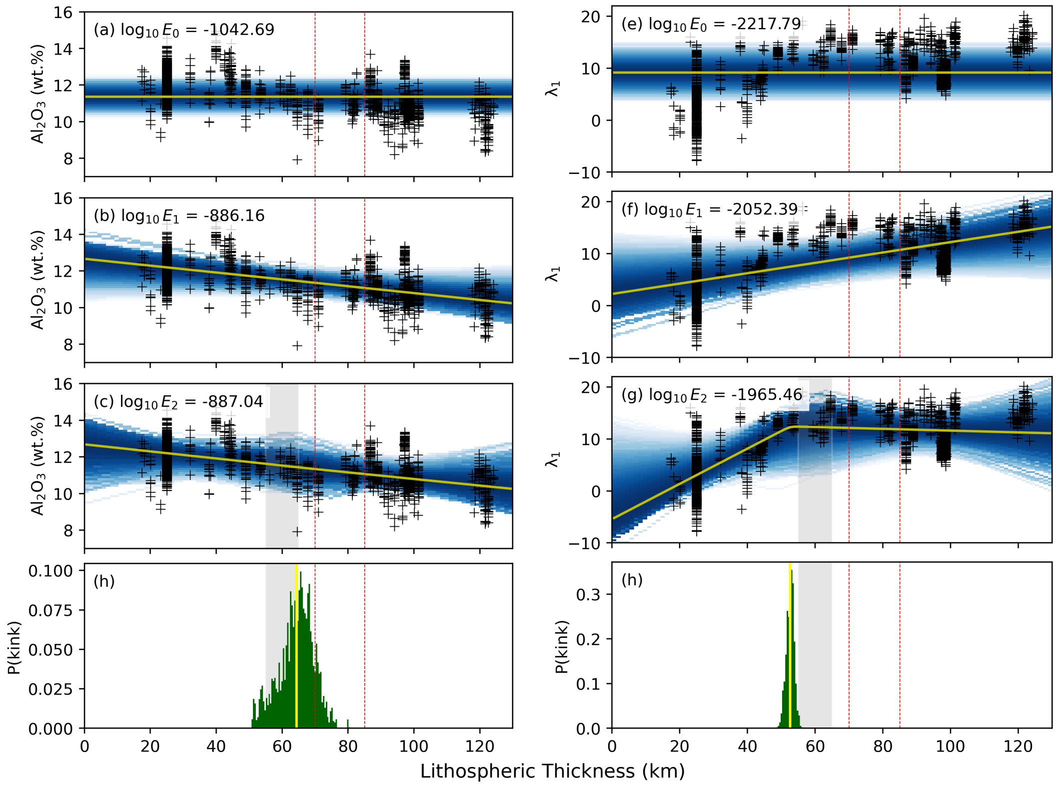

Figure 6. Statistical evidence evaluation results for Al_2O_3 and λ_1 under our reference setup. (a) Al_2O_3 as a function of lithospheric thickness fitted using a constant model; black crosses = individual samples; blue shading = probability density; yellow line = mean model; red dotted lines = expected spinel-garnet transition depths for typical mantle potential temperatures expected in plumes (e.g. Robinson & Wood, 1998; Klemme & O'Neill, 2000; Tomlinson & Holland, 2021); inset gives $\log_{10}$ evidence value. (b) Same for a linear model. (c) Same for a bi-linear model; grey band = prior distribution for kink depth with one standard deviation width. (d) Probability distribution of kink depths, shown as a green histogram; grey band = prior; yellow line = mean value. (e–h) Same as a-d, albeit for λ_1.

ear and bi-linear models are similar (Figure 6b–c), implying the absence of any obvious transition in the trend as a function of lithospheric thickness. The resulting probability distribution of potential kink depths is therefore broad and poorly constrained in Figure 6d, and we infer that Al_2O_3 in OIBs decreases linearly with increasing lithospheric thickness, with no definitive kink. On the other hand, λ_1 shows a clear preference for a bi-linear model, with an increase in the $\log_{10}$ evidence value of ~ 87 over a linear model (Figure 6f–g). The associated probability distribution for the kink is tightly constrained in the depth range of 49–56 km, with an average of ~ 52 km (Figure 6h). Based on this preferred bi-linear model, the most likely trend for λ_1 is that it increases with lithospheric thickness until a depth of ~ 52 km, before subsequently remaining approximately constant.

3.2.2 Summary of Evidence Evaluation Results

Values of $\log_{10}E_1 - \log_{10}E_0$ and $\log_{10}E_2 - \log_{10}E_1$ have been determined for each geochemical parameter, under our reference setup. As a reminder, when greater than a

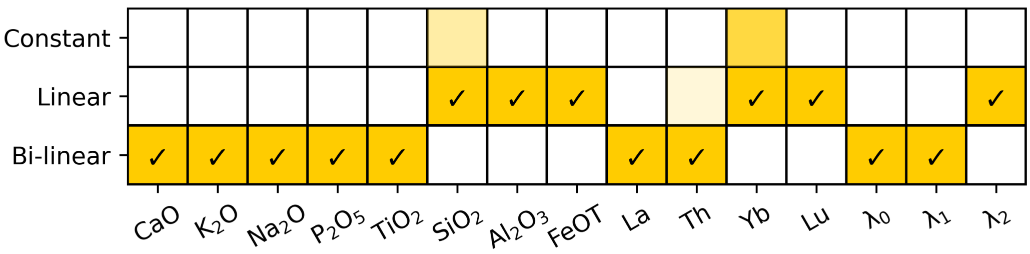

Figure 7. Optimal model type for each geochemical parameter under our reference setup. Ticks denote optimal model; strength of colour fill indicates level of preference for that model type (i.e., when a simpler model has an evidence value that is within 20 but less than 2 of the optimal model, it is filled with colour that linearly increases in intensity).

key threshold value of two (i.e. more than hundred-fold increase in the likelihood), the former indicates statistical preference for a linear model over a constant one, while the latter indicates a bi-linear rather than linear relationship.

The preferred model for each geochemical parameter is shown in Figure 7, with further details in Figures 8–11, and can be summarised as follows:

1. All geochemical parameters prefer either a linear or bi-linear model over a constant model, indicating universal sensitivity to lithospheric thickness.
2. For major elements Al_2O_3, FeO, and SiO_2, data are optimally fitted by linear models (Figure 8). Conversely, TiO_2, Na_2O, K_2O, CaO, and P_2O_5 data are optimally fitted by bi-linear models (Figure 9c–g);
3. For trace elements, the highly incompatible elements La and Th are best fitted by bi-linear models (Figure 9a–b), whereas the less incompatible Yb and Lu are best fitted by linear models (Figure 10);
4. For parameters describing REE patterns, λ_0 and λ_1 are optimally fitted by bi-linear models (Figure 11a–b), whereas λ_2 prefers a linear model (Figure 11c).
5. For geochemical parameters that prefer a bi-linear model, kink depths generally occur at lithospheric thicknesses of 50–60 km.

4 Discussion

4.1 Existence of a Lid Effect

Lithospheric thickness dictates the minimum pressure of plume melting through the so-called 'lid effect'. It affects OIB chemistry in two ways (e.g., Watson & McKenzie, 1991; Humphreys & Niu, 2009; Niu, 2021). First, by inhibiting upwelling beyond a certain depth, lithospheric thickness limits the maximum melt fraction (F). We therefore expect F to be inversely proportional to lithospheric thickness, which will have a substantial impact on the concentrations of highly incompatible trace elements. Second, the pressure at which melting occurs has strong implications for the mineral phases present in the residue following partial melting. In particular, over the depth range of interest here, the stable aluminium-rich phase converts from garnet ($Mg_3Al_2Si_3O_{12}$) to spinel ($MgAl_2O_4$) with decreasing pressure, subsequently becoming plagioclase ($CaAl_2SiO_8$) at shallow depths beneath mid-oceanic spreading centers (e.g., Masaaki, 1980). Despite our analyses being subject to uncertainty, particularly in relation to estimates of lithospheric thickness and assumptions on uniform source composition, the data support a linear or bi-linear trend between all geochemical parameters and lithospheric thickness, providing univer-

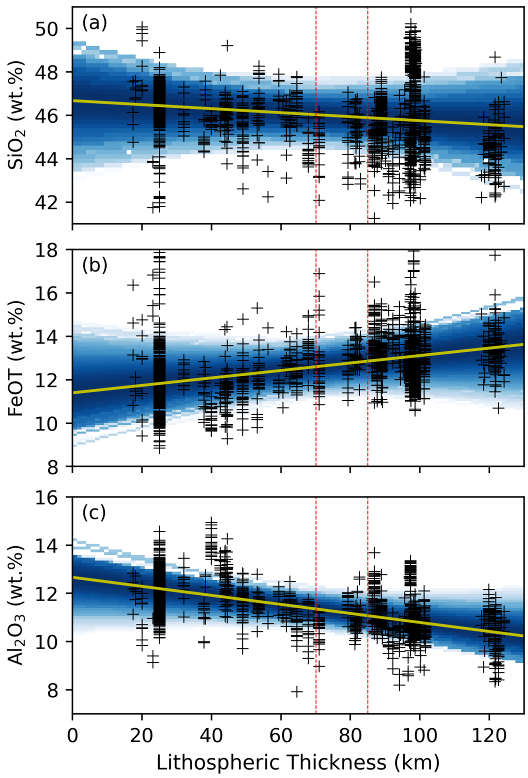

Figure 8. Statistical evidence evaluation results for major elements optimally fitted by linear models, under our reference setup. (a) Results for SiO_2 for all localities; black crosses = individual samples; blue shading = probability density; yellow line = mean model; red dotted lines = spinel-garnet transition depths (e.g., Robinson & Wood, 1998; Klemme & O'Neill, 2000; Tomlinson & Holland, 2021). (b) Same for FeOT. (c) Same for Al_2O_3.

sal evidence for the lid effect and corroborating the conclusions of, for example, Humphreys and Niu (2009), Dasgupta et al. (2010) and Niu (2021).

Nonetheless, it is clear from our results that different geochemical parameters exhibit distinct responses to the lid effect. Some trends (e.g., Al_2O_3) show a linear relationship with lithospheric thickness, whereas others show a bi-linear relationship with an abrupt change at a certain depth (e.g., λ_0, λ_1). In the following sections, we discuss potential explanations for these behaviours. We start with major element trends that are best fitted by linear models, with an emphasis on the relationship to pressure-dependent mineral assemblages. We then discuss the remaining major and trace elements, relating observed trends to the influence of variations in melt fraction and the spinel-garnet phase transition. Although Yb and Lu are best fitted by linear models, we include them in this section because their behaviour is associated with an interplay between F and the spinel-garnet phase transition. We finish by discussing REE trends, described by λ_i, drawing on the lessons learned from the interpretation of trace elements trends.

4.2 Major Elements with Linear Trends

Concentrations of the major elements SiO_2, FeOT and Al_2O_3 in OIBs show a linear dependence on lithospheric thickness (Figure 8). In mantle melts, these components are known to be buffered by the mineral assemblage of the mantle residue and the ob-

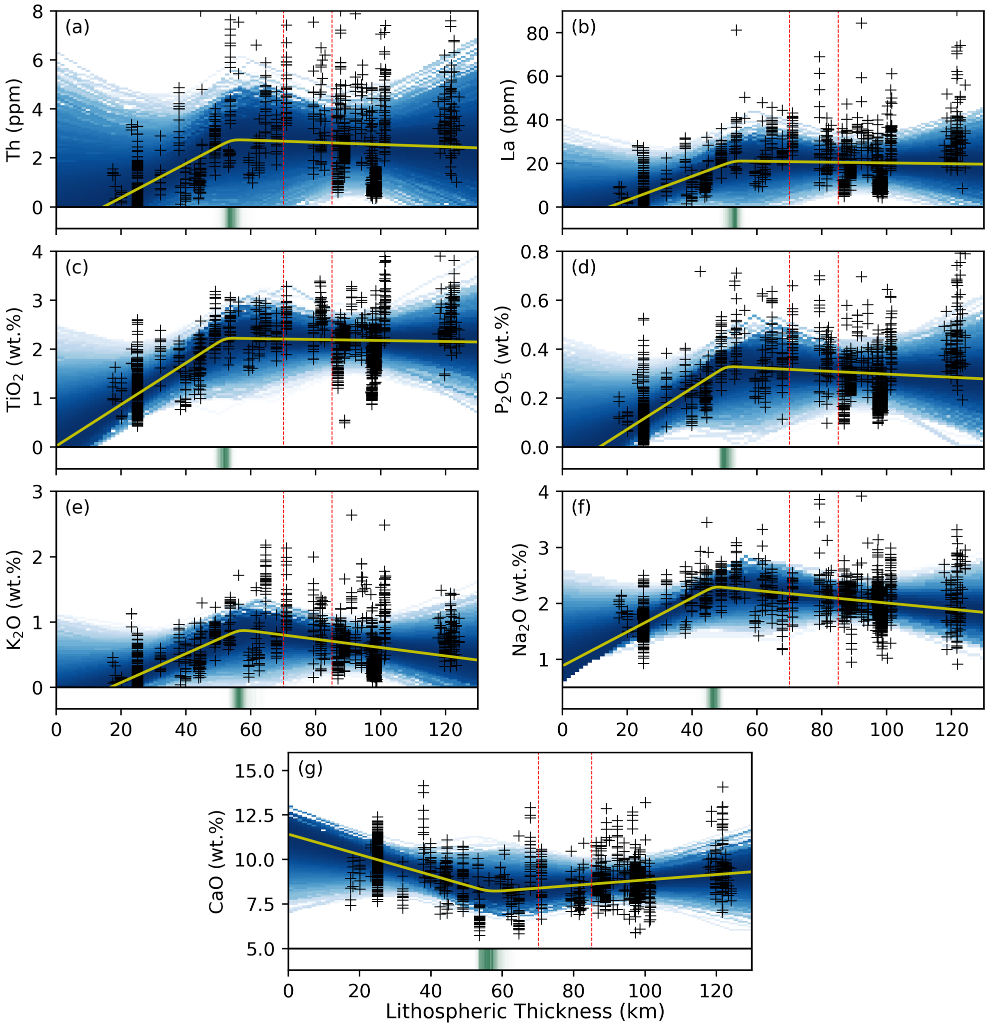

Figure 9. Statistical evidence evaluation results for geochemical parameters optimally fitted by bi-linear models. Data and panel contents same as for Figure 8 but for (a) Th, (b) La, (c) TiO_2, (d) P_2O_5, (e) K_2O, (f) Na_2O, and (g) CaO. The horizontal bar below panel (d) shows the probability distribution of the likely kink depth, with more opaque colors indicating that a kink is more likely at that depth.

served trends are consistent both with experimental studies on the Calcium, Magnesium, Aluminium, Silicon (CMAS) system (e.g., Walter & Presnall, 1994) and with the results of previous observational studies (e.g., Humphreys & Niu, 2009; Niu et al., 2011; Niu, 2021).

SiO_2 exhibits a moderate decrease with increasing lithospheric thickness (Figure 8a). Its concentration in mantle melts is buffered by the two most abundant minerals in the upper mantle, olivine and orthopyroxene, according to the reaction

$$(\mathrm{Mg,Fe})_2\mathrm{SiO}_4 + \mathrm{SiO}_2\,(\mathrm{melt}) \longleftrightarrow (\mathrm{Mg,Fe})_2\mathrm{Si}_2\mathrm{O}_6 \tag{7}$$

Increasing pressure drives this reaction to the right, expanding the stability field of orthopyroxene at the expense of olivine (e.g., Campbell & Nolan, 1974; Walter & Presnall, 1994). As a consequence, as the average melting pressure increases beneath thicker lithosphere, the residue contains more SiO_2-rich orthopyroxene and the corresponding melts

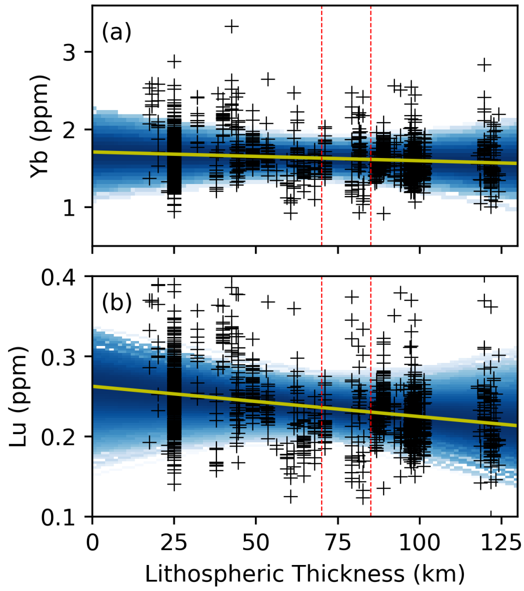

Figure 10. Statistical evidence evaluation results for HREEs, which are optimally fitted by linear models. Data and panel contents same as for Figure 9 but for (a) Yb and (b) Lu.

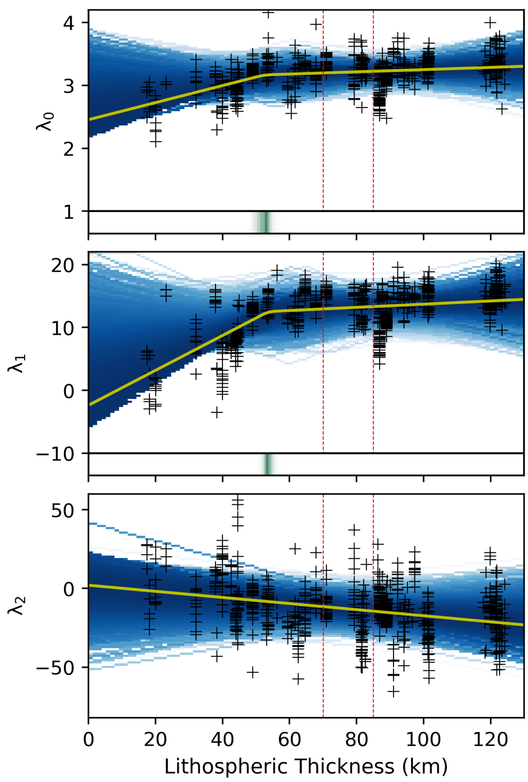

Figure 11. Statistical evidence evaluation results for REE shape parameters. Data and panel contents same as for Figure 9, but for (a) λ_0, (b) λ_1 and (c) λ_2. Note that λ_0 and λ_1 are optimally fitted by bi-linear models, whereas λ_2 is optimally fitted by a linear model.

produced are increasingly SiO_2-poor (e.g., Bohlen et al., 1980; Bohlen & Boettcher, 1981). We note that Herzberg (1992) further proposed that the decrease in SiO_2 with increasing melt pressure stops at ~ 45 wt.% SiO_2 due to low melt fractions in the presence of garnet, but this cut-off behaviour is not observed in either our analyses or in previous studies (e.g., Scarrow & Cox, 1995; Dasgupta et al., 2010). We therefore suggest that the spinel-garnet transition has limited influence on the SiO_2 content of OIBs, with reaction (7) and associated buffering of the silica content by olivine and orthopyroxene being the key control.

We also attribute the linear increase in FeOT with increasing lithospheric thickness (Figure 8b) to the relative stabilities of olivine and orthopyroxene as a function of pressure. Olivine contains more Fe than orthopyroxene and increasing the pressure stabilizes orthopyroxene at the expense of olivine. As a consequence, for similar melt fractions, high-pressure melts contain more Fe than low-pressure melts. The relative abundance of olivine and orthopyroxene in the residue was also used by Niu (2016) to explain the increase in FeOT in mid-ocean ridge basalts (MORB) with increasing ridge axial depth. Analysis of our OIB dataset suggests that this trend can be extended over a greater depth range than is possible with the MORB data alone.

Al_2O_3 linearly decreases with increasing lithospheric thickness (Figure 8c), which we believe can be attributed to an increase in the Al content of clinopyroxene and, to a lesser extent, orthopyroxene, with increasing pressure. Al^{3+} can occupy either the tetrahedral or octahedral sites within the pyroxene crystal lattice. The two tetrahedral sites are characterised by a central cation (usually Si^{4+}) surrounded by four oxygen atoms, whereas the two larger octahedral sites are positions in which the central cation is surrounded by six oxygen atoms and are usually occupied with cations that have greater ionic radii, such as Ca^{2+}. Increasing pressure shrinks the octahedral M1 and M2 sites in both pyroxenes and allows more Al^{3+} to enter the M1 site, which is the smaller of the two octahedral sites (Colson & Gust, 1989). The octahedral Al^{3+} can either be charge balanced by additional Al^{3+} replacing Si^{4+} in an adjacent tetrahedral site according to the reaction

$$\mathrm{Ca_2Si_2O_6} + 2\,\mathrm{Al^{3+}} \longleftrightarrow \mathrm{CaAl_2SiO_6} + \mathrm{Si^{4+}} + \mathrm{Ca^{2+}} \tag{8}$$

or by Na^+ or K^+ replacing a divalent ion on the larger M2 site (Campbell & Borley, 1974; Safonov et al., 2011), according to reaction

$$\mathrm{Ca_2Si_2O_6} + \mathrm{Al^{3+}} + \mathrm{Na^+} \longleftrightarrow \mathrm{NaAlSi_2O_6} + 2\,\mathrm{Ca^{2+}}. \tag{9}$$

As a consequence, the Al_2O_3 content of the residual pyroxenes increases with increasing pressure and the Al_2O_3 concentration in the melt correspondingly decreases. This simple interpretation may be complicated, however, by Al^{3+} being buffered by reactions between spinel and pyroxene in the spinel stability field and between garnet and pyroxene in the garnet stability field. We might therefore have also expected a dependence on the spinel-garnet transition. The fact that our Al_2O_3 trends do not require a bi-linear model in our reference setup suggests that this is not the case, perhaps because both spinel and garnet contain two Al^{3+} ions and the increasing Al content of pyroxenes with pressure is therefore not affected by the spinel-garnet transition.

In summary, we infer that variations in the concentration of major elements SiO_2, FeOT, and Al_2O_3 in OIBs are dominated by gradual changes in mineral assemblage as a function of pressure rather than variations in F or effects arising from the spinel-garnet phase transition.

4.3 Major and Trace Elements with Bi-linear Trends

The behavior of trace elements, which do not form stoichiometric components in minerals, can be understood using the distribution coefficient, D, for the partitioning of the element between a mineral and the melt. During partial melting of mantle peridotite, the concentration of a given element in the aggregate melt (C_l) during batch melting is given by

$$C_\mathrm{l} = \frac{1}{D'(1-F)+F} C_\mathrm{s}, \tag{10}$$

and, in the case of fractional melting, is

$$C_\mathrm{l} = \frac{1}{F}\left[1-(1-F)^{\frac{1}{D'}}\right] C_\mathrm{s}, \tag{11}$$

where D' is the bulk partition coefficient, F is the melt fraction and C_s is the concentration of the element in the source before melting (Shaw, 1970, 1979). C_l is therefore controlled by the combined effect of D' and F. Nevertheless, for incompatible trace elements where D' is low (usually < 0.01), these equations can be simplified to

$$C_\mathrm{l} \approx \frac{1}{F} C_\mathrm{s}, \tag{12}$$

indicating that C_l is proportional to $\frac{1}{F}$, regardless of the melting mechanism. The lower the value of D', the more reliable this approximation becomes. Similarly for moderately low values of D' (i.e. < 0.2), given that melt fractions for OIBs are never higher than ~ 0.2, we can simplify Equations (10) and (11) to

$$C_\mathrm{l} \approx \frac{1}{D'+F} C_\mathrm{s}. \tag{13}$$

In cases where $D' > 0.2$ and differences in the partition coefficients for different minerals are large, which can occur, for example, across the spinel-garnet phase transition, C_l is influenced by both pressure and the phase change. The case of spinel-garnet can be represented by a reaction between spinel and pyroxene to give garnet and olivine according to

$$\mathrm{MgAl_2O_4\,(Spinel) + 2\,Mg_2Si_2O_6 \longleftrightarrow Mg_3Al_2Si_3O_{12}\,(Garnet) + Mg_2SiO_4}. \tag{14}$$

The transition is abrupt and temperature dependent (e.g. Klemme & O'Neill, 2000). For temperatures appropriate for mantle plumes, the transition occurs over a ~ 5 km depth range somewhere between 70–85 km, depending on the mantle composition (e.g. Robinson & Wood, 1998; Klemme & O'Neill, 2000; Wood et al., 2013; Tomlinson & Holland, 2021). Note that the shallower plagioclase-spinel transition in peridotite is not relevant to this study because the plagioclase stability field extends only to pressures of 0.8 GPa in fertile lherzolite and to 0.6 GPa in depleted lherzolite, corresponding to depths of 24 km and 18 km, respectively (Borghini et al., 2010).

For geochemical parameters that are best fitted by bi-linear models, we divide them into two groups: (i) elements exhibiting low partition coefficients ($D' < 0.2$), including Th, La, Ti, P, K and Na, which we propose can be interpreted primarily in terms of melt fraction F (although Na and K may be further influenced by D values for pyroxenes at high pressure); and (ii) Ca, which requires consideration of both F and the spinel-garnet phase change. These bi-linear trends were not identified in previous studies (e.g., Ellam, 1992; Humphreys & Niu, 2009; Dasgupta et al., 2010; Niu et al., 2011; Niu, 2021) and we discuss their likely origin.

4.3.1 Incompatible elements

D' values for the incompatible elements investigated in this study decrease in the following order: Ti $\approx$ P $\approx$ Na $>$ La $>$ K $>$ Th. All are optimally fitted by bi-linear models, in which their concentrations initially increase rapidly with increasing lithospheric thickness, before remaining flat or increasing at a significantly reduced rate in the cases of Th, La, Ti, P, or slightly decreasing in the cases of K and Na. The kinks in slopes all occur at 50–60 km depth (Supplementary Figure S3).

Table 1. Partition coefficients for incompatible elements in the main peridotite minerals. D'_{sprd} and D'_{gprd} are bulk partition coefficients for spinel peridotite (assuming model abundances of 59% Ol, 28% Cpx, 8% Opx, 5% Sp) and garnet peridotite (55% Ol, 23% Cpx, 15% Opx, 7% Grt), respectively. D in each mineral can vary as a function of mineral composition, temperature and pressure.

	Ol	Opx	Cpx	Sp	Grt	D'_{sprd}	D'_{gprd}
Th	0.0001	0.0001	0.00026	0.00001	0.0001	0.00014	0.00014
K	0.00018	0.001	0.002	0.0001	0.001	0.00075	0.00078
La	0.0004	0.002	0.054	0.01	0.01	0.016	0.014
Ti	0.02	0.1	0.18	0.15	0.28	0.078	0.087
P	0.1	0.03	0.05	0	0.1	0.075	0.078
Na	0.006	0.05	0.2	0	0.04	0.064	0.060
Lu	0.0015	0.06	0.28	0.01	7.7	0.085	0.61
Yb	0.0121	0.1036	0.5453	0.01	6.9	0.17	0.63

La, K and Th are highly incompatible in peridotites, regardless of whether the major aluminum-rich phase is spinel or garnet ($D' \leq 0.01$; Table 1). Following on from our interpretation of Equations (12) and (13) for such elements, at constant potential temperature, we expect variations in their concentration to be proportional to $\frac{1}{F}$ as a function of lithospheric thickness and insensitive to the spinel-garnet phase transition (dashed line in Figure 12a). This behaviour should impart an increase in incompatible trace element concentrations at larger thicknesses, with a steeper rate of increase at greater thicknesses. This prediction is consistent with the observed increase in incompatible element concentrations with increasing lithospheric thickness beneath thinner lithosphere. When lithospheric thickness exceeds 50–60 km, however, it is not consistent with the slightly increasing, flat or decreasing concentrations observed. We can further demonstrate this aspect by converting our observed concentrations of La into estimates of F as a function of lithospheric thickness (solid purple line in Figure 12a) and comparing it to the predicted F curves (note that the resulting F curve is insensitive to the choice of La or Th). There is an agreement between the shapes of the two curves for lithospheric thickness < 55 km but they become inconsistent at larger thicknesses, implying that another process modulates concentrations of incompatible elements beyond thicknesses of ~ 55 km. The most important conclusion that can be drawn from the analyses of highly incompatible Th and La is that F remains nearly constant for lithosphere thickness > 55 km.

The moderately incompatible elements Na, P and Ti have $D' \sim 0.06 - 0.08$ in both the spinel and garnet stability fields and follow similar trends. For these elements, D' cannot be neglected and Equation (13) should be used to interpret changes in their concentrations. Since D' varies little with mineralogy for these elements, it can be regarded as a constant and F becomes the dominant variable. As a consequence, experimental and theoretical constraints imply that these moderately incompatible element concentrations should again increase with increasing lithospheric thickness, with steeper rates of increase at greater thicknesses. The contribution from D' should reduce the effect of F, diluting the concentration ratio of these elements between the melts and residue at higher pressures without altering the underlying trend. This prediction is consistent with observations for lithospheric thicknesses less than 55 km, but it is inconsistent with thicker lithosphere trends, which again suggest minimal changes in F at larger thicknesses. This aspect is important to keep in mind for the following interpretations.

Our analyses demonstrate that the concentrations of Na and K differ from other incompatible elements in that they show a slight decrease with increasing lithospheric thickness beyond the kink (Figure 9e and f). At these pressures, F is expected to be small

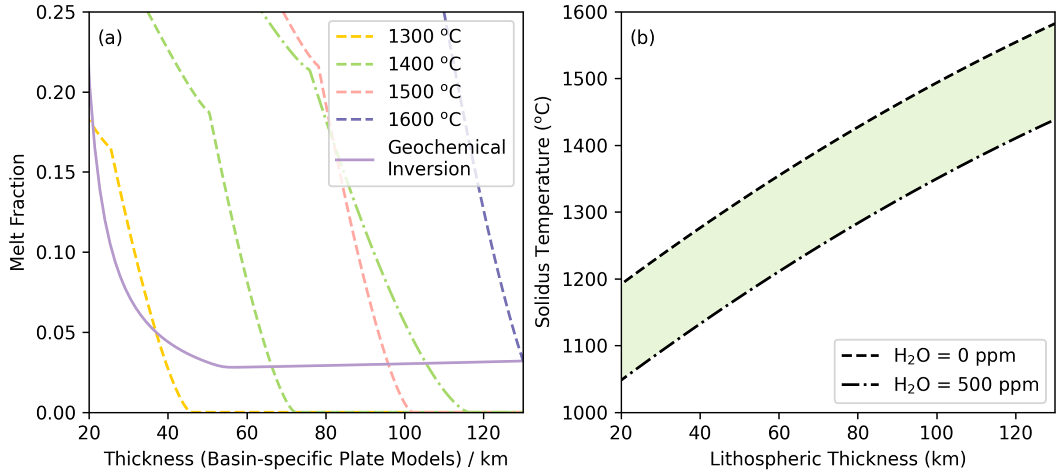

Figure 12. (a) Solid line = melt fraction (F) as a function of lithospheric thickness inferred from Equation (10) and the bi-linear trends for La concentrations, with basin-specific plate model-derived estimates of lithospheric thickness; dashed lines = theoretical melt fraction for decompression melting of dry, primitive peridotite at different potential temperatures from the parameterisation of Katz et al. (2003), as modified by P. W. Ball et al. (2022); dash-dotted line = same for a wet 1400°C source with H_2O = 500 ppm, which is thought to be an upper bound for water content in plume source regions (e.g., Wallace, 1998; Asimow & Langmuir, 2003). (b) Solidi for peridotite with 0–500 ppm water contents.

and to remain nearly constant with increasing lithospheric thickness. The observed trends in Na and K may therefore indicate that variations in D' are playing a role. As discussed in Section 4.2, increasing pressure allows entry of Al^{3+} into the clinopyroxene M1 site. Via reaction (9), this substitution can be charge balanced by replacing a X^{2+} cation in the larger M2 site with Na^+ and/or K^+, resulting in an increase of D' for K^+ and Na^+ with increasing pressure. With minimal changes in F, this effect may explain their observed decrease in concentration with increasing lithospheric thickness, relative to highly incompatible La and Th, although we note that Na^+ is expected to have a stronger affinity for the M2 site than K^+ because its ionic size is closer to the size of the site (Safonov et al., 2011).

4.3.2 CaO

Calcium is the element most likely to be affected by the spinel-garnet transition because garnet contains stoichiometric Ca, whereas spinel does not. The principal repositories for Ca^{2+} in garnet peridotites are, in order of decreasing affinity, clinopyroxene > garnet > orthopyroxene > olivine. Beneath shallow lithosphere, there is a steady decrease in CaO concentration with increasing lithospheric thickness up to $\sim$ 55 km (Figure 9m–n). We attribute this behaviour to the continuous decrease in F, previously deduced from analyses of incompatible element trends: as F decreases, less clinopyroxene melts and the resulting melt has a lower Ca concentration. Our interpretation of the incompatible element trends suggests that, beyond the kink, F should remain approximately constant or continue to decrease, but at a reduced rate. Therefore, we would expect a further decrease in CaO (albeit at a lower rate), rather than the increase that is observed. The cause of this increase is unclear, but assuming that F is not changing (as suggested by the most incompatible elements), it requires that, with increasing pressure, a Ca-rich phase (presumably Ca-rich pyroxene) melts in preference to moderately Ca-poor garnet and orthopyroxene. We note that previous studies, which applied linear regression to the data, found no discernible trend between CaO and lithospheric thickness (e.g., Humphreys & Niu, 2009), probably because the reversal in trends from decreasing to increasing CaO counteract each other.

4.3.3 Yb and Lu

Concentrations of Yb and Lu change little with increasing lithospheric thickness, showing only a slight, linear decrease (Figure 10). This behaviour occurs even though these elements exhibit an order of magnitude difference in compatibility between spinel (incompatible) and garnet (compatible; Table 1), from which we might expect to see a kink in their trends.

Within the spinel stability field, the decrease in F with increasing pressure, required by the incompatible trace element trends, is offset by increasing D' due to an increasing amount of clinopyroxene in the residue at higher pressures (e.g., Green & Ringwood, 1967). Within the garnet stability field, the constant or slight decrease in F with increasing lid thickness is initially offset by an increase in D' as garnet replaces spinel and, subsequently, as pressure continues to increase, by garnet partially replacing pyroxene according to reaction (14).

Superimposed on these changes is the migration of low Yb-Lu melt from the garnet zone into the spinel zone, where it partially offsets the potential increase in the concentration of these elements due to their lower D' in the spinel zone. This behaviour is termed the 'memory effect', whereby erupted melts preserve a geochemical memory of high-pressure melting despite melting continuing to shallower depths (e.g. Elliott et al., 1991). The relative proportions of melt from the spinel and garnet zone are also critical in determining melt composition: increasing pressure can increase Yb-Lu concentrations in melts within the spinel zone while simultaneously reduce the melt volume within that zone, thus limiting low-pressure melts' impact on determining the final average Yb-Lu concentration and resulting in an decrease of Yb-Lu with increasing lithospheric thickness. Overall, the combined impact of the competing influences of increasing F, especially within the spinel zone, changes in D' as garnet is replaced by spinel, and the systematic decrease in the proportion of melt coming from the spinel zone with increasing pressure, can plausibly explain the slight decrease in Yb and Lu concentrations with increasing lithosphere thickness. Taken together, this result implies that the absence of a kink in Yb-Lu trends, which might be expected from the spinel-garnet phase transition, is obscured by the memory effect.

4.4 Shape of REEs

We next discuss the shape parameters, λ_i, for REE concentration patterns (O'Neill, 2016). λ_0 is the average of the logarithmic concentration of all REEs except Eu, normalised by each element's concentration in chondrites. Increasing lid thickness reduces the melt fraction, thereby elevating the concentration of highly incompatible LREEs (Figure 9) while having a limited effect on the concentration of HREEs (Figure 10). It is therefore not surprising that λ_0 follows trends defined by the highly incompatible elements, with a kink at ~ 55 km (Figures 11a).

λ_1 measures the enrichment of LREEs relative to HREEs and has a bi-linear trend, similar to λ_0 (Figure 11b). Previous studies described variations in REE trends using ratios, such as La/Yb and Sm/Yb, and related observed changes to an increasing abundance of garnet in the residue as the melting pressure increases (e.g., Ellam, 1992; Humphreys & Niu, 2009). However, these studies did not recognise either a kink or the influence of changes in F on LREE and, hence, the slope of the REE pattern. As noted in connection with λ_0, the LREEs initially increase with increasing lithospheric thickness to ~ 55 km

(Section 4.3.1), driven by changes in F, then remain nearly constant, while HREE concentrations change little throughout (Section 4.3.3). Therefore, the combined behaviour of LREEs and HREEs accounts for the observed variation in λ_1.

λ_2 quantifies the curvature of the REE pattern. As outlined by O'Neill (2016), values are positive if amphibole remains in the residue following melting and transitions from positive to negative if more garnet remains. OIBs are dry relative to arc magmas, so amphibole is not expected to play a role in their genesis (e.g., O'Neill, 2016). To examine the sensitivity of λ_2 to melting depth, we consider a two-stage melting model (Supplementary Table S6), in which partial melting begins in the garnet zone and extends into the spinel zone, with mixing permitted between melts from both zones. For melting in the garnet zone, λ_2 becomes more negative as both F and the amount of garnet in the residue increase. For melting in the spinel zone, λ_2 is positive when F is low, but decreases as F increases. When melts from both zones mix, the effect is cumulative. λ_2 is also sensitive to source composition: melts generated from a primitive mantle source have higher λ_2 values than those from a depleted mantle source (Supplementary Table S6). These insights imply that interpretations of λ_2 are complex, although certain inferences can be made.

Figure 11c shows that λ_2 linearly decreases with increasing lithospheric thickness. At lithospheric thicknesses greater than ~ 55 km, the majority of λ_2 values are negative and the trend becomes increasingly negative as the lithosphere thickens. Assuming that total F changes little after the kink, as is implied by the trends identified for highly incompatible elements, and there is no mixing of melts from the spinel and garnet zones (which is plausible given that the lid should act as a barrier to melting above the spinel-garnet transition depth), based on the two-stage model outlined above, we infer that the amount of garnet in the source increases with pressure at lithospheric thicknesses exceeding those of the kink, as expected. When lithospheric thickness is less than 55 km, assuming all melts are generated in the spinel zone and there is no mixing with melts from the garnet zone, as the lithosphere thickens, F will decrease and λ_2 will increase. This is inconsistent with the trend that we have identified for λ_2 (Figure 11c), which decreases across all lithospheric thicknesses. This can be plausibly explained if a larger proportion of garnet melts mixed with a smaller proportion of spinel melts as lithospheric thickness and pressure increase (decreasing total F – e.g., primitive mantle starting to melt from 4 GPa, if $F(0.06) = F_{\mathrm{grt}}(0.01) + F_{\mathrm{spl}}(0.05)$, $\lambda_2 = 7.26$; if $F(0.04) = F_{\mathrm{grt}}(0.03) + F_{\mathrm{spl}}(0.01)$, $\lambda_2 = 1.86$), providing further evidence for the memory effect when melts are generated under thin lithosphere (e.g., Elliott et al., 1991).

4.5 Trend Robustness

To analyse the robustness of our results to initial OIB processing steps, potential bias towards heavily sampled localities, and/or choice of lithospheric thickness model, we evaluate Bayes factors for a suite of additional scenarios including: (i) filtered OIB data prior to- and post-corrections for fractional crystallisation; (ii) a sub-sample of the OIB dataset, where a percentage of samples are randomly removed; (iii) datasets where Iceland and Hawaii samples are included/excluded; and (iv) lithospheric thickness obtained from the basin-specific plate-cooling models versus a model derived from seismic tomography. A summary of these results are presented in Figure 13, with further plots presented in Supplementary Figures S4–S5.

4.5.1 Correction for Fractional Crystallisation

Our reverse-fractionation calculations in Petrolog3 suggest that primitive OIB melts commonly undergo 5–25% fractional crystallisation in the magma chamber (Supplementary Figure S6). Correcting for fractional crystallisation does alter absolute geochemical concentrations, but the preference for a linear over constant dependence on litho-

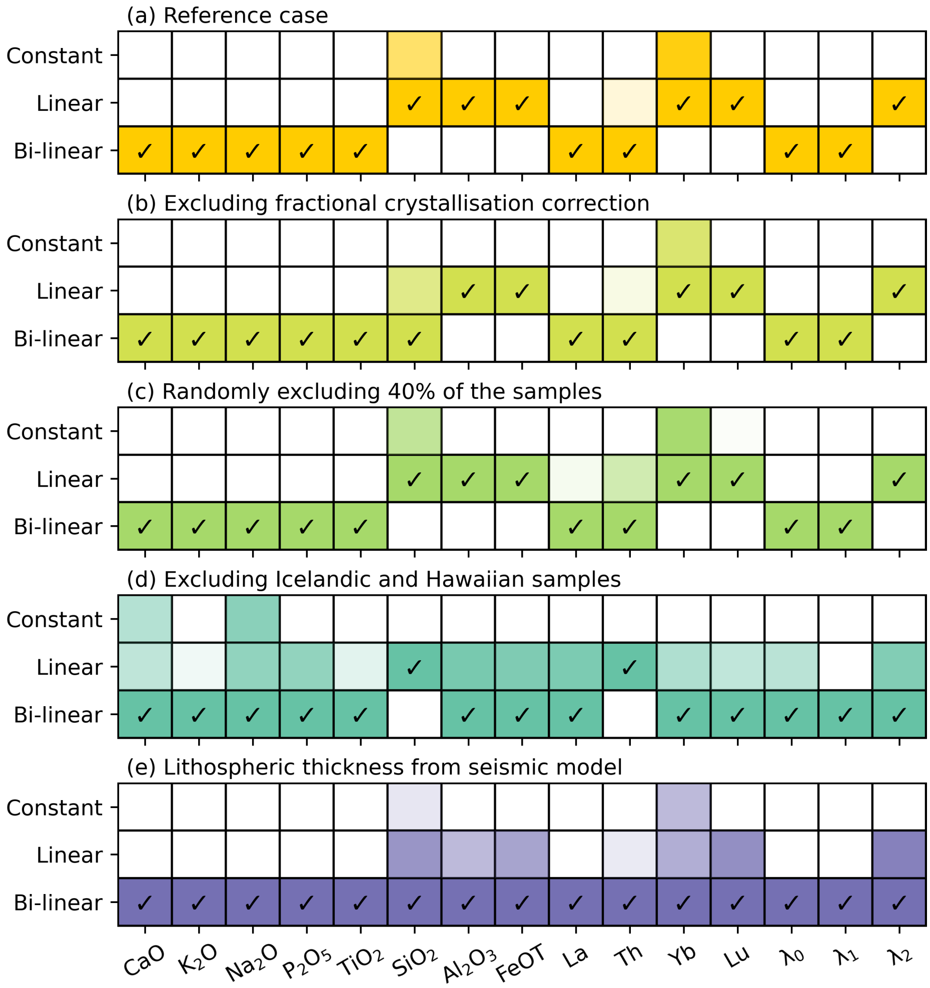

Figure 13. (a) Optimal model type for each geochemical parameter under our reference setup (filtered OIB samples from all localities corrected for fractional crystallisation, with lithospheric thicknesses from basin-specific plate-cooling models; as in Figure 7). (b) Same as the reference setup except data are not corrected for fractional crystallisation. (c) Same as the reference setup except 40 % of the data are randomly removed. (d) Same as the reference setup except Icelandic and Hawaiian samples were excluded. (e) Same as the reference setup albeit with lithospheric thickness taken from the model based on seismic tomography.

spheric thickness remains unchanged for all major and minor elements, and REE shape parameters (Figure 13b). In most cases, the preference for either linear or bi-linear models also remains unchanged, the exception being SiO_2, for which the non-corrected data shows a preference for a bi-linear model. This behaviour is a direct consequence of imposing the $SiO_2 > 43$ wt.% filtering criteria: for the non-fractionation corrected data, this results in a hard cut-off of all data below this value and preferentially increases preferred model values in thicker lithosphere, whereas following fractionation correction, the kink is smoothed out and SiO_2 linearly decreases with increasing lithospheric thickness (Supplementary Figures S7 and S8).

4.5.2 Data Subsets

The possibility of bias from specific samples was tested by removing some data to see if the observed trends remain - so-called bootstrapping. We randomly removed 20% and 40% of all OIB samples while keeping all other variables consistent. In most of these tests, the preferred model and the trend for each of the geochemical parameters did not change (Figure 13c). Exceptions occurred when the preferred model was close to the edge of a threshold before removing some samples. Nonetheless, our overall interpretation remains valid, and the observed geochemical trends are not strongly affected by sampling bias.

4.5.3 Heavily Sampled Localities

Hawaii and Iceland are heavily sampled in comparison to other localities in our OIB database, yielding high-density data clusters that may potentially introduce bias into the results. Nevertheless, we find that excluding these sites does not generally alter evidence in favour of the lid effect. For all geochemical parameters, there is still strong preference for either a linear or bi-linear model over a constant one. The two exceptions occur for Ca and Na, where the evidence with respect a constant model is still greater than 2 but less than 20 (Figure 13d).

With regards to preference for a bi-linear versus linear fit, removal of these localities has more of an influence on results. For geochemical parameters where all sites are optimally fitted by bi-linear models, excluding Iceland and Hawaii can either increase or reduce values of $\log_{10}E_2 - \log_{10}E_1$, depending on the parameter (Supplementary Figure S4a and e). In general, more parameters transition to preferring a bi-linear model (e.g., Al_2O_3, FeOT, Yb, Lu and λ_2), with Si maintaining preference for a linear model and only Th switching from a bi-linear to linear model. This indicates that evidence in favour of bi-linear trends is not attributable to potential sampling bias from Hawaii and Iceland.

Nevertheless, it is interesting to note that excluding Icelandic and Hawaiian samples has an impact on the slope of the trend in thick lithosphere (beyond the kink depth of ~ 55 km). For incompatible elements Th, La, TiO_2 and P_2O_5, the slope after the kink increases (Supplementary Figure S9), which is also the case for λ_0 and λ_1 (Supplementary Figure S10), albeit still at a lower rate than would be expected from theoretical arguments for melting at constant potential temperature and composition. For Na_2O and K_2O, it reduces the rate of concentration decrease with increasing lithospheric thickness (Supplementary Figure S9). All of these differences can likely be attributed to the concentrations of incompatible elements in Hawiian basalts being lower than those of other OIBs on lithosphere of similar thickness. As noted in Section 2.4, Hawaiian basalts are dominated by tholeiites, whereas all other OIBs on thick lithosphere have alkali basalt affinities. Tholeiites are produced by higher degrees of partial melting (e.g., Yoder Jr & Tilley, 1962) and concentrations of incompatible elements are therefore expected to be diluted, which is consistent with the Hawaiian plume being hotter and stronger than other plumes beneath thick lithosphere (e.g., Hoggard, Parnell-Turner, & White, 2020). Hawaiian OIBs may also originate from a source that is more depleted in highly incompatible elements if, as suggested by Hofmann and Jochum (1996) and Pietruszka et al. (2013), it contains a significant amount of recycled oceanic gabbro. Regardless of the exact nature of the Hawaiian plume, its distinctive characteristics, coupled with the large number of samples available, can influence the slope of geochemical trends in thick lithosphere but does not refute evidence for the lid effect.

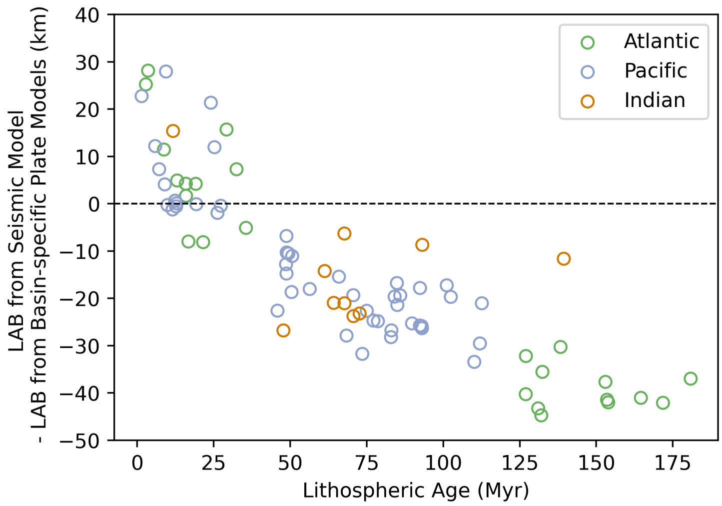

Figure 14. Difference between local lithospheric thickness beneath each island from the seismic model and that predicted by the basin-specific plate models, as a function of lithospheric age at time of OIB eruption. Localities in the Atlantic, Pacific and Indian Oceans are represented by green, blue and red circles, respectively.

4.5.4 Alternative Estimates of Lithospheric Thickness

As introduced in Section 2.2, a limitation of theoretical cooling models is that they cannot capture local deviations in lithospheric thickness away from the average value for ocean floor of a given age (e.g., D. R. Davies et al., 2019). By comparing expected values with local estimates obtained from seismological constraints, we demonstrate that there are systematic differences between the two at the sites of OIBs in our database (Figure 14). For ocean islands on lithosphere younger than ~ 30 Ma, such as at Easter Island or the Azores, seismically inferred estimates of local lithospheric thickness systematically exceed expectations from plate-cooling models. This offset is likely artificial, being a consequence of surface wave tomography having limited resolution at depths shallower than ~ 75 km and therefore smearing shallow velocity structure into greater depths in regions of thin lithosphere (see Section 2.2). For older lithosphere on the other hand, seismically inferred estimates of present-day lithospheric thickness beneath each ocean island are consistently thinner than expectations from plate models. In contrast to the artifacts in regions of thin lithosphere, this observation is likely real and probably reflects destabilisation and thinning of the lithosphere by the underlying mantle plume (e.g., G. F. Davies, 1994; Dumoulin et al., 2001). As a consequence of these two effects, the majority of lithospheric thickness estimates beneath OIBs from the seismic model fall in the 40–100 km range, which is slightly narrower than the associated range of 30–120 km from plate-cooling models.

When switching to estimates of lithospheric thickness inferred from the seismic model, we find that all geochemical trends are best fitted by bi-linear models, including those that display linear trends when using lithospheric thickness from basin-specific plate models (Supplementary Figure S4f). In particular, there is a moderate preference ($5 < \log_{10} E_2 - \log_{10} E_1 < 10$) for bi-linear models in the cases of Al_2O_3, FeO and Yb, as well as a slight preference ($2 < \log_{10} E_2 - \log_{10} E_1 < 5$) in the cases of SiO_2, Lu, and λ_2. Nevertheless, constant models still perform poorly (Figure 13e), and our dataset displays robust evidence for existence of the lid effect.

4.6 Processes Contributing to Observed Geochemical Trends

In our reference setup, bi-linear trends generally fall into two categories: (i) the highly incompatible elements (Th, K, La, P, Ti, Na), in which concentrations are entirely controlled by melt fraction and therefore indicate that F remains approximately constant at lithospheric thicknesses greater than that of the kink; and (ii) for CaO and parameters describing REE patterns (λ_0 and λ_1), where the depth of the kink is being determined by the combined effects of changing melt fraction interacting with the spinel-garnet phase transition. For the latter, the role of this phase change is to maintain HREE concentrations with increasing lithospheric thickness, while allowing the concentration of the LREE to continue to increase as F reduces.

It is important to note that the kinks in our bi-linear trends may not, in reality, reflect sharp change points, but rather a gradual transition in the trend as a function of increasing lithospheric thickness. While our findings show that the kink is generally identified at a depth of 50–60 km (Supplementary Figure S3), since these trends are sensitive to both variations in F and the spinel-garnet phase transition, it is incorrect to infer the phase transition depth directly from the kink depth. This point is further emphasised by the fact that we observe garnet signatures in some OIBs that are generated beneath thin lithosphere (e.g., through trends of Yb, Lu, λ_2), which can be attributed to the memory effect of high-pressure melts from the garnet stability field incompletely mixing with lower pressure melts from the spinel stability field.

Our resulting inferences of melt fraction as a function of lithospheric thickness (Figure 12a) suggest that, beyond a certain lithospheric thickness, F becomes approximately constant. This behaviour is unexpected since, based on the lid effect and theoretical models of plate cooling, we would expect lithosphere to continue to thicken and, all other aspects being equal, cause a continuous reduction in F. One potential explanation for this behaviour could be progressive thinning of overlying lithosphere by upwelling plume material. Small-scale convection above mantle plumes is known to be more prevalent beneath thicker lithosphere (e.g., Dumoulin et al., 2001; van Hunen et al., 2003; Ballmer et al., 2011; Le Voci et al., 2014; D. R. Davies et al., 2016; Duvernay et al., 2021), making it more likely that the base of older lithosphere would become unstable upon plume impingement. This argument is supported by our observation in Section 4.5.4 and Figure 14 that seismically inferred estimates of lithospheric thickness are consistently thinner than those predicted by plate-cooling models in older lithosphere. Accordingly, beyond the $\sim$ 55 km kink depth, lithospheric thickness above mantle plumes is unlikely to increase at a rate consistent with cooling model expectations, thereby reducing the rate of the expected reduction in melt fraction. A further contributing factor is that, since the solidus temperature increases with pressure (Figure 12b), weaker plumes with lower excess temperatures may fail to cross the solidus and generate melt beneath thick lithosphere. This effect would be compounded by the fact that weaker plumes generate smaller melt volumes that are more likely to get trapped at depth and not erupt onto the seafloor. We refer to this behaviour as the 'temperature effect' and have investigated two lines of independent evidence that might support it.

First, we have explored potential relationships between lithospheric thickness and the potential temperature of OIB sources as estimated from geochemical or geophysical arguments (e.g., Putirka, 2008; P. Ball et al., 2021; Bao et al., 2022, Supplementary Figure S11). No clear patterns have emerged (although such estimates are known to be uncertain; e.g., Herzberg et al., 2007; Bao et al., 2022). Secondly, we have compared lithospheric thickness to recent analyses of plume buoyancy flux from Hoggard, Parnell-Turner, and White (2020). Here, we find that magmatic plumes beneath thicker lithosphere generally have higher buoyancy fluxes, potentially indicative of higher excess temperatures (Figure 15). This observation is consistent with the suggestion that, beyond the kink depth, melt fractions are approximately constant due to preferential sampling of progressively

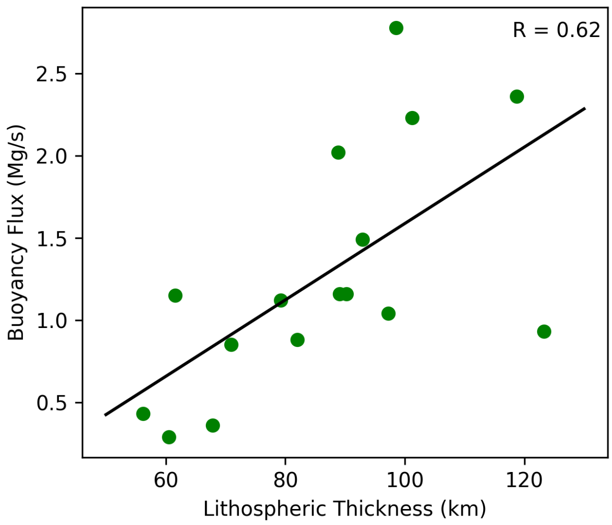

Figure 15. Relationship between buoyancy flux of magmatic plumes from Hoggard, Parnell-Turner, and White (2020) and lithospheric thickness estimated from the basin-specific plate models (for values greater than the kink depth of ~ 55 km).

hotter plumes from regions of thicker lithosphere (i.e., the rate of decrease in F is at least partially offset by the increase in plume temperature).

Taken together, local variations in lithospheric thickness away from average expectations from theoretical cooling models, sampling biases associated with progressively hotter plumes in regions of thicker lithosphere, and source region heterogeneities, are all plausible contributors to observed incompatible element trends.

4.7 Limited Evidence for Melt Re-equilibration at Base of Lithosphere

Both Iceland and Hawaii have a large number of samples and exhibit a wide spread of compositions (e.g. Figure 16). Previous studies have attributed these ranges to variations in the fertility of the mantle source (e.g., Humphreys & Niu, 2009; Niu et al., 2011; Jones et al., 2017). Furthermore, Niu (2021) have also suggested that none of this spread can be attributed to differences in the initial melting pressure (i.e. there is no memory effect), since OIB melts re-equilibrate with the surrounding mantle during their ascent to the surface. Melting in an ascending mantle plume is expected to occur over a depth range of several tens of kilometres. If such re-equilibration reactions do occur, however, we would expect major element concentrations buffered by olivine and pyroxene to be strongly homogenised, while highly incompatible trace elements (e.g., Th, K and La) that have $D' < 0.01$ in both the garnet and spinel stability fields should retain their original spread.

Our analyses have found no evidence to support such a process for re-equilibration of plume-derived melts: in other words, we find robust evidence for preservation of geochemical signatures across a range of depths in erupted melt products (i.e., the memory effect). OIBs from Hawaii and Iceland, for example, show a negative correlation between SiO_2 and FeOT (Figure 16a–b), which can be attributed to melts generated at a range of different pressures and has previously been suggested to occur in many OIBs (e.g., Scarrow & Cox, 1995). In the case of Iceland, most of the data cluster at ~ 46.5 wt.% SiO_2, but some samples extend towards ~ 42 wt.% SiO_2. The high SiO_2 samples could relate to melts generated at low pressure, while samples with lower SiO_2 are gen-

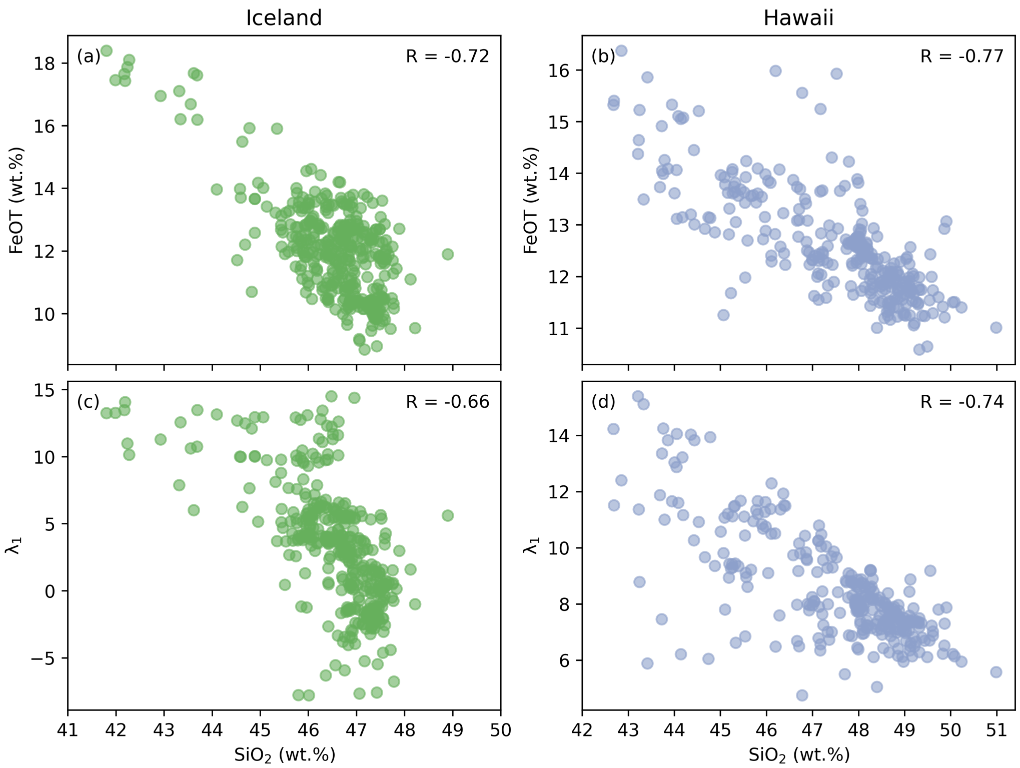

Figure 16. Co-variation of pressure-sensitive geochemical parameters for OIB samples located at Iceland and Hawaii. (a) FeOT as a function of SiO_2 for Icelandic samples, following application of filtering and corrections for fractional crystallisation. (b) Same for Hawaiian samples. (c–d) Same for λ_1 values as a function of SiO_2.

erated by smaller degrees of melting at higher pressure. There is also a cluster of samples at the high SiO_2 end of the Hawaiian array, albeit at 48.5 wt.% SiO_2, with the data more evenly spread across the array. As with Iceland, we suggest that the low-SiO_2, high-FeOT basalts at Hawaii are produced by melts separating from the mantle at depth (i.e. far below the lithospheric lid) and that they have subsequently erupted without undergoing re-equilibration during their ascent.

Importantly, whilst variations in FeOT at a given SiO_2 can potentially be explained by mantle source heterogeneity, the correlation between SiO_2 and λ_1 provides convincing support for melting across a range of pressures without complete homogenisation and mixing (Figure 16c–d). Melt re-equilibration would be expected to bound major element concentrations within a limited range, but have little impact on incompatible trace element concentrations. Accordingly, following re-equilibration, limited correlation would be expected between major and trace elements, which is not borne out by our observations.

5 Conclusions

Our study yields insights into the role of lithospheric thickness variations in influencing the geochemical characteristics of OIBs. Our results support existence of the lid effect, in which lithospheric thickness limits the lowest melting pressure of upwelling mantle plumes and has an important influence on OIB geochemistry. Our statistical analyses suggest that REE patterns, and major and trace element concentrations, are influenced by lithospheric thickness, with some geochemical parameters best fitted by linear trends and others by bi-linear trends with a kink at thicknesses of 50–60 km. Although other factors such as source heterogeneity, melts separating from the mantle at various depths below the lid, and bias from heavily sampled localities are excepted to influence OIB geochemical trends, the observed trends remain overall consistent with expectations from the lid effect.

Such trends can be explained by a combination of pressure-driven changes in melt fraction and mineral assemblage, especially the spinel-garnet transition. The behavior of highly incompatible elements suggests that the melt fraction decreases rapidly with increasing lithospheric thickness until thicknesses reach $\sim 55\,\mathrm{km}$, but subsequently decreases at a significantly lower rate with increasing thicknesses. This behaviour is inconsistent with theoretical expectations based solely on the lid effect and suggests that: (i) plumes impinging beneath thicker lithosphere may be more effective at thinning the overlying lid, thereby modulating changes in melt fraction; and (ii) only melts from plumes with higher potential temperatures can penetrate thick lithosphere and reach the seafloor, consistent with solidus temperatures increasing with pressure and evidence that magmatic plumes under thicker lithosphere have higher buoyancy fluxes.

The depth of the spinel-garnet transition zone cannot be directly identified from the trends observed herein. Nonetheless, the signature of this phase transition is evident in observed trends for Yb, Lu, and λ_2. These trends require that a signature of melt produced within the garnet zone is carried by many OIBs originating beneath thin lithosphere, indicative of a memory effect within plume-derived melts. This interpretation is further supported by geochemical trends from different samples generated in the same plume: it is therefore likely that some OIB melts, generated at varying pressures, can ascend to the surface separately without re-equilibrating at the base of the lithosphere.

Taken together, our results have implications for magma generation, migration and mixing beneath OIBs, which will be vital for connecting these intricate processes to the larger-scale dynamics of upwelling mantle plumes. Our study provides quantitative constraints on the relationship between modern OIB geochemistry and lithospheric thickness, which will underpin future efforts to invert the geochemical composition of volcanic lavas for the temperature and pressure of their mantle source (e.g., Klöcking et al., 2020; P. W. Ball et al., 2021), including those preserved from earlier periods of Earth's history, revealing changes in lithospheric thickness through space and time. Such point-wise constraints are also required by a new class of data-driven geodynamical simulation that aim to recover the spatial and temporal evolution of the mantle and its impact at the surface (e.g., Ghelichkhan et al., 2023; Bunge et al., 2023).

Open Research

The unfiltered dataset of geochemical analyses for OIBs was extracted from the open-source GeoRoc database (https://georoc.eu) in February, 2023. The dataset, which includes OIB geochemistry, lithospheric thickness, Python scripts for Bayes factor analysis and two-phase melting, and other information, is achieved at Zenodo (Jiang, 2024). Figures have been prepared using Matplotlib (Hunter, 2007).

Acknowledgments

This research was undertaken with the assistance of resources from the *National Computational Infrastructure* (NCI Australia), an NCRIS enabled capability supported by the Australian Government, and was partially supported by the Australian Government through the *Australian Research Council's* Discovery Projects funding scheme (project DP200100053) and Discovery Early Career Researcher Awards (DE220101519). The authors are also grateful for funding provided by the *Chinese Scholarship Council* (CSC) scholarship and *Shen-su Sun* scholarship. We thank Anthony Burnham, Thomas Duvernay, Hugh O'Neill and Fred Richards for help and feedback. We thank Boda Liu and Antonio Manjon-Cabeza Cordoba for constructive and valuable reviews.

References

Ahrens, L. H. (1952). The use of ionization potentials Part 1. Ionic radii of the elements. *Geochim. Cosmochim. Acta*, *2*(3), 155–169.

Albarède, F., Luais, B., Fitton, G., Semet, M., Kaminski, E., Upton, B. G. J., ... Cheminée, J.-L. (1997). The geochemical regimes of Piton de la Fournaise volcano (Réunion) during the last 530000 years. *J. Petrol.*, *38*(2), 171–201.

Asimow, P. D., & Langmuir, C. (2003). The importance of water to oceanic mantle melting regimes. *Nature*, *421*(6925), 815–820.

Ball, P., White, N., Maclennan, J., & Stephenson, S. (2021). Global influence of mantle temperature and plate thickness on intraplate volcanism. *Nature Communications*, *12*(1), 2045.

Ball, P. W., Czarnota, K., White, N. J., Klöcking, M., & Davies, D. R. (2021). Thermal structure of eastern Australia's upper mantle and its relationship to Cenozoic volcanic activity and dynamic topography. *Geochem. Geophys. Geosys.*, *22*(8), e2021GC009717.

Ball, P. W., Duvernay, T., & Davies, D. R. (2022). A coupled geochemical-geodynamic approach for predicting mantle melting in space and time. *Geochem. Geophys. Geosys.*, *23*(4), e2022GC010421.

Ball, P. W., White, N. J., Masoud, A., Nixon, S., Hoggard, M. J., Maclennan, J., ... Kröpelin, S. (2019). Quantifying asthenospheric and lithospheric controls on mafic magmatism across North Africa. *Geochem. Geophys. Geosys.*, *20*(7), 3520–3555.

Ballmer, M. D., Ito, G., van Hunen, J., & Tackley, P. J. (2011). Spatial and temporal variability in Hawaiian hotspot volcanism induced by small-scale convection. *Nat. Geosci.*, *4*(7), 457–460.

Bao, X., Lithgow-Bertelloni, C. R., Jackson, M. G., & Romanowicz, B. (2022). On the relative temperatures of Earth's volcanic hotspots and mid-ocean ridges. *Science*, *375*(6576), 57–61.

Bohlen, S. R., & Boettcher, A. L. (1981). Experimental investigations and geological applications of orthopyroxene geobarometry. *Am. Mineral.*, *66*(9-10), 951–964.

Bohlen, S. R., Essene, E. J., & Boettcher, A. L. (1980). Reinvestigation and application of olivine-quartz-orthopyroxene barometry. *Earth Planet. Sci. Lett.*, *47*(1), 1–10.

Borghini, G., Fumagalli, P., & Rampone, E. (2010). The stability of plagioclase in the upper mantle: subsolidus experiments on fertile and depleted lherzolite. *J. Petrol.*, *51*(1-2), 229–254.

Bunge, H.-P., Horbach, A., Colli, L., Ghelichkhan, S., Vilacís, B., & Hayek, J. N. (2023). Geodynamic data assimilation: Techniques and observables to construct and constrain time-dependent earth models. In A. Ismail-Zadeh, F. Castelli, D. Jones, & S. Sanchez (Eds.), *Applications of data assimilation and inverse problems in the earth sciences* (p. 311–325). Cambridge University Press. doi: 10.1017/9781009180412.021

Burov, E., & Gerya, T. (2014). Asymmetric three-dimensional topography over mantle plumes. *Nature*, *513*(7516), 85–89.

Burov, E., Guillou-Frottier, L., d'Acremont, E., Le Pourhiet, L., & Cloetingh, S. (2007). Plume head–lithosphere interactions near intra-continental plate boundaries. *Tectonophysics*, *434*(1-4), 15–38.

Campbell, I. H. (2007). Testing the plume theory. *Chem. Geol.*, *241*(3-4), 153–176.

Campbell, I. H., & Borley, G. D. (1974). The geochemistry of pyroxenes from the lower layered series of the Jimberlana intrusion, Western Australia. *Contri. Mineral. Petrol.*, *47*(4), 281–297.

Campbell, I. H., & Nolan, J. (1974). Factors effecting the stability field of Ca-poor pyroxene and the origin of the Ca-poor minimum in Ca-rich pyroxenes from tholeiitic intrusions. *Contrib. Mineral. and Petrol.*, *48*(3), 205–219.

Chung, S.-L., & Jahn, B.-M. (1995). Plume-lithosphere interaction in generation of the Emeishan flood basalts at the Permian-Triassic boundary. *Geology*, *23*(10), 889–892.

Class, C., & Goldstein, S. L. (1997). Plume-lithosphere interactions in the ocean basins: constraints from the source mineralogy. *Earth Planet. Sci. Lett.*, *150*(3-4), 245–260.

Colson, R. O., & Gust, D. A. (1989). Effects of pressure on partitioning of trace elements between low-Ca pyroxene and melt. *Am. Mineral.*, *74*(1-2), 31–36.

Condie, K. C. (1999). Mafic crustal xenoliths and the origin of the lower continental crust. *Lithos*, *46*(1), 95–101.

Conrad, C. P., Bianco, T. A., Smith, E. I., & Wessel, P. (2011). Patterns of intraplate volcanism controlled by asthenospheric shear. *Nature Geoscience*, *4*(5), 317–321.

Courtillot, V., Jaupart, C., Manighetti, I., Tapponnier, P., & Besse, J. (1999). On causal links between flood basalts and continental breakup. *Earth Planet. Sci. Lett.*, *166*(3-4), 177–195.

Danyushevsky, L. V., & Plechov, P. (2011). Petrolog3: Integrated software for modeling crystallization processes. *Geochem. Geophys. Geosys.*, *12*(7).

Dasgupta, R., Jackson, M. G., & Lee, C.-T. A. (2010). Major element chemistry of ocean island basalts—conditions of mantle melting and heterogeneity of mantle source. *Earth Planet. Sci. Lett.*, *289*(3-4), 377–392.

Davies, D. R., & Davies, J. H. (2009). Thermally-driven mantle plumes reconcile multiple hot-spot observations. *Earth Planet. Sci. Lett.*, *278*(1-2), 50–54.

Davies, D. R., Goes, S., & Sambridge, M. (2015). On the relationship between volcanic hotspot locations, the reconstructed eruption sites of large igneous provinces and deep mantle seismic structure. *Earth Planet. Sci. Lett.*, *411*, 121–130.

Davies, D. R., Le Voci, G., Goes, S., Kramer, S. C., & Wilson, C. R. (2016). The mantle wedge's transient 3-D flow regime and thermal structure. *Geochem. Geophys. Geosys.*, *17*(1), 78–100.

Davies, D. R., & Rawlinson, N. (2014). On the origin of recent intra-plate volcanism in Australia. *Geology*, *42*, 1031–1034. doi: 10.1016/j.epsl.2014.11.052

Davies, D. R., Rawlinson, N., Iaffaldano, G., & Campbell, I. H. (2015). Lithospheric controls on magma composition along Earth's longest continental hotspot track. *Nature*, *525*(7570), 511–514.

Davies, D. R., Valentine, A., Kramer, S. C., Rawlinson, N., Hoggard, M. J., Eakin, C., & Wilson, C. (2019). Earth's multi-scale topographic response to global mantle flow. *Nat. Geosci.*, *12*(10), 845–850.

Davies, G. F. (1994). Thermomechanical erosion of the lithosphere by mantle plumes. *J. Geophys. Res.*, *99*(B8), 15709–15722.

Davies, J. H. F. L., Marzoli, A., Bertrand, H., Youbi, N., Ernesto, M., Greber, N., . . . others (2021). Zircon petrochronology in large igneous provinces reveals upper crustal contamination processes: new U–Pb ages, Hf and O isotopes, and trace elements from the Central Atlantic magmatic province (CAMP). *Contrib. Mineral. Petrol.*, *176*, 1–24.

Dumoulin, C., Doin, M.-P., & Fleitout, L. (2001). Numerical simulations of the cooling of an oceanic lithosphere above a convective mantle. *Phys. Earth Planet. Inter.*, *125*(1-4), 45–64.

Duncan, R. A., & Richards, M. (1991). Hotspots, mantle plumes, flood basalts, and true polar wander. *Rev. Geophys.*, *29*(1), 31–50.

Duvernay, T., Davies, D. R., Mathews, C. R., Gibson, A. H., & Kramer, S. C. (2021). Linking intraplate volcanism to lithospheric structure and asthenospheric flow. *Geochem. Geophys. Geosys.*, *22*(8), e2021GC009953.

Duvernay, T., Davies, D. R., Mathews, C. R., Gibson, A. H., & Kramer, S. C. (2022). Continental magmatism: the surface manifestation of dynamic interactions between cratonic lithosphere, mantle plumes and edge-driven convection. *Geochem. Geophys. Geosys.*, *23*(7), e2022GC010363.

Ellam, R. (1992). Lithospheric thickness as a control on basalt geochemistry. *Geology*, *20*(2), 153–156.

Elliott, T., Hawkesworth, C., & Grönvold, K. (1991). Dynamic melting of the Iceland plume. *Nature*, *351*(6323), 201–206.

Fisk, M., Upton, B., Ford, C., & White, W. (1988). Geochemical and experimental study of the genesis of magmas of Reunion Island, Indian Ocean. *J. Geophys. Res.*, *93*(B5), 4933–4950.

Fitton, J. G., James, D., & Leeman, W. P. (1991). Basic magmatism associated with late Cenozoic extension in the western United States: Compositional variations in space and time. *J. Geophys. Res.*, *96*(B8), 13693–13711.

Fujimaki, H., Tatsumoto, M., & Ken-ichiro, A. (1984). Partition coefficients of Hf, Zr, and REE between phenocrysts and groundmasses. *J. Geophys. Res.*, *89*(S02), 662-672.

Gautier, I., Weis, D., Mennessier, J.-P., Vidal, P., Giret, A., & Loubet, M. (1990). Petrology and geochemistry of the Kerguelen Archipelago basalts (South Indian Ocean): evolution of the mantle sources from ridge to intraplate position. *Earth Planet. Sci. Lett.*, *100*(1-3), 59–76.

Ghelichkhan, S., Gibson, A., Davies, D. R., Kramer, S. C., & Ham, D. A. (2023). Automatic adjoint-based inversion schemes for geodynamics: Reconstructing the evolution of earth's mantle in space and time. *EGUsphere*, *2023*, 1–46.

Gibson, S., & Geist, D. (2010). Geochemical and geophysical estimates of lithospheric thickness variation beneath galápagos. *Earth Planet. Sci. Lett.*, *300*(3-4), 275–286.

Goslin, J., & Sibuet, J.-C. (1975). Geophysical study of the easternmost Walvis Ridge, South Atlantic: deep structure. *Geol. Soc. Am. Bull.*, *86*(12), 1713–1724.

Graça, M. C., Kusznir, N., & Stanton, N. S. G. (2019). Crustal thickness mapping of the central South Atlantic and the geodynamic development of the Rio Grande Rise and Walvis Ridge. *Mar. Pet. Geol.*, *101*, 230–242.

Green, D., & Ringwood, A. (1967). The genesis of basaltic magmas. *Contrib. Mineral. Petrol.*, *15*(2), 103–190.

Greenberger, R., Mustard, J., Kumar, P., Dyar, M., Breves, E., & Sklute, E. (2012). Low temperature aqueous alteration of basalt: Mineral assemblages of Deccan basalts and implications for Mars. *J. Geophys. Res.*, *117*(E11).

Grevemeyer, I., Flueh, E. R., Reichert, C., Bialas, J., Kläschen, D., & Kopp, C. (2001). Crustal architecture and deep structure of the Ninetyeast Ridge hotspot trail from active-source ocean bottom seismology. *Geophys. J. Int.*, *144*(2), 414–431.

Griffiths, R. W., & Campbell, I. H. (1990). Stirring and structure in mantle starting plumes. *Earth Planet. Sci. Lett.*, *99*(1-2), 66–78.

Griffiths, R. W., & Campbell, I. H. (1991). On the dynamics of long-lived plume conduits in the convecting mantle. *Earth Planet. Sci. Lett.*, *103*(1-4), 214–227.

Hart, S., Hauri, E., Oschmann, L., & Whitehead, J. (1992). Mantle plumes and entrainment: isotopic evidence. *Science*, *256*(5056), 517–520.

Herzberg, C. (1992). Depth and degree of melting of komatiites. *J. Geophys. Res.*, *97*(B4), 4521–4540.

Herzberg, C., Asimow, P. D., Arndt, N., Niu, Y., Lesher, C., Fitton, J., ... Saunders, A. (2007). Temperatures in ambient mantle and plumes: Constraints from basalts, picrites, and komatiites. *Geochem. Geophys. Geosys.*, *8*(2).

Hill, R. I. (1991). Starting plumes and continental break-up. *Earth Planet. Sci. Lett.*, *104*(2-4), 398–416.

Hofmann, A. (2003). Sampling mantle heterogeneity through oceanic basalts: isotopes and trace elements. *Treatise Geochem.*, *2*, 568.

Hofmann, A., & Jochum, K. (1996). Source characteristics derived from very incompatible trace elements in Mauna Loa and Mauna Kea basalts, Hawaii Scientific Drilling Project. *J. Geophys. Res.*, *101*(B5), 11831–11839.

Hoggard, M. J., Czarnota, K., Richards, F. D., Huston, D. L., Jaques, A. L., & Ghelichkhan, S. (2020). Global distribution of sediment-hosted metals controlled by craton edge stability. *Nat. Geosci.*, *13*(7), 504–510.

Hoggard, M. J., Parnell-Turner, R., & White, N. (2020). Hotspots and mantle plumes revisited: Towards reconciling the mantle heat transfer discrepancy. *Earth Planet. Sci. Lett.*, *542*, 116317.

Hole, M. J., & Millett, J. (2016). Controls of mantle potential temperature and lithospheric thickness on magmatism in the North Atlantic Igneous Province. *J. Petrol.*, *57*(2), 417–436.

Humphreys, E. R., & Niu, Y. (2009). On the composition of ocean island basalts (OIB): The effects of lithospheric thickness variation and mantle metasomatism. *Lithos*, *112*(1-2), 118-136.

Hunter, J. D. (2007). Matplotlib: A 2D graphics environment. *Computing in Science & Engineering*, *9*(3), 90–95. doi: 10.1109/MCSE.2007.55

Iaffaldano, G., Davies, D. R., & DeMets, C. (2018). Indian Ocean floor deformation induced by the Reunion plume rather than the Tibetan Plateau. *Nat. Geosci.*, *11*(5), 362–366.

Jackson, M. G., Weis, D., & Huang, S. (2012). Major element variations in Hawaiian shield lavas: Source features and perspectives from global ocean island basalt (OIB) systematics. *Geochem. Geophys. Geosys.*, *13*(9).

Jeffreys, H. (1935). Some tests of significance, treated by the theory of probability. In *Mathematical proceedings of the cambridge philosophical society* (Vol. 31, pp. 203–222).

Jiang, S. (2024, March). *Oib geochemistry & lithospheric thickness.* Zenodo. Retrieved from `https://doi.org/10.5281/zenodo.10889440` doi: 10.5281/zenodo.10889440

Johnson, K. T. M. (1994). Experimental cpx/ and garnet/melt partitioning of REE and other trace elements at high pressures: petrogenetic implications. *Mineral Mag.*, *58A*(1), 454-455.

Johnson, K. T. M. (1998). Experimental determination of partition coefficients for rare earth and high-field-strength elements between clinopyroxene, garnet, and basaltic melt at high pressures. *Contrib. Mineral. Petrol.*, *133*(1-2), 60-68. doi: DOI10.1007/s004100050437

Jones, T. D., Davies, D. R., Campbell, I. H., Iaffaldano, G., Yaxley, G. M., Kramer, S. C., & Wilson, C. R. (2017). The concurrent emergence and causes of double volcanic hotspot tracks on the pacific plate. *Nature*, *545*(7655), 472–476.

Jones, T. D., Davies, D. R., Campbell, I. H., Wilson, C. R., & Kramer, S. C. (2016). Do mantle plumes preserve the heterogeneous structure of their deep-mantle source? *Earth Planet. Sci. Lett.*, *434*, 10–17.

Jones, T. D., Davies, D. R., & Sossi, P. A. (2019). Tungsten isotopes in mantle plumes: Heads it's positive, tails it's negative. *Earth Planet. Sci. Lett.*, *506*, 255–267.

Kass, R. E., & Raftery, A. E. (1995). Bayes factors. *J. Am. Stat. Assoc.*, *90*(430), 773–795.

Katz, R. F., Spiegelman, M., & Langmuir, C. H. (2003). A new parameterization of hydrous mantle melting. *Geochem., Geophys., Geosys.*, *4*(9).

Khogenkumar, S., Singh, A. K., Singh, R. B., Khanna, P., Singh, N. I., & Singh, W. I. (2016). Coexistence of MORB and OIB-type mafic volcanics in the Manipur Ophiolite Complex, Indo-Myanmar Orogenic Belt, northeast India: implication for heterogeneous mantle source at the spreading zone. *J. Asian Earth Sci.*, *116*, 42–58.

King, S. D., & Anderson, D. L. (1998). Edge-driven convection. *Earth Planet. Sci. Lett.*, *1998*, 289–296. doi: 10.1016/S0012-821X(98)00089-2

Klemme, S., & O'Neill, H. S. (2000). The near-solidus transition from garnet lherzolite to spinel lherzolite. *Contri. Mineral. Petrol.*, *138*(3), 237–248.

Klöcking, M., Davies, D., Jaques, A. L., Champion, D. C., & Czarnota, K. (2020). *Spatio-temporal evolution of australian lithosphere-asthenosphere boundary from mafic volcanism.* Geoscience Australia.

Klöcking, M., White, N., Maclennan, J., McKenzie, D., & Fitton, J. (2018). Quantitative relationships between basalt geochemistry, shear wave velocity, and asthenospheric temperature beneath western North America. *Geochem. Geophys. Geosys.*, *19*(9), 3376–3404.

Le Voci, G., Davies, D. R., Goes, S., Kramer, S. C., & Wilson, C. R. (2014). A systematic 2-D investigation into the mantle wedge's transient flow regime and thermal structure: Complexities arising from a hydrated rheology and thermal buoyancy. *Geochem. Geophys. Geosys.*, *15*(1), 28–51.

Li, M., McNamara, A. K., & Garnero, E. J. (2014). Chemical complexity of hotspots caused by cycling oceanic crust through mantle reservoirs. *Nat. Geosci.*, *7*(5), 366–370.

Liu, J.-Q., Chen, L.-H., Zeng, G., Wang, X.-J., Zhong, Y., & Yu, X. (2016). Lithospheric thickness controlled compositional variations in potassic basalts of Northeast China by melt-rock interactions. *Geophys. Res. Lett.*, *43*(6), 2582–2589.

Lundstrom, C. C., Hoernle, K., & Gill, J. (2003). U-series disequilibria in volcanic rocks from the Canary Islands: Plume versus lithospheric melting. *Geochim. Cosmochim. Acta*, *67*(21), 4153–4177.

MacDonald, G. A., & Katsura, T. (1964). Chemical composition of Hawaiian lavas. *J. Petrol.*, *5*(1), 82–133.

Masaaki, O. (1980). The Ronda peridotite: Garnet-, spinel-, and plagioclase-lherzolite facies and the PT trajectories of a high-temprature mantle intrusion. *J. Petrol.*, *21*(3), 533–572.

Mather, B. R., Müller, R. D., Seton, M., Ruttor, S., Nebel, O., & Mortimer, N. (2020). Intraplate volcanism triggered by bursts in slab flux. *Science Advances*, *6*(51), eabd0953.

McKenzie, D. (1967). Some remarks on heat flow and gravity anomalies. *J. Geophys, Res.*, *72*(24), 6261–6273.

McKenzie, D., & O'Nions, R. K. (1991). Partial melt distributions from inversion of rare earth element concentrations. *J. Petrol.*, *32*(5), 1021-1091.

Morgan, W. J. (1971). Convection plumes in the lower mantle. *Nature*, *230*(5288), 42–43.

Nebel, O., Sossi, P. A., Bénard, A., Arculus, R. J., Yaxley, G. M., Woodhead, J. D., ... Ruttor, S. (2019). Reconciling petrological and isotopic mixing mechanisms in the Pitcairn mantle plume using stable Fe isotopes. *Earth Planet. Sci. Lett.*, *521*, 60–67.

Niu, Y. (2016). The meaning of global ocean ridge basalt major element compositions. *J. Petrol.*, *57*(11-12), 2081–2103.

Niu, Y. (2021). Lithosphere thickness controls the extent of mantle melting, depth of melt extraction and basalt compositions in all tectonic settings on Earth – A review and new perspectives. *Earth-Science Reviews*, *217*, 103614.

Niu, Y., Wilson, M., Humphreys, E. R., & O'Hara, M. J. (2011). The origin of intra-plate ocean island basalts (OIB): the lid effect and its geodynamic implications. *J. Petrol.*, *52*(7-8), 1443–1468.

Norman, M. D., & Garcia, M. O. (1999). Primitive magmas and source characteristics of the Hawaiian plume: petrology and geochemistry of shield picrites. *Earth Planet. Sci. Lett.*, *168*(1-2), 27–44.

Owen-Smith, T. M., Ashwal, L. D., Sudo, M., & Trumbull, R. B. (2017). Age and petrogenesis of the Doros Complex, Namibia, and implications for early plume-derived melts in the Paraná–Etendeka LIP. *J. Petrol.*, *58*(3), 423–442.

O'Neill, H. S. C. (2016). The smoothness and shapes of chondrite-normalized rare earth element patterns in basalts. *J. Petrol.*, *57*(8), 1463-1508.

Pallister, J. S., & Hopson, C. A. (1981). Samail ophiolite plutonic suite: field relations, phase variation, cryptic variation and layering, and a model of a spreading ridge magma chamber. *J. Geophys. Res.*, *86*(B4), 2593–2644.

Parsons, B., & Sclater, J. G. (1977). An analysis of the variation of ocean floor bathymetry and heat flow with age. *J. Geophys. Res.*, *82*(5), 803–827.

Pietruszka, A. J., Norman, M. D., Garcia, M. O., Marske, J. P., & Burns, D. H. (2013). Chemical heterogeneity in the hawaiian mantle plume from the alteration and dehydration of recycled oceanic crust. *Earth Planet. Sci. Lett.*, *361*, 298–309.

Priestley, K., & McKenzie, D. (2006). The thermal structure of the lithosphere from shear wave velocities. *Earth Planet. Sci. Lett.*, *244*(1-2), 285–301.

Putirka, K. (2008). Excess temperatures at ocean islands: Implications for mantle layering and convection. *Geology*, *36*(4), 283–286.

Rawlinson, N., Davies, D. R., & Pilia, S. (2017). The mechanisms underpinning Cenozoic intraplate volcanism in eastern Australia: Insights from seismic tomography and geodynamic modeling. *Geophysical Research Letters*, *44*(19), 9681–9690.

Richards, F. D., Hoggard, M. J., Cowton, L. R., & White, N. J. (2018). Reassessing the thermal structure of oceanic lithosphere with revised global inventories of basement depths and heat flow measurements. *J. Geophys. Res.*, *123*(10), 9136–9161.

Richards, F. D., Hoggard, M. J., Crosby, A., Ghelichkhan, S., & White, N. (2020). Structure and dynamics of the oceanic lithosphere-asthenosphere system. *Phys. Earth Planet. Inter.*, *309*, 106559.

Richards, F. D., Hoggard, M. J., White, N., & Ghelichkhan, S. (2020). Quantifying the relationship between short-wavelength dynamic topography and thermomechanical structure of the upper mantle using calibrated parameterization of anelasticity. *J. Geophys. Res.*, *125*(9), e2019JB019062.

Robinson, J. A. C., & Wood, B. J. (1998). The depth of the spinel to garnet transition at the peridotite solidus. *Earth Planet. Sci. Lett.*, *164*(1-2), 277–284.

Rudnick, R. L. (1995). Making continental crust. *Nature*, *378*(6557), 571–578.

Ryan, M. P. (1988). The mechanics and three-dimensional internal structure of active magmatic systems: Kilauea Volcano, Hawaii. *J. Geophys. Res.*, *93*(B5), 4213–4248.

Ryan, M. P. (1994). Neutral-buoyancy controlled magma transport and storage in mid-ocean ridge magma reservoirs and their sheeted-dike complex: a summary of basic relationships. *Int. Geophys.*, *57*, 97–138.

Safonov, O., Bindi, L., & Vinograd, V. (2011). Potassium-bearing clinopyroxene: a review of experimental, crystal chemical and thermodynamic data with petrological applications. *Mineral. Mag.*, *75*(4), 2467–2484.

Saito, T., Uno, M., Sato, T., Fujisaki, W., Haraguchi, S., Li, Y.-b., ... Maruyama, S. (2015). Geochemistry of accreted metavolcanic rocks from the Neoproterozoic Gwna Group of Anglesey–Lleyn, NW Wales, UK: MORB and OIB in the Iapetus Ocean. *Tectonophysics*, *662*, 243–255.

Scarrow, J. H., & Cox, K. (1995). Basalts generated by decompressive adiabatic melting of a mantle plume: a case study from the Isle of Skye, NW Scotland. *J. Petrol.*, *36*(1), 3–22.
Schaeffer, A., & Lebedev, S. (2013). Global shear speed structure of the upper mantle and transition zone. *Geophys. J. Int.*, *194*(1), 417–449.
Schmincke, H.-U. (1982). Volcanic and chemical evolution of the Canary Islands. In *Geology of the northwest african continental margin* (pp. 273–306). Springer.
Seton, M., Müller, R. D., Zahirovic, S., Williams, S., Wright, N. M., Cannon, J., ... McGirr, R. (2020). A global data set of present-day oceanic crustal age and seafloor spreading parameters. *Geochem. Geophys. Geosys.*, *21*(10), e2020GC009214.
Shaw, D. M. (1970). Trace element fractionation during anatexis. *Geochim. Cosmochim. Acta*, *34*(2), 237–243.
Shaw, D. M. (1979). Trace element melting models. *Phys. Chem. Earth*, *11*, 577–586.
Sisson, T., & Grove, T. (1993). Temperatures and H_2O contents of low-MgO high-alumina basalts. *Contrib. Mineral. Petrol.*, *113*(2), 167–184.
Skilling, J. (2006). Nested sampling for general bayesian computation. *Bayesian Anal.*, *1*(4), 833–860.
Speagle, J. S. (2020). DYNESTY: a dynamic nested sampling package for estimating Bayesian posteriors and evidences. *Mon. Notices Royal Astron. Soc.*, *493*(3), 3132–3158.
Straub, S. M., Gómez-Tuena, A., Zellmer, G. F., Espinasa-Perena, R., Stuart, F. M., Cai, Y., ... Mesko, G. T. (2013). The processes of melt differentiation in arc volcanic rocks: Insights from OIB-type arc magmas in the central Mexican volcanic belt. *J. Petrol.*, *54*(4), 665–701.
Sun, C., & Liang, Y. (2013). The importance of crystal chemistry on REE partitioning between mantle minerals (garnet, clinopyroxene, orthopyroxene, and olivine) and basaltic melts. *Chem. Geol.*, *358*, 23–36.
Tomlinson, E. L., & Holland, T. J. (2021). A thermodynamic model for the subsolidus evolution and melting of peridotite. *J. Petrol.*, *62*(1), 1–23.
Turcotte, D. L., & Oxburgh, E. R. (1967). Finite amplitude convective cells and continental drift. *J. Fluid Mech.*, *28*(1), 29–42. doi: 10.1017/S0022112067001880
Ubide, T., Larrea, P., Becerril, L., & Galé, C. (2022). Volcanic plumbing filters on ocean-island basalt geochemistry. *Geology*, *50*(1), 26–31.
van Hunen, J., Huang, J., & Zhong, S. (2003). The effect of shearing on the onset and vigor of small-scale convection in a Newtonian rheology. *Geophys. Res. Lett.*, *30*(19).
Wallace, P. J. (1998). Water and partial melting in mantle plumes: Inferences from the dissolved H_2O concentrations of Hawaiian basaltic magmas. *Geophys. Res. Lett.*, *25*(19), 3639–3642.
Walter, M. J., & Presnall, D. C. (1994). Melting behavior of simplified lherzolite in the system CaO-MgO-Al_2O_3-SiO_2-Na_2O from 7 to 35 kbar. *J. Petrol.*, *35*(2), 329–359.
Watson, S., & McKenzie, D. (1991). Melt generation by plumes: a study of Hawaiian volcanism. *J. Petrol.*, *32*(3), 501–537.
Weaver, B. L. (1991). The origin of ocean island basalt end-member compositions: trace element and isotopic constraints. *Earth Planet. Sci. Lett.*, *104*(2-4), 381–397.
White, R., & McKenzie, D. (1989). Magmatism at rift zones: the generation of volcanic continental margins and flood basalts. *J. Geophys. Res.*, *94*(B6), 7685–7729.
White, R., Minshull, T., Richardson, K., Smallwood, J., Staples, R., McBride, J., ... Group, F. W. (1996). Seismic images of crust beneath Iceland contribute to

long-standing debate. *Eos, Transactions American Geophysical Union*, *77*(21), 197–201.
Wood, B. J., Kiseeva, E. S., & Matzen, A. K. (2013). Garnet in the Earth's Mantle. *Elements*, *9*(6), 421–426.
Yoder Jr, H., & Tilley, C. E. (1962). Origin of basalt magmas: an experimental study of natural and synthetic rock systems. *J. Petrol.*, *3*(3), 342–532.

Supporting Information for "Investigating the Lid Effect in the Generation of Ocean Island Basalts"

S. Jiang[1], R. Hawkins[1], M.J. Hoggard[1], D.R. Davies[1], I.H. Campbell[1]

[1]Research School of Earth Sciences, Australian National University, Canberra, ACT 2601, Australia

Contents of this file

1. Figures S1 to S11: include information about lithospheric thickness from plate models, magma evolution processes from fractionation and reverse-fractionation calculations, model evidence calculation results and associated examples, and OIB temperatures from various geochemical constraints.

2. Tables S1 to S6: include information about lithospheric thickness evaluated from different models and λ_2 values from a two-phase melting model.

References

Abdel-Monem, A., Fernandez, L., & Boone, G. (1975). K-Ar ages from the eastern Azores group (Santa Maria, São Miguel and the Formigas islands). *Lithos*, *8*(4), 247–254.

Ariskin, A. A., Frenkel, M. Y., Barmina, G. S., & Nielsen, R. L. (1993). COMAGMAT: a Fortran program to model magma differentiation processes. *Computers & Geosciences*, *19*(8), 1155–1170.

Ball, P., White, N., Maclennan, J., & Stephenson, S. (2021). Global influence of mantle temperature and plate thickness on intraplate volcanism. *Nature Communications*, *12*(1), 2045.

Bao, X., Lithgow-Bertelloni, C. R., Jackson, M. G., & Romanowicz, B. (2022). On the relative temperatures of Earth's volcanic hotspots and mid-ocean ridges. *Science*, *375*(6576), 57–61.

Calvert, A. T., Moore, R. B., McGeehin, J. P., & da Silva, A. M. R. (2006). Volcanic history and $^{40}Ar/^{39}Ar$ and ^{14}C geochronology of Terceira Island, Azores, Portugal. *J. Volcanol. Geotherm. Res.*, *156*(1-2), 103–115.

Camps, P., Henry, B., Prevot, M., & Faynot, L. (2001). Geomagnetic paleosecular variation recorded in Plio-Pleistocene volcanic rocks from Possession Island (Crozet Archipelago, southern Indian Ocean). *J. Geophys. Res.*, *106*(B2), 1961–1971.

Caplan-Auerbach, J., Duennebier, F., & Ito, G. (2000). Origin of intraplate volcanoes from guyot heights and oceanic paleodepth. *J. Geophys. Res.*, *105*(B2), 2679–2697.

Caroff, M., Maury, R. C., Vidal, P., Guille, G., Dupuy, C., Cotten, J., … Gillot, P.-Y. (1995). Rapid temporal changes in ocean island basalt composition: Evidence from an 800 m deep drill hole in Eiao Shield (Marquesas). *J. Petrol.*, *36*(5), 1333–1365.

Carracedo, J. C., Day, S., Guillou, H., Badiola, E. R., Canas, J., & Torrado, F. P. (1998). Hotspot volcanism close to a passive continental margin: the Canary Islands. *Geol. Mag.*, *135*(5), 591–604.

Chaffey, D., Cliff, R., & Wilson, B. (1989). Characterization of the St Helena magma source. *Geol. Soc. Spec. Publ.*, *42*(1), 257–276.

Clague, D. A., Dalrymple, G. B., Wright, T., Klein, F., Koyanagi, R., Decker, R., & Thomas, D. (1989). The Hawaiian-Emperor chain. In *The Eastern Pacific Ocean and Hawaii.*

Clague, D. A., Weber, W. S., & Dixon, J. E. (1991). Picritic glasses from Hawaii. *Nature*, *353*(6344), 553–556.

Cliff, R., Baker, P., & Mateer, N. (1991). Geochemistry of inaccessible island volcanics. *Chem. Geol.*, *92*(4), 251–260.

Clouard, V., & Bonneville, A. (2005). Ages of seamounts, islands, and plateaus on the Pacific plate. *Geol. Soc. Am. Spec. Pap.*, *388*, 71.

Cousens, B. L., & Clague, D. A. (2015). Shield to rejuvenated stage volcanism on Kauai and Niihau, Hawaiian Islands. *J. Petrol.*, *56*(8), 1547–1584.

Danyushevsky, L. V., & Plechov, P. (2011). Petrolog3: Integrated software for modeling crystallization processes. *Geochem. Geophys. Geosys.*, *12*(7).

Duncan, R., & Varne, R. (1988). The age and distribution of the igneous rocks of Macquarie Island. In *Papers and proceedings of the royal society of tasmania* (Vol. 122, pp. 45–50).

Duncan, R. A. (2002). A time frame for construction of the Kerguelen Plateau and

Broken Ridge. *J. Petrol.*, *43*(7), 1109–1119.

Duncan, R. A., & McDougall, I. (1974). Migration of volcanism with time in the Marquesas Islands, French Polynesia. *Earth Planet. Sci. Lett.*, *21*(4), 414–420.

Duncan, R. A., & McDougall, I. (1976). Linear volcanism in French polynesia. *J. Volcanol. Geotherm. Res.*, *1*(3), 197–227.

Dyhr, C. T., & Holm, P. M. (2010). A volcanological and geochemical investigation of Boa Vista, Cape Verde Islands: 40Ar/39Ar geochronology and field constraints. *J. Volcanol. Geotherm. Res.*, *189*(1-2), 19–32.

Esser, R. P., Kyle, P. R., & McIntosh, W. C. (2004). ^{40}Ar/^{39}Ar dating of the eruptive history of Mount Erebus, Antarctica: volcano evolution. *Bull. Volcanol.*, *66*, 671–686.

Fodor, R., Frey, F., Bauer, G., & Clague, D. (1992). Ages, rare-earth element enrichment, and petrogenesis of tholeiitic and alkalic basalts from Kahoolawe Island, Hawaii. *Contrib. Mineral. Petrol.*, *110*, 442–462.

França, Z. T., Tassinari, C. C., Cruz, J. V., Aparicio, A. Y., Araña, V., & Rodrigues, B. N. (2006). Petrology, geochemistry and Sr–Nd–Pb isotopes of the volcanic rocks from Pico Island—Azores (Portugal). *J. Volcanol. Geotherm. Res.*, *156*(1-2), 71–89.

Geist, D. J., Snell, H., Snell, H., Goddard, C., & Kurz, M. D. (2014). A paleogeographic model of the Galápagos Islands and biogeographical and evolutionary implications. *The Galápagos: a natural laboratory for the earth sciences*, 145–166.

Haase, K., Devey, C. W., Mertz, D. F., Stoffers, P., & Garbe-Schönberg, D. (1996). Geochemistry of lavas from Mohns Ridge, Norwegian-Greenland Sea: implications for melting conditions and magma sources near Jan Mayen. *Contrib. Mineral. Petrol.*, *123*(3), 223–237.

Hajash, A., & Armstrong, R. L. (1972). Paleomagnetic and radiometric evidence for the age of the Comores Islands, west central Indian Ocean. *Earth Planet. Sci. Lett.*, *16*(2), 231–236.

Harris, C., Bell, J., & Atkins, F. (1983). Isotopic composition of lead and strontium in lavas and coarse-grained blocks from Ascension Island, South Atlantic—an addendum. *Earth Planet. Sci. Lett.*, *63*(1), 139–141.

Hildenbrand, A., Marques, F. O., Costa, A., Sibrant, A., Silva, P., Henry, B., … Madureira, P. (2012). Reconstructing the architectural evolution of volcanic islands from combined K/Ar, morphologic, tectonic, and magnetic data: The Faial Island example (Azores). *J. Volcanol. Geotherm. Res.*, *241*, 39–48.

Holm, P. M., Grandvuinet, T., Friis, J., Wilson, J. R., Barker, A. K., & Plesner, S. (2008). An ^{40}Ar-^{39}Ar study of the Cape Verde hot spot: Temporal evolution in a semistationary plate environment. *J. Geophys. Res.*, *113*(B8).

Johnson, C. L., Wijbrans, J. R., Constable, C. G., Gee, J., Staudigel, H., Tauxe, L., … Salgueiro, M. (1998). ^{40}Ar/^{39}Ar ages and paleomagnetism of Sao Miguel lavas, Azores. *Earth Planet. Sci. Lett.*, *160*(3-4), 637–649.

Klemme, S., & O'Neill, H. S. (2000). The near-solidus transition from garnet lherzolite to spinel lherzolite. *Contri. Mineral. Petrol.*, *138*(3), 237–248.

Leonhardt, R., McWilliams, M., Heider, F., & Soffel, H. (2009). The Gilsá excursion and the Matuyama/Brunhes transition recorded in ^{40}Ar/^{39}Ar dated lavas from Lanai and Maui, Hawaiian Islands. *Geophysical Journal International*, *179*(1), 43–58.

McKenzie, D., & O'Nions, R. K. (1995). The source regions of ocean island basalts. *J.*

Petrol., *36*(1), 133–159.

Millet, M.-A., Doucelance, R., Baker, J. A., & Schiano, P. (2009). Reconsidering the origins of isotopic variations in Ocean Island Basalts: insights from fine-scale study of São Jorge Island, Azores archipelago. *Chem. Geol.*, *265*(3-4), 289–302.

Natland, J. H., & Turner, D. L. (1985). Age progression and petrological development of Samoan shield volcanoes: evidence from K-Ar ages, lava compositions, and mineral studies. *Investigations of the Northern Melanesian Border-land, Earth Sci. Ser.*, *3*.

O'Connor, J. M., & le Roex, A. P. (1992). South Atlantic hot spot-plume systems: 1. Distribution of volcanism in time and space. *Earth Planet. Sci. Lett.*, *113*(3), 343–364.

O'Connor, J. M., & Jokat, W. (2015). Tracking the Tristan-Gough mantle plume using discrete chains of intraplate volcanic centers buried in the Walvis Ridge. *Geology*, *43*(8), 715–718.

Paul, D., White, W. M., & Blichert-Toft, J. (2005). Geochemistry of Mauritius and the origin of rejuvenescent volcanism on oceanic island volcanoes. *Geochem. Geophys. Geosys.*, *6*(6).

Putirka, K. (2008). Excess temperatures at ocean islands: Implications for mantle layering and convection. *Geology*, *36*(4), 283–286.

Recq, M., Goslin, J., Charvis, P., & Operto, S. (1998). Small-scale crustal variability within an intraplate structure: the Crozet Bank (southern Indian Ocean). *Geophys. J. Int.*, *134*(1), 145–156.

Richards, F. D., Hoggard, M. J., Crosby, A., Ghelichkhan, S., & White, N. (2020). Structure and dynamics of the oceanic lithosphere-asthenosphere system. *Phys. Earth*

Planet. Inter., *309*, 106559.

Robinson, J. A. C., & Wood, B. J. (1998). The depth of the spinel to garnet transition at the peridotite solidus. *Earth Planet. Sci. Lett.*, *164*(1-2), 277–284.

Schwarz, S., Klügel, A., & Wohlgemuth-Ueberwasser, C. (2004). Melt extraction pathways and stagnation depths beneath the Madeira and Desertas rift zones (NE Atlantic) inferred from barometric studies. *Contrib. Mineral. Petrol.*, *147*, 228–240.

Seton, M., Müller, R. D., Zahirovic, S., Williams, S., Wright, N. M., Cannon, J., ... McGirr, R. (2020). A global data set of present-day oceanic crustal age and seafloor spreading parameters. *Geochem. Geophys. Geosys.*, *21*(10), e2020GC009214.

Stuessy, T. F., Foland, K., Sutter, J. F., Sanders, R. W., & Silva O, M. (1984). Botanical and geological significance of potassium-argon dates from the Juan Fernandez Islands. *Science*, *225*(4657), 49–51.

Tomlinson, E. L., & Holland, T. J. (2021). A thermodynamic model for the subsolidus evolution and melting of peridotite. *J. Petrol.*, *62*(1), 1–23.

Upton, B. J., Wadsworth, W., & Newman, T. (1967). The petrology of rodriguez island, indian ocean. *Geological Society of America Bulletin*, *78*(12), 1495–1506.

Vezzoli, L., & Acocella, V. (2009). Easter Island, SE Pacific: An end-member type of hotspot volcanism. *Geol. Soc. Am. Bull.*, *121*(5-6), 869–886.

Weis, D., Frey, F. A., Schlich, R., Schaming, M., Montigny, R., Damasceno, D., ... Scoates, J. S. (2002). Trace of the Kerguelen mantle plume: Evidence from seamounts between the Kerguelen Archipelago and Heard Island, Indian Ocean. *Geochem. Geophys. Geosys.*, *3*(6), 1–27.

Workman, R. K., & Hart, S. R. (2005). Major and trace element composition of the depleted MORB mantle (DMM). *Earth Planet. Sci. Lett.*, *231*(1-2), 53–72.

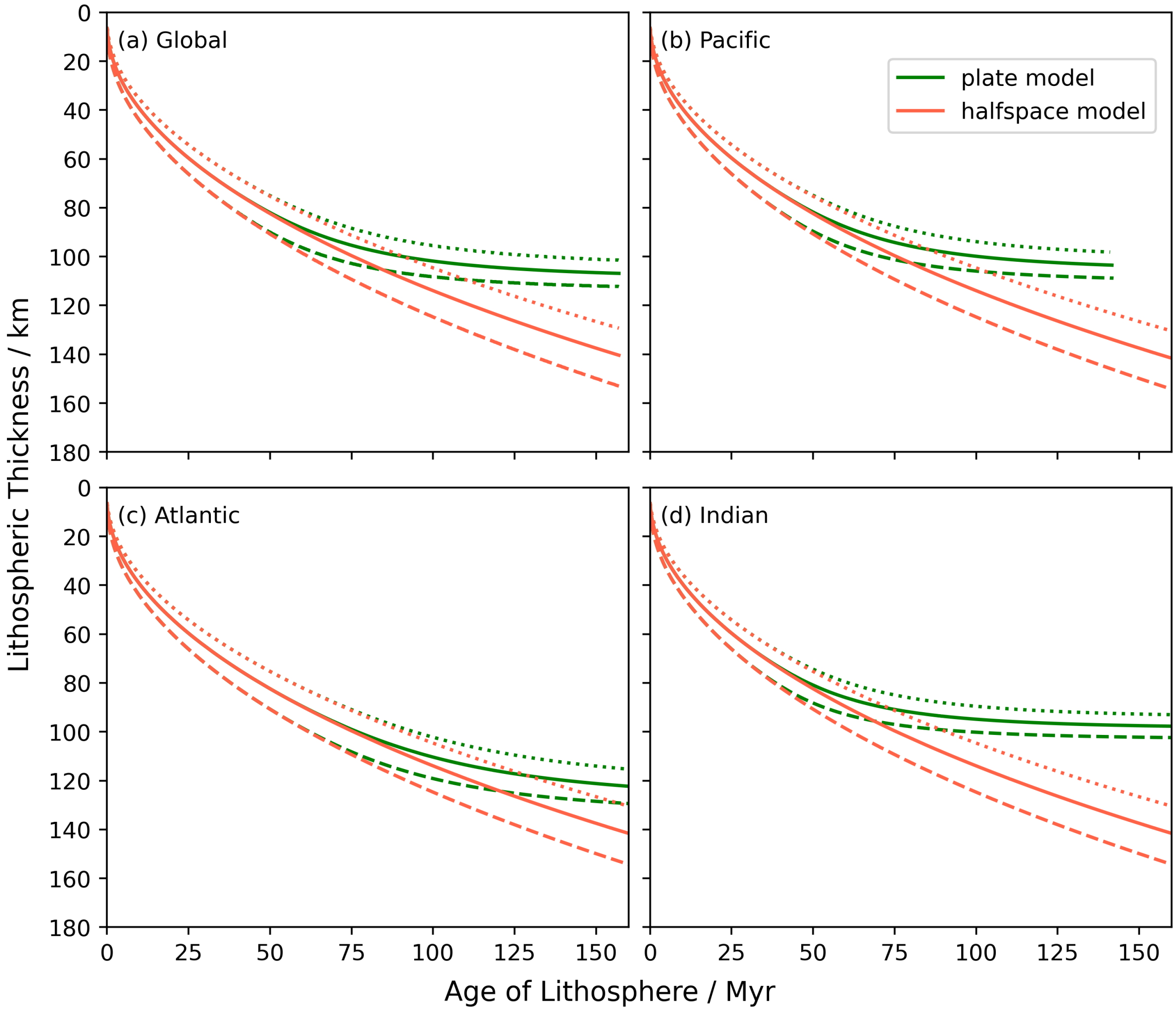

Figure S1. The world average and each oceanic basin's lithospheric thickness as a function of time for the best-fitting RHCGW20 plate model and half-space model (Richards et al., 2020). The halfspace model is coloured red, whereas the plate model is coloured green. The 1125 °C, 1175 °C, and 1225 °C contours are represented by the dotted, solid, and dashed lines, respectively.

Table S1. Locations of OIB samples selected from Atlantic and Indian Ocean for this study. In brackets is the name of the island chain/group to which each island belongs. The age of the lithosphere at present day and the misfit are obtained from Seton et al. (2020). The minimun and maximun eruption ages are obtained from multiple papers.

Island	Longitude	Latitude	Ocean	Lithospheric Age at Present Day (Myr)	Present-day Age Misfit (Myr)	Eruption Age Max (Myr)	Eruption Age Min (Myr)	Reference
Ascension	−14.3559	−7.9467	Atlantic	5.07	0.98	1.7	1.3	1, 2
Boa Vista (Cape Verde)	−22.8078	16.0950	Atlantic	140.78	0.67	15	4.5	3
Brava (Cape Verde)	−24.7024	14.8444	Atlantic	7.99	0.75	2	0	4
Corvo (Azores)	−31.1080	39.7023	Atlantic	10.00	0.23	1.5	1	5
Deserta	−16.5290	32.5594	Atlantic	140.99	0.24	3.6	1.7	6
Faial (Azores)	−28.6965	38.5913	Atlantic	13.52	2.00	0.85	0.03	7
Fogo (Cape Verde)	−24.3817	14.9133	Atlantic	128.52	0.63	3	0	4
Fuerteventura (Canary)	−14.0537	28.3587	Atlantic	188.36	3.77	20.6	12.5	8
Gough	−9.9353	−40.3189	Atlantic	29.70	0.37	1	0	9, 10
Gran Canaria (Canary)	−15.5474	27.9202	Atlantic	176.60	2.75	14.5	9.5	8
Inaccessible	−12.6733	−37.3004	Atlantic	20.25	0.27	6	1	11
Jan Mayen	−8.2920	71.0318	Atlantic	9.85	2.40	7	7	12
La Gomera (Canary)	−17.2194	28.1033	Atlantic	160.82	1.07	12	2.6	8
La Palma (Canary)	−17.9058	28.7134	Atlantic	154.05	0.42	2	0.1	8
Lanzarote (Canary)	−13.5900	29.0469	Atlantic	188.61	3.87	15.5	0	8
Maio (Cape Verde)	−23.1680	15.2003	Atlantic	137.97	0.21	16	6	4
Pico (Azores)	−28.3228	38.4580	Atlantic	16.05	2.40	0.3	0	5
Sal (Cape Verde)	−22.9297	16.7266	Atlantic	140.09	0.81	15	1.1	4
Santiago (Cape Verde)	−23.6205	15.0853	Atlantic	135.06	0.31	4.6	0.7	4
Sao Jorge (Azores)	−28.0303	38.6410	Atlantic	16.72	1.95	1.3	0.2	13
Sao Miguel (Azores)	−25.4970	37.7804	Atlantic	38.03	1.74	4	0.95	14, 15
St. Helena	−5.7089	−15.9650	Atlantic	40.47	1.04	9	7	16
Terceira (Azores)	−27.2206	38.7216	Atlantic	19.35	1.45	0.38	0.04	17
Tenerife (Canary)	−16.8330	28.29	Atlantic	163.66	1.33	12	7.5	8
Tristan da Cunha	−12.2777	−37.1052	Atlantic	21.66	0.27	0.21	0	9
Comoros	43.3333	−11.6455	Indian	141.23	3.14	3.65	0.01	18
Heard	73.5042	−53.0818	Indian	112.66	3.47	21	18	19
Ile aux Cochons (Crozet)	50.2315	−46.0988	Indian	72.99	0.58	0.4	0.2	20
Ile de l'Est (Crozet)	52.2197	−46.4359	Indian	70.06	0.41	8.75	2.9	20
Ile de la Possession (Crozet)	51.7378	−46.4269	Indian	70.48	0.37	5	0.5	20
Ile des Pingouins (Crozet)	50.4088	−46.4187	Indian	71.77	0.51	1.1	1.1	20, 21
Kerguelen	69.3545	−49.3948	Indian	64.84	2.67	34	0.1	20
Mauritius (Mascarene)	57.5522	−20.3484	Indian	66.13	4.05	7.8	1.9	22
Renuion (Mascarene)	55.5364	−21.1151	Indian	69.82	1.64	2.2	2	23
Rodrigues (Mascarene)	63.4272	−19.7245	Indian	13.23	0.39	1.5	1.5	24

Table S2. As in Table. S1 but for islands on Pacific Ocean.

Island	Longitude	Latitude	Ocean	Lithospheric Age at Present Day (Myr)	Present-day Age Misfit (Myr)	Eruption Age Max (Myr)	Eruption Age Min (Myr)	Reference
Aitutaki (Cook-Austral)	−159.7853	−18.858	Pacific	107.18	3.10	8.4	1	25, 26
Alexander Selkirk (Juan Fernandez)	−80.787	−33.761	Pacific	29.07	0.33	2.58	0.89	27
Bara Bora (Society)	−151.7415	−16.5004	Pacific	80.46	1.00	3.39	3.12	25
Darwin (Galapagos)	−92.0041	1.6787	Pacific	2.66	0.24	2	0.4	28
Easter	−109.3497	−27.1127	Pacific	6.33	1.78	0.78	0.11	29
Eiao (Marquesas)	−140.6690	−7.9790	Pacific	54.28	0.18	5.6	5.4	25, 31
Espanole (Galapagos)	−89.6722	−1.3758	Pacific	14.83	0.46	3.5	3	28
Fangataufa (Pitcairn)	−138.7427	−22.2353	Pacific	35.39	1.18	10.62	9.64	25
Fatu Hiva (Marquesas)	−138.6489	−10.4905	Pacific	50.14	0.48	1.39	1.3	25, 30
Fernandina (Galapagos)	−91.4821	−0.4124	Pacific	12.50	0.15	0.06	0.032	28
Floreana (Galapagos)	−90.4313	−1.3083	Pacific	14.64	0.28	2.3	1.5	28
Gambier (Pitcairn)	−134.9743	−23.1097	Pacific	29.48	0.37	5.63	5.16	25
Hawaii Main Island	−155.6659	19.5429	Pacific	92.92	1.96	1	0	25
Hiva Oa (Marquesas)	−139.0211	−9.7547	Pacific	50.67	0.25	2.48	1.58	25, 30
Huahine (Society)	−150.9889	−16.7883	Pacific	77.33	0.81	2.58	2.01	25
Isabela (Galapagos)	−91.1353	−0.8292	Pacific	13.51	0.15	0.8	0.5	28
Kahoolawe (Hawaii)	−156.5961	20.5552	Pacific	94.17	1.28	1.42	0.99	32
Kauai (Hawaii)	−159.5261	22.0964	Pacific	89.17	2.28	5.8	4.3	33
Lanai (Hawaii)	−156.9273	20.8166	Pacific	94.62	1.27	1.6	1.55	34
Macquarie	158.8556	−54.6208	Pacific	20.02	0.00	11.5	9.7	35
Mangaia (Cook-Austral)	−157.9166	−21.9352	Pacific	100.70	1.62	18.9	16.6	25, 26
Marchena (Galapagos)	−90.4691	0.3184	Pacific	9.71	0.66	0.8	0.6	28
Maui (Hawaii)	−156.3319	20.7984	Pacific	93.61	1.09	1.3	1.15	36
Maupiti (Society)	−152.2620	−16.4382	Pacific	82.88	1.03	4.49	3.94	25
Mehetia (Society)	−148.0669	−17.8775	Pacific	66.30	0.37	0.55	0.2	25
Molokai (Hawaii)	−157.0226	21.1444	Pacific	91.36	1.47	1.8	1.3	25
Nihoa (Hawaii)	−161.9218	23.0605	Pacific	92.20	3.64	7.5	6.9	25
Niihau (Hawaii)	−160.1575	21.8921	Pacific	90.37	2.92	5.6	5.4	33
Nuku Hiva (Marquesas)	−140.1421	−8.8605	Pacific	53.39	0.20	4.22	3.7	25, 30
Oahu (Hawaii)	−158.0001	21.4389	Pacific	89.16	1.45	3.6	2.8	25
Pinta (Galapagos)	−90.7628	0.5920	Pacific	7.94	0.43	0.8	0.7	28
Pitcairn	−128.3242	−24.3768	Pacific	20.02	1.45	0.93	0.45	25
Raivavae (Cook-Austral)	−147.6609	−23.8650	Pacific	62.28	2.46	7	4.8	25, 26
Rapa (Cook-Austral)	−144.3313	−27.5811	Pacific	54.75	0.31	4.6	4	25, 26
Rarotonga (Cook-Austral)	−159.7763	−21.2292	Pacific	102.65	2.95	1.8	1.2	25, 26
Rimatara (Cook-Austral)	−152.7500	−22.6690	Pacific	84.87	1.39	2.6	1	25, 26
Robinson Crusoe (Juan Fernandez)	−78.8580	−33.6377	Pacific	30.47	1.13	4.39	4.07	27
Ross	166.9603	−77.5247	Pacific	48.00	0.00	4	0.3	37
Rurutu (Cook-Austral)	−151.3385	−22.4801	Pacific	83.76	1.57	12	8.4	25, 26
San Cristobal (Galapagos)	−89.4364	−0.8675	Pacific	13.12	1.04	4	2.4	28
Santa Cruz (Galapagos)	−90.3372	−0.6394	Pacific	12.96	0.23	1.1	0.03	28
Savaii (Samoan)	−172.4319	−13.6598	Pacific	114.15	2.78	5	3	25
Tahiti (Society)	−149.426	−17.6509	Pacific	71.47	0.49	1.23	0.48	25
Tubuai (Cook-Austral)	−149.4500	−23.3788	Pacific	77.91	2.02	10.4	8.6	25, 26
Tutuila (Samoan)	−170.7325	−14.3258	Pacific	113.82	3.74	1.4	1	25, 38
Ua Huka (Marquesas)	−139.5484	−8.9078	Pacific	51.62	0.20	2.78	2.75	25, 30
Ua Pou (Marquesas)	−140.0804	−9.4043	Pacific	53.59	0.18	2.95	2.95	25
Upolu (Samoan)	−171.7349	−13.9134	Pacific	114.09	3.16	2.7	1.5	25, 38

Table S3. References for oceanic island ages from Table. S1 and S2.

Number	Reference
1	Caplan-Auerbach, Duennebier, and Ito (2000)
2	Harris, Bell, and Atkins (1983)
3	Dyhr and Holm (2010)
4	Holm et al. (2008)
5	França et al. (2006)
6	Schwarz, Klügel, and Wohlgemuth-Ueberwasser (2004)
7	Hildenbrand et al. (2012)
8	Carracedo et al. (1998)
9	O'Connor and le Roex (1992)
10	O'Connor and Jokat (2015)
11	Cliff, Baker, and Mateer (1991)
12	Haase, Devey, Mertz, Stoffers, and Garbe-Schönberg (1996)
13	Millet, Doucelance, Baker, and Schiano (2009)
14	Abdel-Monem, Fernandez, and Boone (1975)
15	Johnson et al. (1998)
16	Chaffey, Cliff, and Wilson (1989)
17	Calvert, Moore, McGeehin, and da Silva (2006)
18	Hajash and Armstrong (1972)
19	Weis et al. (2002)
20	Recq, Goslin, Charvis, and Operto (1998)
21	Camps, Henry, Prevot, and Faynot (2001)
22	R. A. Duncan (2002)
23	Paul, White, and Blichert-Toft (2005)
24	Upton, Wadsworth, and Newman (1967)
25	Clouard and Bonneville (2005)
26	R. A. Duncan and McDougall (1976)
27	Stuessy, Foland, Sutter, Sanders, and Silva O (1984)
28	Geist, Snell, Snell, Goddard, and Kurz (2014)
29	Vezzoli and Acocella (2009)
30	R. A. Duncan and McDougall (1974)
31	Caroff et al. (1995)
32	Fodor, Frey, Bauer, and Clague (1992)
33	Cousens and Clague (2015)
34	Leonhardt, McWilliams, Heider, and Soffel (2009)
35	R. Duncan and Varne (1988)
36	Clague et al. (1989)
37	Esser, Kyle, and McIntosh (2004)
38	Natland and Turner (1985)

Table S4. Mean lithospheric thickness estimates at the time of eruption for off-axis oceanic islands in the Atlantic and Indian Ocean.

Island	Ocean	Global Plate Model	Basin-based Plate Model	Seismology	Seismolgy Corrected
Ascension	Atlantic	25.92	26.05	55.98	54.18
Boa Vista (Cape Verde)	Atlantic	105.52	118.29	82.96	75.01
Brava (Cape Verde)	Atlantic	34.32	34.2	86.21	84.79
Corvo (Azores)	Atlantic	37.79	37.85	50.96	49.29
Deserta	Atlantic	105.86	119.75	92.85	89.46
Faial (Azores)	Atlantic	45.03	44.89	50.37	49.79
Fogo (Cape Verde)	Atlantic	104.97	117.68	87.31	85.46
Fuerteventura (Canary)	Atlantic	112.94	123.32	93.49	81.21
Gough	Atlantic	64.56	64.59	80.94	80.27
Gran Canaria (Canary)	Atlantic	109.93	122.58	90.67	81.53
Inaccessible	Atlantic	50.21	50.11	47.36	42.11
Jan Mayen	Atlantic	23.23	23.14	57.15	48.36
La Gomera (Canary)	Atlantic	106.73	121.62	86.04	80.17
La Palma (Canary)	Atlantic	106.71	121.59	85.26	83.92
Lanzarote (Canary)	Atlantic	116.49	124.12	93.56	87.12
Maio (Cape Verde)	Atlantic	105.16	117.83	86.29	77.55
Pico (Azores)	Atlantic	49.12	48.94	53.35	53.16
Sal (Cape Verde)	Atlantic	105.48	118.76	80.76	74
Santiago (Cape Verde)	Atlantic	105.57	118.56	85.45	83
Sao Jorge (Azores)	Atlantic	49.16	49.01	51.65	50.67
Sao Miguel (Azores)	Atlantic	70.77	70.98	68.28	65.87
St. Helena	Atlantic	67.92	67.82	81.68	75.1
Terceira (Azores)	Atlantic	53.3	53.12	57.57	57.32
Tenerife (Canary)	Atlantic	106.79	121.78	87.38	79.77
Tristan da Cunha	Atlantic	56.26	56.22	48.22	48.08
Comoros	Indian	106.04	97.25	87.73	85.61
Heard	Indian	100.51	94.1	99.31	85.4
Ile aux Cochons (Crozet)	Indian	94.78	90.24	67.32	67.02
Ile de l'Est (Crozet)	Indian	91.01	87.62	72.1	66.64
Ile de la Possession (Crozet)	Indian	92.73	89.11	70.6	68.05
Ile des Pingouins (Crozet)	Indian	93.65	90.02	67.32	66.25
Kerguelen	Indian	80.93	79.26	71.7	52.45
Mauritius (Mascarene)	Indian	89.54	86.81	76.76	72.57
Renuion (Mascarene)	Indian	92.69	88.88	84.59	82.57
Rodrigues (Mascarene)	Indian	42.77	42.89	59.93	58.26

Table S5. Mean lithospheric thickness estimates at the time of eruption for off-axis oceanic islands in the Pacific Ocean.

Island	Ocean	Global Plate Model	Basin-based Plate Model	Seismology	Seismolgy Corrected
Aitutaki (Cook-Austral)	Pacific	102.41	100.17	84.37	80.46
Alexander Selkirk (Juan Fernandez)	Pacific	62.68	62.54	63.91	62.1
Bara Bora (Society)	Pacific	96.4	95.13	73.34	70.41
Darwin (Galapagos)	Pacific	18.26	18.17	42.86	40.91
Easter	Pacific	31.98	32.06	44.91	44.24
Eiao (Marquesas)	Pacific	81.8	81.55	79.35	74.71
Espanole (Galapagos)	Pacific	42.67	42.5	46.28	41.28
Fangataufa (Pitcairn)	Pacific	60.39	60.5	80.94	72.44
Fatu Hiva (Marquesas)	Pacific	81.59	81.48	68	66.7
Fernandina (Galapagos)	Pacific	43.92	43.99	44.67	44.6
Floreana (Galapagos)	Pacific	44.46	44.48	46.72	43.91
Gambier (Pitcairn)	Pacific	59.28	59.4	85.15	80.74
Hawaii Main Island	Pacific	100.51	98.53	81.38	80.69
Hiva Oa (Marquesas)	Pacific	81.53	81.3	70.38	68.49
Huahine (Society)	Pacific	95.52	94.36	73.77	71.71
Isabela (Galapagos)	Pacific	44.56	44.52	45.56	44.59
Kahoolawe (Hawaii)	Pacific	100.47	98.7	73.91	72.81
Kauai (Hawaii)	Pacific	98.63	96.96	81.5	77.31
Lanai (Hawaii)	Pacific	100.71	98.81	73.91	72.49
Macquarie	Pacific	38.85	38.95	76.44	66.89
Mangaia (Cook-Austral)	Pacific	98.23	96.53	83.35	68.31
Marchena (Galapagos)	Pacific	38.22	38.29	43.46	42.36
Maui (Hawaii)	Pacific	100.26	98.59	73.93	72.82
Maupiti (Society)	Pacific	96.85	95.54	74.45	70.69
Mehetia (Society)	Pacific	91.91	90.99	75.94	75.55
Molokai (Hawaii)	Pacific	99.95	98.17	74.25	72.86
Nihoa (Hawaii)	Pacific	98.54	97.11	81.62	75.69
Niihau (Hawaii)	Pacific	98.66	97.26	84.98	80.48
Nuku Hiva (Marquesas)	Pacific	82.41	82	74.98	71.47
Oahu (Hawaii)	Pacific	98.9	97.34	80.66	77.94
Pinta (Galapagos)	Pacific	34.75	34.71	43.19	42
Pitcairn	Pacific	53.36	53.62	54.35	53.5
Raivavae (Cook-Austral)	Pacific	86.64	86.27	73.62	68.23
Rapa (Cook-Austral)	Pacific	82.81	82.59	68.14	63.91
Rarotonga (Cook-Austral)	Pacific	102.13	100.09	84.42	82.83
Rimatara (Cook-Austral)	Pacific	98.3	96.74	71.62	69.96
Robinson Crusoe (Juan Fernandez)	Pacific	61.59	61.59	64.11	59.64
Ross	Pacific	79.49	79.24	59.08	56.62
Rurutu (Cook-Austral)	Pacific	94.89	94.09	72.2	62.33
San Cristobal (Galapagos)	Pacific	39.81	39.9	44.73	39.61
Santa Cruz (Galapagos)	Pacific	43.86	43.88	45.38	44.52
Savaii (Samoan)	Pacific	103.4	101.19	71.48	67.74
Tahiti (Society)	Pacific	93.77	92.91	74.35	73.56
Tubuai (Cook-Austral)	Pacific	92.91	92.17	73.24	64.29
Tutuila (Samoan)	Pacific	103.73	101.52	81.67	80.46
Ua Huka (Marquesas)	Pacific	81.83	81.6	73.76	71.28
Ua Pou (Marquesas)	Pacific	82.92	82.84	74.4	71.77
Upolu (Samoan)	Pacific	103.61	101.32	73.65	71.77

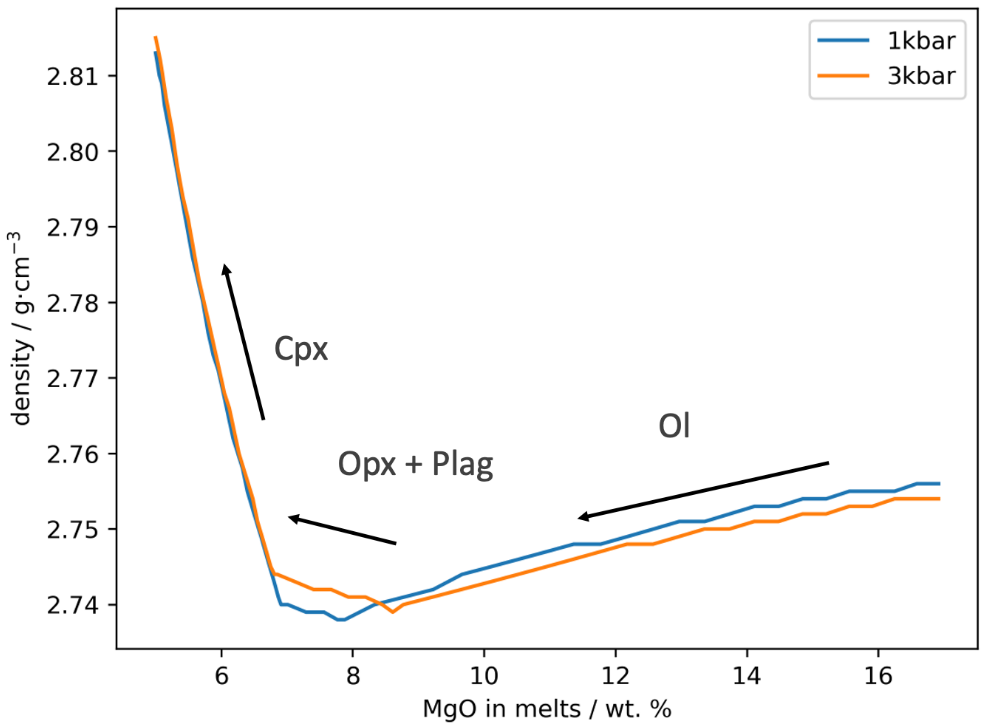

Figure S2. Magma density v.s. MgO content, calculated from Petrolog3 (Danyushevsky & Plechov, 2011), from fractionation at 1 and 3 kbar, respectively. The fractional crystallisation model is taken from Ariskin et al. (1993). Olivine crystallises first, then othropyroxene and plagioclase. Clinopyroxene forms at last. The primary magma composition is taken from Clague et al. (1991).

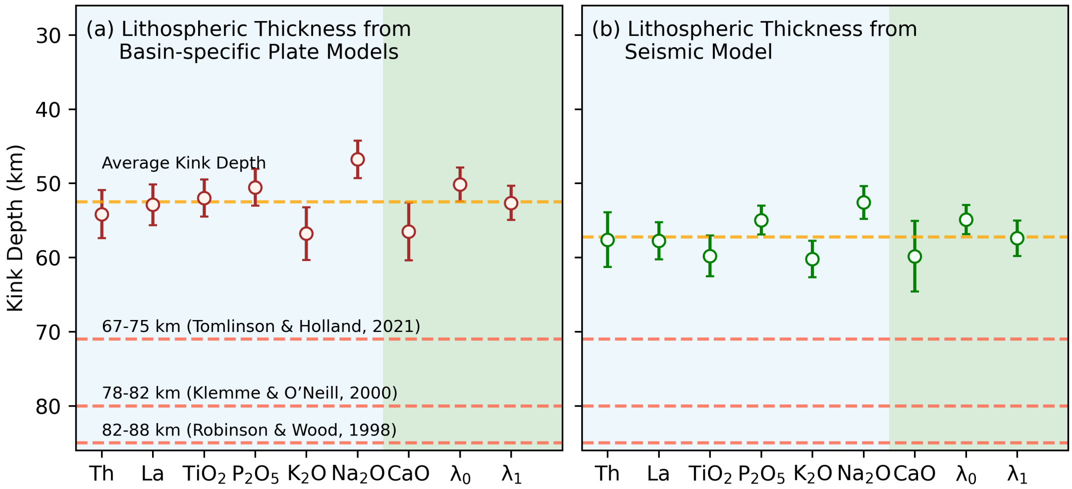

Figure S3. Preferred kink depths for geochemical parameters that are optimally fitted by bi-linear models. Circles with errors = mean and uncertainty range, where the error is equal to two standard deviations of likely kink depths. (a) Results for lithospheric thickness estimates obtained from basin-specific plate models; orange dashed line = average kink depth; red dashed lines = near-solidus spinel-garnet transition depths from experimental petrology (Robinson & Wood, 1998; Klemme & O'Neill, 2000; Tomlinson & Holland, 2021); blue shading = bi-linear trends dominated by melt-fraction effects; green shading = bi-linear trends affected by a combination of melt fraction and spinel-garnet transition depth. (b) Same for lithospheric thicknesses estimated from seismic tomography.

Figure S4. (a-d) $\log_{10}E_1 - \log_{10}E_0$ and (e-f) $\log_{10}E_2 - \log_{10}E_1$ values for major, trace elements and λs in OIBs, using all data (red) as well as datasets with Iceland samples removed (orange), Hawaii samples removed (green), and both sample sets removed (blue). Data in panels (a, b, e, f) are raw OIB compositions and data in panel (c, d, g, h) are fractionation corrected. Lithospheric thickness is estimated using the basin-based plate model (left column) and seismic data (right column). The key threshold value of 2 is represented by dashed horizontal lines, meaning that if the evidence difference of two models is larger than 2, the first model is statistically more favourable. For illustrative purposes, evidence values exceeding 20 are capped. When including all data, using basin-specific plate models and applying fractionation correction, parameters shaded in grey are best fitted by bi-linear models, and parameters without shading are best fitted by bi-linear models.

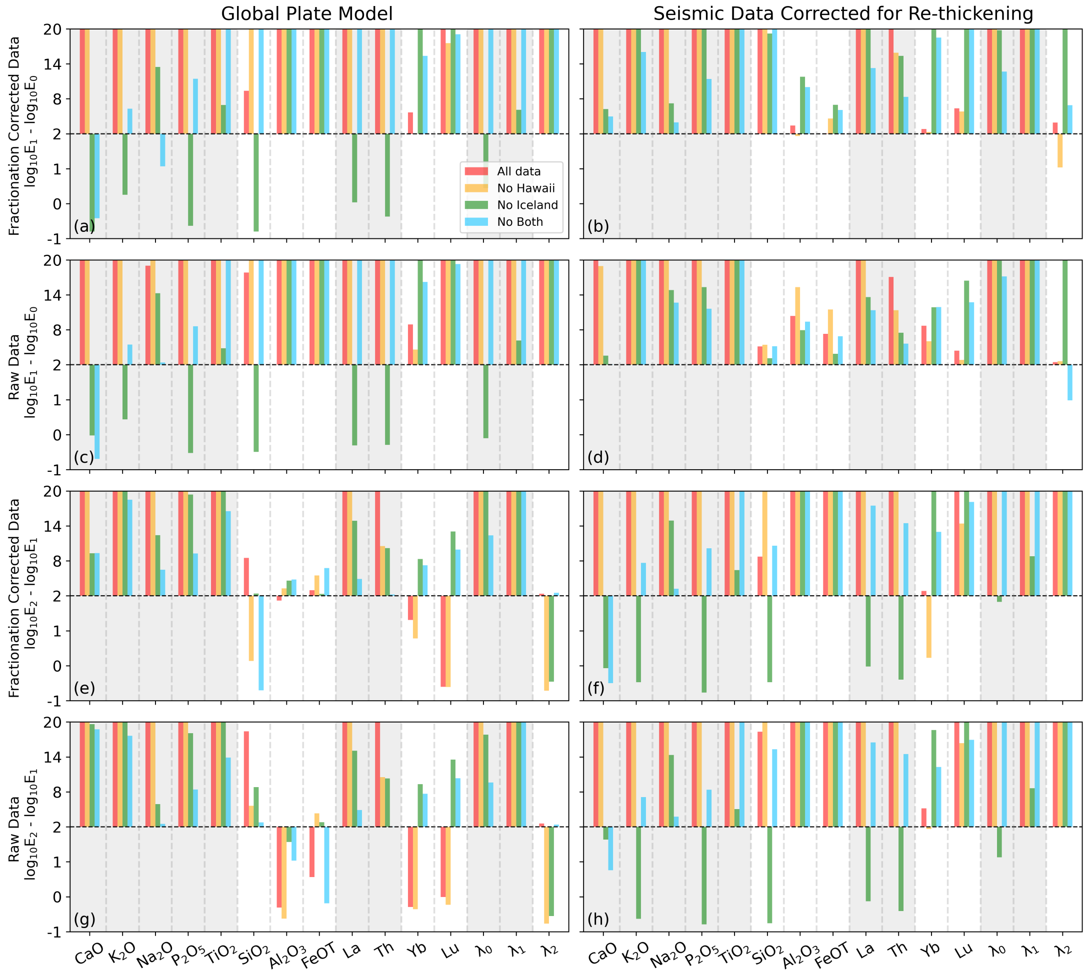

Figure S5. As in Figure S4 but lithospheric thickness is estimated using the global plate model (left column) and seismic data corrected for re-thickening (right column).

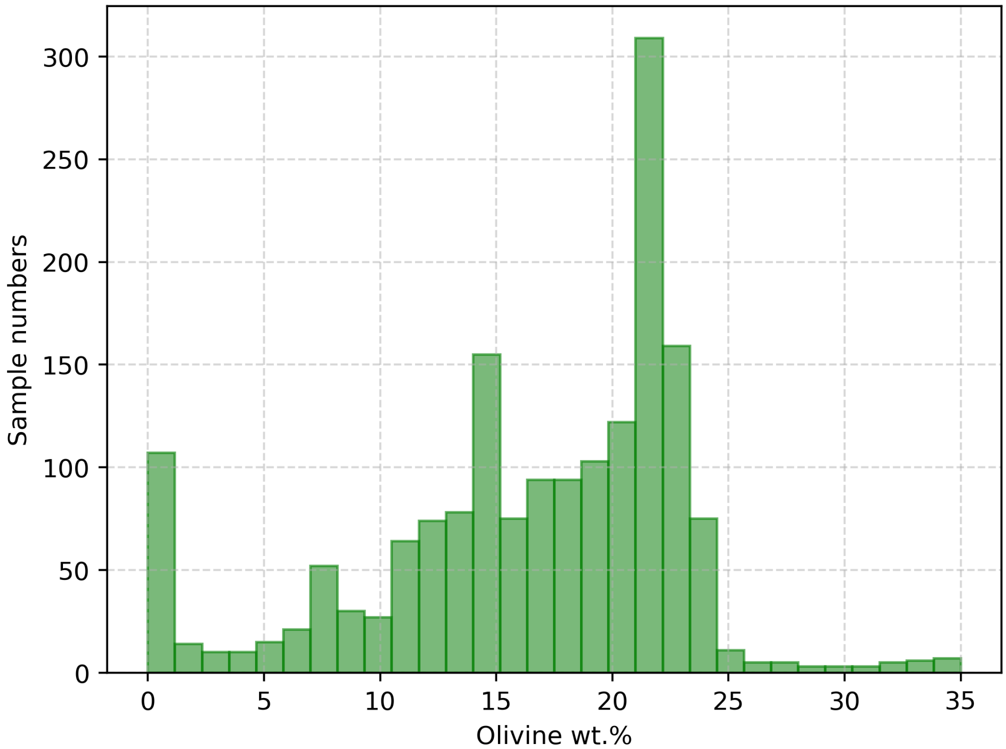

Figure S6. The predicted fraction of olivine that has crystallised from the primitive magma to form the observed OIB compositions. Calculation is performed in Petrolog3 (Danyushevsky & Plechov, 2011).

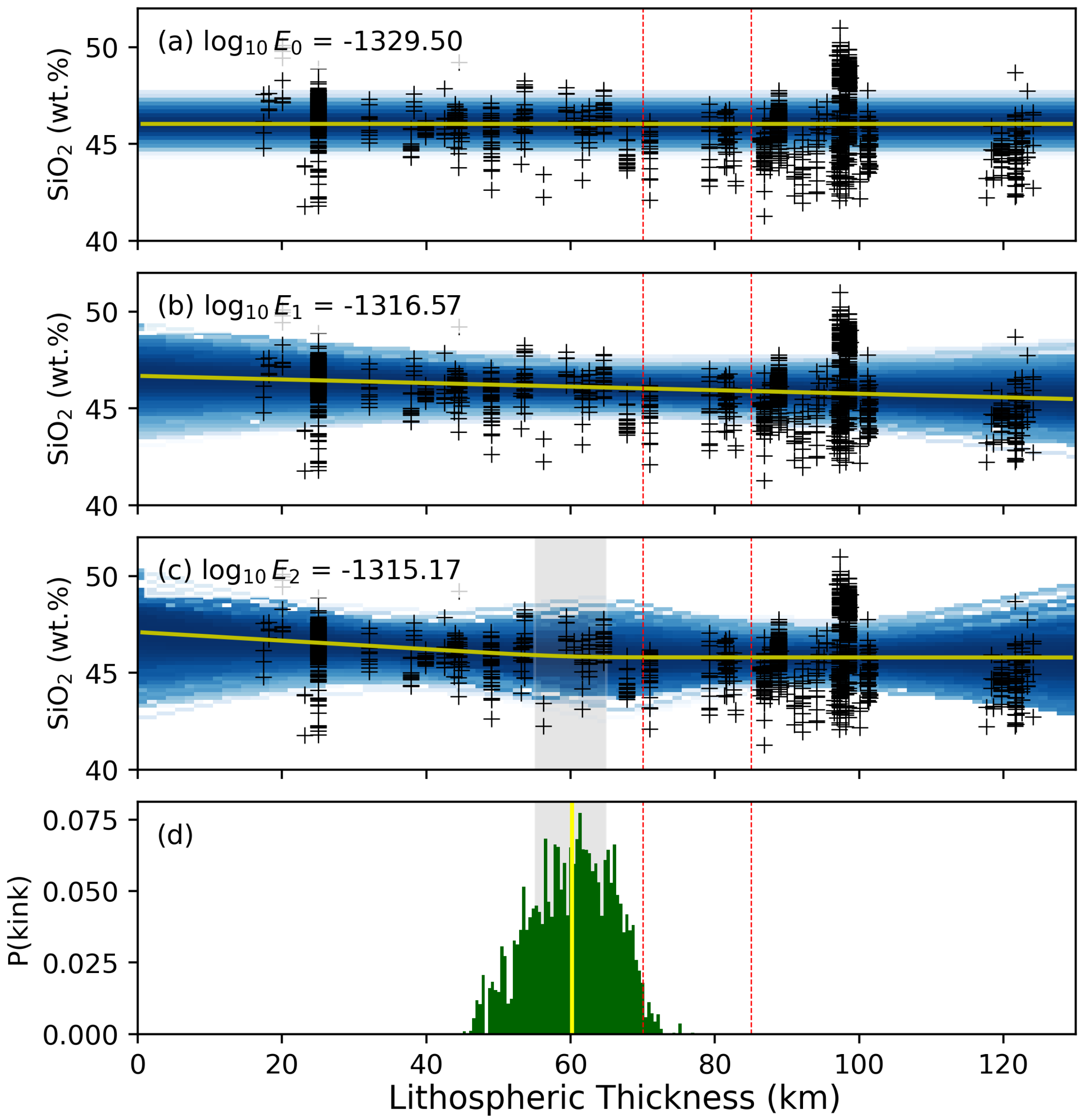

Figure S7. Statistical evidence evaluation results for SiO_2 data, including all sample clusters, using the basin-based plate model, and corrected for the impact of fractional crystallisation. Fitting results are obtained using: (a) a constant model; (b) a linear model; and (c) a bi-linear model. The mean curve is represented by the yellow line, with probability density indicated via blue shading. Panel (d) shows a histogram of the depth of the breakpoint in the bi-linear model, with the yellow vertical line indicating the mean value.

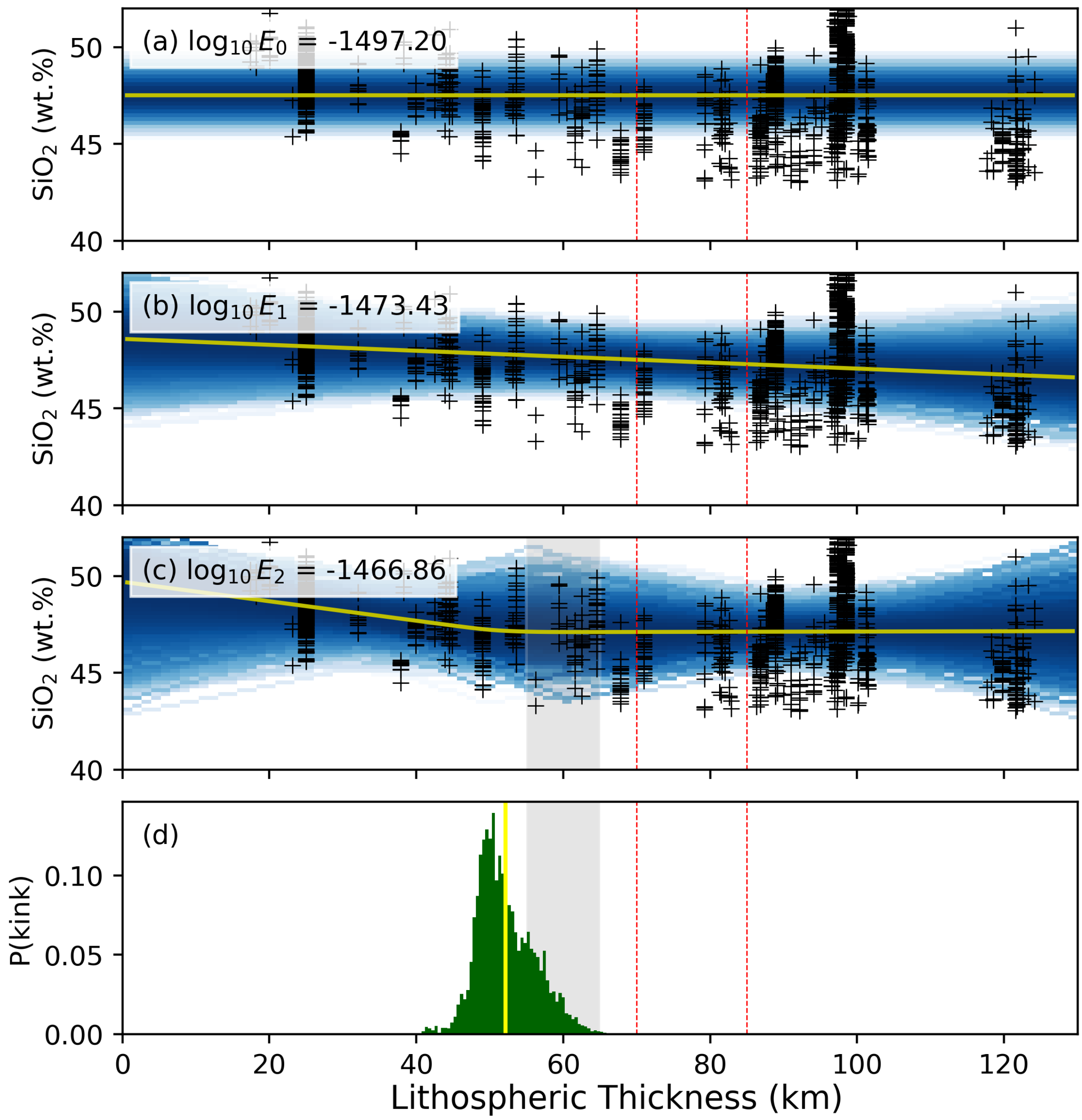

Figure S8. As in Figure S7 but for non-fractionation corrected SiO_2 dataset.

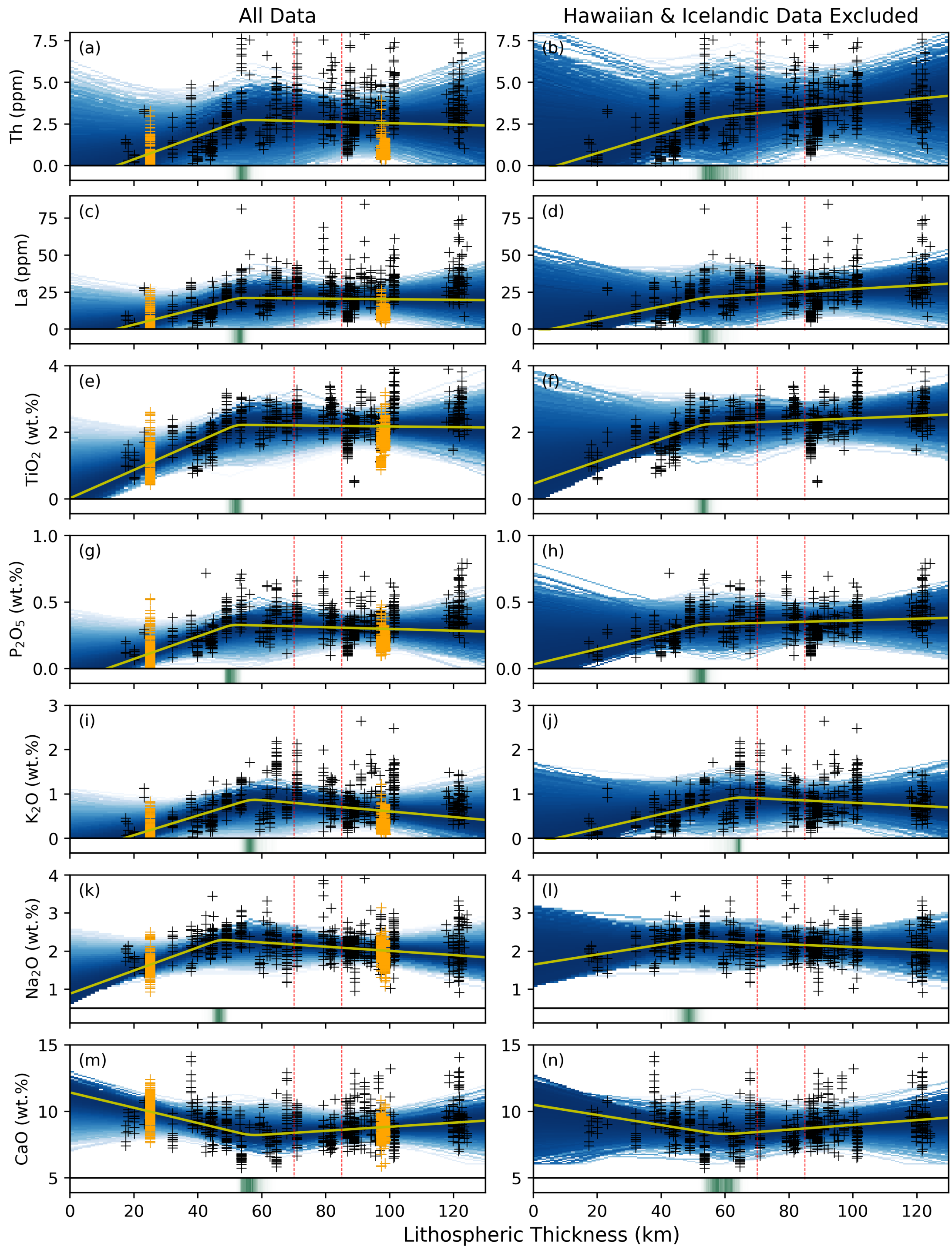

Figure S9. Statistical evidence evaluation results for incompatible elements, but excluding Icelandic and Hawaii samples. Data and panel contents same as for Figure 9 in the main text.

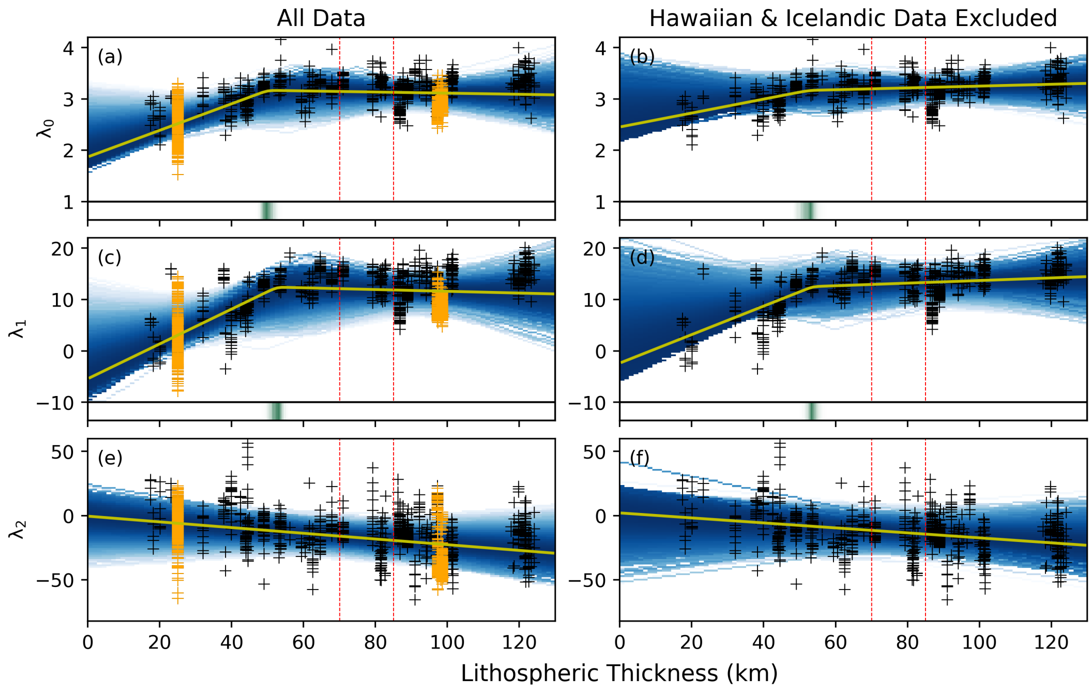

Figure S10. Statistical evidence evaluation results for incompatible elements, but excluding Icelandic and Hawaii samples. Data and panel contents same as for Figure 9 in the main text.

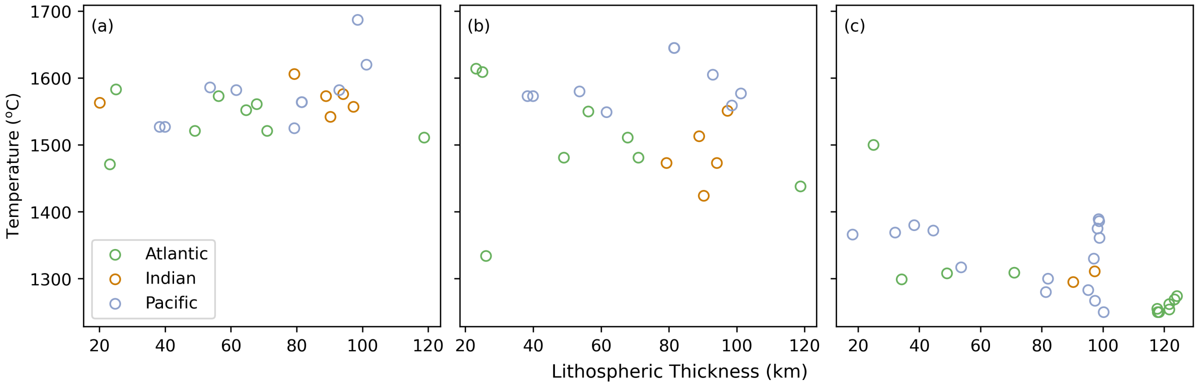

Figure S11. The relationship between lithospheric thickness and the potential temperature of OIB sources estimated from geochemical constraints of (a) Putirka (2008), (b) Bao et al. (2022) and (c) Ball et al. (2021). Localities in the Atlantic, Pacific and Indian Oceans are represented by green, blue and red circles, respectively.

Table S6. λ_2 values for a two-phase melting model at different F_{grt}, F_{spl} and starting melting pressure. REE concentrations in primitive mantle are from McKenzie and O'Nions (1995), and REE concentrations in depleted mantle are from Workman and Hart (2005). Python scripts are available online, as indicated in the Open Research Section.

F_{spl} / F_{grt}	0.00	0.01	0.02	0.03	0.04	0.05	0.06	0.07	0.08	0.09	0.00	0.01	0.02	0.03	0.04	0.05	0.06	0.07	0.08	0.09
3 GPa	Primitive										Depleted									
0.00	–	27.34	22.00	17.40	13.49	10.22	7.52	5.29	3.46	1.98	–	16.36	11.02	6.42	2.51	-0.76	-3.47	-5.70	-7.52	-9.00
0.01	14.09	16.84	14.27	11.29	8.55	6.18	4.20	2.55	1.20	0.10	3.10	5.86	3.29	0.31	-2.43	-4.80	-6.79	-8.43	-9.78	-10.88
0.02	9.54	10.43	8.76	6.69	4.74	3.03	1.59	0.39	-0.59	-1.38	-1.45	-0.55	-2.23	-4.29	-6.24	-7.95	-9.39	-10.59	-11.57	-12.37
0.03	5.78	5.90	4.68	3.22	1.83	0.60	-0.43	-1.29	-1.98	-2.54	-5.20	-5.08	-6.30	-7.76	-9.16	-10.38	-11.42	-12.27	-12.97	-13.52
0.04	2.80	2.59	1.67	0.62	-0.37	-1.24	-1.97	-2.57	-3.04	-3.41	-8.18	-8.39	-9.31	-10.36	-11.36	-12.22	-12.95	-13.55	-14.02	-14.39
0.05	0.54	0.19	-0.52	-1.28	-1.99	-2.59	-3.10	-3.50	-3.80	-4.02	-10.45	-10.79	-11.50	-12.27	-12.97	-13.58	-14.08	-14.48	-14.78	-15.01
0.06	-1.07	-1.47	-2.04	-2.61	-3.11	-3.53	-3.87	-4.13	-4.31	-4.42	-12.05	-12.46	-13.02	-13.59	-14.09	-14.52	-14.85	-15.11	-15.29	-15.40
0.07	-2.09	-2.52	-3.00	-3.44	-3.81	-4.11	-4.33	-4.49	-4.58	-4.62	-13.07	-13.51	-13.98	-14.42	-14.79	-15.09	-15.32	-15.47	-15.56	-15.60
0.08	-2.56	-3.04	-3.47	-3.84	-4.14	-4.36	-4.52	-4.61	-4.64	-4.63	-13.55	-14.02	-14.45	-14.82	-15.12	-15.34	-15.50	-15.59	-15.63	-15.61
0.09	-2.54	-3.06	-3.50	-3.85	-4.12	-4.31	-4.43	-4.49	-4.50	-4.47	-13.52	-14.04	-14.48	-14.83	-15.10	-15.29	-15.41	-15.48	-15.49	-15.45
4 GPa																				
0.00	–	27.86	22.70	18.21	14.37	11.13	8.42	6.17	4.31	2.78	–	16.87	11.72	7.23	3.39	0.15	-2.56	-4.81	-6.67	-8.20
0.01	-2.20	17.22	15.33	12.43	9.68	7.26	5.21	3.50	2.08	0.91	-13.18	6.24	4.34	1.45	-1.30	-3.72	-5.77	-7.48	-8.90	-10.07
0.02	-7.50	8.64	8.90	7.36	5.57	3.89	2.42	1.18	0.14	-0.72	-18.48	-2.34	-2.08	-3.62	-5.42	-7.09	-8.56	-9.80	-10.84	-11.70
0.03	-12.08	1.86	3.49	3.01	2.02	0.98	0.01	-0.83	-1.54	-2.13	-23.06	-9.12	-7.49	-7.97	-8.96	-10.01	-10.97	-11.82	-12.52	-13.11
0.04	-15.97	-3.57	-1.03	-0.68	-1.01	-1.53	-2.07	-2.57	-3.00	-3.35	-26.95	-14.55	-12.01	-11.66	-11.99	-12.51	-13.05	-13.55	-13.98	-14.33
0.05	-19.24	-7.95	-4.79	-3.80	-3.59	-3.68	-3.86	-4.07	-4.25	-4.39	-30.22	-18.94	-15.77	-14.79	-14.57	-14.66	-14.84	-15.05	-15.23	-15.38
0.06	-21.95	-11.52	-7.92	-6.44	-5.79	-5.51	-5.40	-5.35	-5.33	-5.29	-32.93	-22.50	-18.91	-17.42	-16.77	-16.50	-16.38	-16.34	-16.31	-16.28
0.07	-24.19	-14.43	-10.54	-8.66	-7.66	-7.08	-6.72	-6.46	-6.25	-6.06	-35.17	-25.41	-21.52	-19.65	-18.65	-18.07	-17.70	-17.44	-17.23	-17.04
0.08	-26.02	-16.81	-12.71	-10.54	-9.26	-8.42	-7.84	-7.39	-7.03	-6.70	-37.00	-27.79	-23.70	-21.52	-20.24	-19.41	-18.82	-18.38	-18.01	-17.68
0.09	-27.50	-18.76	-14.53	-12.12	-10.60	-9.56	-8.79	-8.19	-7.68	-7.24	-38.49	-29.75	-25.51	-23.11	-21.59	-20.54	-19.77	-19.17	-18.66	-18.22
5 GPa																				
0.00	–	28.37	23.43	19.09	15.34	12.13	9.43	7.15	5.25	3.67	–	17.39	12.44	8.10	4.35	1.15	-1.56	-3.83	-5.73	-7.31
0.01	-3.11	19.25	17.01	13.95	11.08	8.57	6.43	4.62	3.12	1.86	-14.09	8.26	6.02	2.97	0.10	-2.41	-4.55	-6.36	-7.87	-9.12
0.02	-8.25	11.13	11.06	9.24	7.23	5.38	3.76	2.38	1.22	0.26	-19.24	0.14	0.07	-1.75	-3.75	-5.60	-7.22	-8.60	-9.76	-10.72
0.03	-12.78	4.41	5.84	5.07	3.83	2.56	1.41	0.41	-0.44	-1.15	-23.77	-6.57	-5.14	-5.91	-7.16	-8.42	-9.57	-10.57	-11.42	-12.13
0.04	-16.72	-1.13	1.36	1.44	0.85	0.09	-0.65	-1.32	-1.90	-2.38	-27.70	-12.11	-9.62	-9.55	-10.14	-10.89	-11.64	-12.31	-12.88	-13.37
0.05	-20.10	-5.72	-2.47	-1.71	-1.75	-2.07	-2.46	-2.84	-3.18	-3.46	-31.08	-16.71	-13.45	-12.69	-12.73	-13.05	-13.44	-13.82	-14.16	-14.45
0.06	-22.98	-9.55	-5.74	-4.42	-4.00	-3.95	-4.04	-4.17	-4.30	-4.40	-33.96	-20.53	-16.72	-15.40	-14.99	-14.93	-15.02	-15.15	-15.28	-15.39
0.07	-25.42	-12.74	-8.52	-6.76	-5.96	-5.59	-5.41	-5.32	-5.27	-5.22	-36.40	-23.73	-19.51	-17.74	-16.94	-16.57	-16.39	-16.31	-16.25	-16.20
0.08	-27.47	-15.43	-10.90	-8.77	-7.65	-7.01	-6.61	-6.33	-6.11	-5.92	-38.46	-26.41	-21.88	-19.76	-18.64	-17.99	-17.59	-17.31	-17.09	-16.90
0.09	-29.20	-17.68	-12.93	-10.51	-9.12	-8.24	-7.64	-7.19	-6.83	-6.51	-40.19	-28.66	-23.91	-21.49	-20.10	-19.22	-18.62	-18.17	-17.81	-17.50